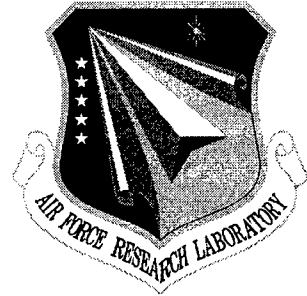


AFRL-SN-RS-TR-1998-95
Final Technical Report
April 1998



AIR DEFENSE INITIATIVE (ADI) CLUTTER MODEL

PAR Government Systems Corporation

W. L. Simkins, Jr.

APPROVED FOR PUBLIC RELEASE; DISTRIBUTION UNLIMITED.

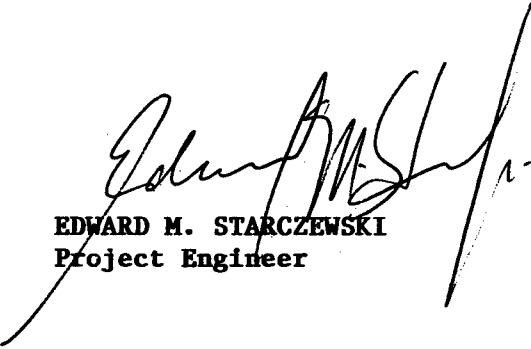
19980618 099

**AIR FORCE RESEARCH LABORATORY
SENSORS DIRECTORATE
ROME RESEARCH SITE
ROME, NEW YORK**

This report has been reviewed by the Air Force Research Laboratory, Information Directorate, Public Affairs Office (IFOIPA) and is releasable to the National Technical Information Service (NTIS). At NTIS it will be releasable to the general public, including foreign nations.

AFRL-SN-RS-TR-1998-95 has been reviewed and is approved for publication.

APPROVED:


EDWARD M. STARCZEWSKI
Project Engineer

FOR THE DIRECTOR:


ROBERT G. POLCE, Acting Chief
Rome Operations Office
Sensors Directorate

If your address has changed or if you wish to be removed from the Air Force Research Laboratory Rome Research Site mailing list, or if the addressee is no longer employed by your organization, please notify AFRL/SNRT, 26 Electronic Pky, Rome, NY 13441-4514. This will assist us in maintaining a current mailing list.

Do not return copies of this report unless contractual obligations or notices on a specific document require that it be returned.

REPORT DOCUMENTATION PAGE			Form Approved OMB No. 0704-0188	
<p>Public reporting burden for this collection of information is estimated to average 1 hour per response, including the time for reviewing instructions, searching existing data sources, gathering and maintaining the data needed, and completing and reviewing the collection of information. Send comments regarding this burden estimate or any other aspect of this collection of information, including suggestions for reducing this burden, to Washington Headquarters Services, Directorate for Information Operations and Reports, 1215 Jefferson Davis Highway, Suite 1204, Arlington, VA 22202-4302, and to the Office of Management and Budget, Paperwork Reduction Project (0704-0188), Washington, DC 20503.</p>				
1. AGENCY USE ONLY (Leave blank)	2. REPORT DATE	3. REPORT TYPE AND DATES COVERED		
	April 1998	Final Jul 89 - Jan 90		
4. TITLE AND SUBTITLE	5. FUNDING NUMBERS			
AIR DEFENSE INITIATIVE (ADI) CLUTTER MODEL		C - F30602-89-D-0027, Task 7 PE - 63741F PR - 3640 TA - QC WU - 08		
6. AUTHOR(S)	8. PERFORMING ORGANIZATION REPORT NUMBER			
William L. Simkins, Jr.	N/A			
7. PERFORMING ORGANIZATION NAME(S) AND ADDRESS(ES)	10. SPONSORING/MONITORING AGENCY REPORT NUMBER			
PRIME: PAR Government Systems Corporation PAR Technology Park 220 Seneca Turnpike New Hartford NY 13413-1191	SUB: W.L. Simkins RD 1 Box 295 Camden NY 13316	AFRL-SN-RS-TR-1998-95		
9. SPONSORING/MONITORING AGENCY NAME(S) AND ADDRESS(ES)	11. SUPPLEMENTARY NOTES			
AFRL/SNRT 26 Electronic Pky Rome NY 13441-4514	AFRL Project Engineer: Edward M. Starczewski/SNRT/(315) 330-7127			
12a. DISTRIBUTION AVAILABILITY STATEMENT	12b. DISTRIBUTION CODE			
Approved for public release; distribution unlimited				
13. ABSTRACT (Maximum 200 words) This is a republication of RADC-TR-90-170.				
<p>This technical report documents a detailed radar clutter model utilized throughout the duration of the Air Defense Initiative (ADI) program conducted by the US Air Force from 1985 to 1995. One objective of this effort was to identify possible sources of false alarms in an airborne early warning (AEW) radar environment, and quantify the number of sources as a function of radar frequency, location, season, and time of day. Analysis is presented for radars designed to operate at UHF, L-Band, and S-Band. The environments modeled included tropospheric clutter (precipitation, lightning, and turbulent layer), sea clutter (open sea and land-sea interface), distributed terrain clutter, discrete manmade clutter (buildings, vehicles, and vessels), angels (birds and insects), and aurora.</p>				
<p>ADI was initially created to provide for a defense against low radar cross section threats. The most significant problem facing ADI is achieving a high probability of detection against modern targets while maintaining very low false alarm rates due to clutter returns. Given the power and size constraints of an AEW radar, most of the burden for achieving this performance is placed on waveform design and signal processing which, in turn, is strongly influenced by how the interference from the clutter environment is defined.</p>				
14. SUBJECT TERMS			15. NUMBER OF PAGES	
Radar Clutter, Backscatter, Land Clutter, Sea Clutter, Angels, Aurora, Weather Clutter, Clutter Models			132	
16. PRICE CODE				
17. SECURITY CLASSIFICATION OF REPORT	18. SECURITY CLASSIFICATION OF THIS PAGE	19. SECURITY CLASSIFICATION OF ABSTRACT	20. LIMITATION OF ABSTRACT	
UNCLASSIFIED	UNCLASSIFIED	UNCLASSIFIED	UL	

TABLE OF CONTENTS

1.0 Introduction	1-1
2.0 Summary and Recommendations	2-1
3.0 Tropospheric Clutter	3-1
4.0 Sea Clutter	4-1
5.0 Terrain Clutter	5-1
6.0 Manmade Structures	6-1
7.0 Birds and Insects	7-1
8.0 Auroral Clutter	8-1
9.0 References	9-1

1.0 INTRODUCTION

The Air Defense Initiative (ADI) was created to address the defense of the continental United States (CONUS) against the low radar cross section (RCS) threat of the future. One of the biggest performance problems facing ADI is achieving a high probability of detection of very small RCS targets while maintaining very low false alarm rates from the clutter environment. Given the power and size constraints of an airborne platform, most of the burden of achieving this performance is placed on waveform design and signal processing, which, in turn, is strongly influenced by how the interference from the clutter environment is defined. Experiences with several radar programs in the 1970's and early 1980's have shown that the use of inaccurate clutter models will lead to good predictions of performance on paper, but disappointing performance in the field. Therefore, it is very important that the ADI program use a description of the clutter environment that is as accurate as possible.

Ignoring the time and money constraints, the best approach to determining the ADI clutter problem is to build a flexible instrumented measurement system that has the power, antenna aperture and bandwidth required by ADI and use it for extensive clutter and target detection measurements. Unfortunately, such a system is very expensive to build and operate and the measurement efforts require a large number of manhours to obtain and adequately analyze the data.

The next best approach is to use clutter models based on existing information for the development of an advanced development (ADM) ADI system. Ideally, these models would describe the results of existing measured data and theory through equations and graphs which allow extrapolation to the ADI system parameters. Potential clutter issues that have been observed but not adequately measured can also be identified for further study. An ADM ADI system could then be used to perform a limited number of measurements on the little known clutter problems for use in the final ADI system procurement.

RADC has been involved in the development of clutter models for system procurements for many years. Between 1976 and 1979, RADC performed measurements and suggested clutter models for the SEEK IGLOO (1976) and the SEEK FROST (1978-9) programs. Since 1980, current clutter models for ground-based systems were maintained by RADC for in-house research and development programs and were updated as new information became available. Versions of

these models were also provided in support of system procurements including the Advanced Tactical Radar program (1981), the North Warning System radar procurement (1982), the FAA/ARSR-4 radar procurement (1984) and the US Customs Service SOWRBALL radar procurement (1985-6). The ARSR-4 clutter model (Simkins 1984) addressed the important clutter issues of a ground-based L-Band system with well-defined constraints on system bandwidth, scan times, antenna size and volume coverage. This study upgrades the ARSR-4 clutter model by incorporating measurements, models and other developments that have been published or presented since the ARSR-4 model's development, by extending the existing models to the airborne geometries and by proposing new models unique to the ADI environment. For the ADI problem, the following issues had to be addressed:

- a. the extension of existing parameters to UHF;
- b. the extension of the surface clutter parameters to grazing angles up to 90 degrees;
- c. the presentation of a larger number of terrain and sea environments including land, urban, rural, sea, land-sea interface and mountains;
- d. a re-examination of the impact of an elevated platform on the models for angels (i.e. birds and insects), man-made targets and propagation;
- e. the development of models for clutter issues unique to ADI such as aurora.

The next section of the report provides a brief summary of the clutter models for each of the environments and presents those potential clutter problems that could not be modeled and require further investigation. The subsequent sections present the study results for tropospheric clutter (precipitation, refractive index irregularities, and lightning), sea clutter (open sea and land-sea interface), terrain clutter, manmade structures (buildings, vehicles and vessels), birds and insects and aurora.

2.0 SUMMARY AND RECOMMENDATIONS

The section begins with a brief summary of the clutter models proposed for ADI. The second part of this summary will briefly discuss some of the effects of platform motion on the observed clutter statistics. Next, clutter-related phenomena that could not be modeled due to a lack of information are discussed. Finally, recommendations are made for future work.

2.1 Summary of Proposed ADI Clutter Models

The distributed clutter sources defined in the model are terrain, sea, weather and aurora. The point clutter or discrete sources modeled represent manmade land structures, vehicles, ships, buoys, and angels (birds and insects). The models are applicable for UHF, L-Band and S-Band systems. The value and equations given in the following sections for distributed land clutter and sea clutter inherently include local multipath and small-scale shadowing effects. For manmade structures, vehicles, vessels and other scatterers above the surface of the earth, multipath is not included in the given values and must be accounted for separately.

These models present the physical locations and intrinsic characteristics of the clutter and do not include the effects due to platform motion, radar instabilities or nonlinearities.

2.1.1 Tropospheric Clutter

The tropospheric clutter reviewed in this section includes backscatter from precipitation, turbulent layers and local changes in the index of refraction. Each clutter type is treated as a volumetric scatterer where the backscatter or volume reflectivity is described as a random process.

The precipitation is presented as a storm system that is 200 nm in diameter with strong convective cells embedded in widely distributed lighter rain. A description of the spatial extent and intensity of the cellular and distributed rain is given in Table 2.1 for mid-Latitude and tropical environments. The cellular precipitation in the mid-latitude model is randomly distributed throughout the storm system while the tropical model has cells in various stages of development traveling in clusters of 5 - 10 cells per group.

TABLE 2.1 SPATIAL DISTRIBUTION OF RAIN TYPES

	MIDDLE LATITUDES	TROPICAL LATITUDES		
Cellular Precipitation				
* Core height (ft)	0 - 15,000	0 - 20,000		
* Number of cells within 200 nm storm	172	211		
* Spatial distribution of cells	Uniform	In uniformly distributed clusters		
* Cluster size	N/A	400 nm ²		
* Cell Size and Rainfall Rate				
Mean Rainfall Rate (mm/hr)	Number of cells	Diameter (nm)	Number of cells	Diameter (nm)
3.5	51	3.1	50	2.2
9.0	58	2.8	46	1.8
18.0	50	2.4	42	1.5
35.0	10	1.6	25	1.3
70.0	3	1.2	23	1.1
175.0	2	.7	20	0.6
350.0	--	---	6	0.5
* Edge Falloff				
* Horizontal	6 dBZ/nm	8 dBZ/nm		
* Vertical	2 dBZ/kft	2 dBZ/kft		
* Fall Rate	15 knots	15 knots		
Distributed Precipitation				
* Bright Band				
* Mean Equivalent Rainrate	10 mm/hr	10 mm/hr		
* Vertical Width	1 kft	1.5 kft		
* Altitude at Bottom of Layer	9 kft	13 kft		
* Vertical Fall Rate	2 knots	2 knots		
* Rain below the Bright Band				
* Height	0 to 9 kft	0 to 13.5 kft		
* Mean Rainrate	1 mm/hr	1 mm/hr		
* Areal Extent	Throughout storm system bwt cells	Within clusters between cells		
* Vertical Fall Rate	10 knots	10 knots		

TABLE 2.2 WEATHER BACKSCATTER AND ATTENUATION RELATIONSHIPS
BACKSCATTER FORMULA AND DENSITY FUNCTIONS

Relationships between the rainfall rate r , the mean volume reflectivity η_v , and the reflectivity factor Z

$$\eta_v = p^5 |k|^2 Z/\lambda^4 = 5.69 \cdot 10^{-14} r^{1.6/4} (\text{m}^2/\text{m}^3)$$

$$Z = 200 r^{1.6} \text{ mm}^6/\text{m}^3$$

Reduction in volume reflectivity η_v with circular polarization

$$CR = \begin{cases} -15 \text{ db for rain} \\ -10 \text{ db for bright band} \end{cases}$$

The pdf of mean volume reflectivity η_v due to small-scale variation in the rainrate of distributed rain or a cellular rain cell.

$$p_k(\eta_v) = [k^k \eta_v^{k-1} \exp(-k\eta_v/\eta_r)] / \{\Gamma(k)(\eta_r)^k\}$$

where $k = [(R \theta/D_r) * (cv/2)/D_r] =$ the number of uncorrelated samples of η_v within the resolution cell.

$\eta_r =$ the expected value of the volume reflectivity associated with the rainrate of distributed rain or within the core of a cellular rain cell

$D_r =$ the distance between uncorrelated samples of $\eta_v = 1000$ feet

Conditional pdf of instantaneous volume reflectivity η_v

$$p(\eta_v/\eta_r) = \exp(-\eta_v/\eta_r)/\eta_r$$

Compound pdf of instantaneous volume reflectivity η_v

$$p(\eta_v) = \int_0^{\infty} p(\eta_v/\eta_r=\eta) p^k(\eta) d\eta$$

ATTENUATION DUE TO RAIN

Attenuation Factor $a = .00013 (f)^{2.36} r_{avg} R$

$r_{avg} =$ conditional path average rainrate given that it is raining within 100 nm
= .42 mm/hr/nm

TABLE 2.3 WIND VELOCITY AND WEATHER SPECTRA
HORIZONTAL WIND VELOCITY

- * ENVIRONMENTAL WINDS IN CLEAR WEATHER OR IN DISTRIBUTED RAIN
 - * Mean Velocity = 10 knots, gusting to 20 knots $h < .2$ kft
 - * Mean Velocity = $10 + \text{SHR1} * h$ (knots) $.2 \text{ kft} < h < 20$ kft
 - * Mean Velocity = $20 + \text{SHR2} * (h - 20)$ (knots) $20 \text{ kft} < h$
 - SHR1 = .5 knots/kft; SHR2 = 1.7 knots/kft

* WINDS IN CELLULAR RAIN

The mean velocity of the cell structure is 20 knots in the same direction as the winds in the distributed rain. Within the cell (including the extended edges) below 20 kft., a vertical wind shear with respect to both speed and direction is present, but the shear at the front of the storm is slightly different than at the back. At the front quadrant of the storm, the mean velocity V as a function of altitude is given as

$$V_{\text{front}} = \text{SHR3} * (h-3) \text{ (knots)} ; \text{SHR3} = 2.55$$

For the back of the storm,

$$V_{\text{back}} = \text{SHR4} * (h-10) + 20 \text{ (knots)} ; \text{SHR4} = 2.35.$$

where the sign of the velocity for both equations is relative to the environmental winds. For the side quadrants,

$$V_{\text{side}} = j \text{SHR4} * (h-10)$$

where $j = +1$ for one side and -1 for the other. In this case, the sign represents the velocity relative to the storm center.

Above the cell core between 20 kft and 34 kft, the wind velocities are constant, but the direction of the side winds slowly change uniformly in the direction of the environmental winds. Above 34 kft, the environmental winds exist.

The shape of the spectral distribution from the rain is a function of the antenna gain function illuminating the rain. For rain illuminated by a complete Gaussian antenna pattern, the spectral shape of the rain will be Gaussian with a standard deviation σ_r given as

$$\sigma_r = [(\text{TURB})^2 + (\text{FALL})^2 + (\text{WIND SHEAR})^2 + (\text{BEAM})^2]^{.5}$$

where

TURB = standard deviation of the wind turbulence = 1.4 (knots)

FALL = s.d. of the fall velocities = $2 |\sin \phi_e|$ (knots)

BEAM = s.d. of the beam spread = $.42 V \theta |\sin \theta_w|$ (knots)
s.d. of the vertical wind shear

WIND = {

SHEAR = $2.55 * (\text{SHRx}) * R \phi \cos \phi_e |\cos \theta_w|$ (knots)

SHRx = shear values given in above for $x = 1, 2, 3, 4$

R = Range in nm

ϕ = two-way elevation beamwidth (radians)

θ = two-way azimuthal beamwidth (radians)

θ_w = angle between wind direction and the center of the beam (radians)

ϕ_e = elevation angle

V = mean velocity at the center of the beam (knots)

h = altitude, (kilofeet MSL)

For the tropical environment, the distributed precipitation exists only within the 400 nm^2 clusters. For the middle latitude environment, the distributed precipitation exists between the cells within the group and between the cell groups throughout the storm system.

Table 2.2 defines the relationships between rainfall rate, average and instantaneous volume reflectivity, frequency and attenuation. The propagation loss for any given path shall also include the atmospheric loss as given in NRL Report 6930. Note that the weather backscatter is treated as a inhomogeneous process with the mean reflectivity varying in space about the expected values related to the average rainrate in a rain cell. The backscatter from rain in a resolution cell is time varying, but can be considered stationary for short intervals. Table 2.2 also gives the average fall rates for precipitation. While real convective systems have vertical velocities that can be positive (updrafts) and negative (downdrafts), only vertical velocities are given in the model.

Table 2.3 defines the environmental winds as a function of height and presents formulas for calculating the spectral spread of the rain backscatter. While the simplifying assumption of a Gaussian beamshape is used as an example, the use of the actual antenna pattern is expected for analysis. When the rain partially fills the antenna pattern or different rainrates are observed in different regions of the pattern, then the spectral shape can be obtained by weighting the contribution of each scattering volume with the antenna gain in the direction of that volume.

Lightning is both a source of noise and a source of radar clutter. When the electromagnetic energy generated during a discharge has sufficient power at the radar frequency to be detected, such a signal is called a "sferic". The ionized channel created by the discharge can also be a significant source of backscatter. Models for the amplitudes and velocity characteristics are given in Table 2.4.

Tropospheric clutter has also been related to inhomogeneities in the refractive index. Radar echoes structured in horizontal layers were found to correspond in height to regions of refractive-index inhomogeneities. When there is a considerable amount of turbulence in atmospheric regions having a high spatial gradient of refractive index n , the irregular, small-scale fluctuations of n can cause appreciable backscatter. Table 2.5 summarizes their amplitude and velocity characteristics.

TABLE 2.4 LIGHTNING

Number of flashes/min/nm: 20

Backscatter:

Average RCS per flash : 10 dBsm, UHF thru S-Band

Duration of echo : 100 msec exponential time constant

Mean radial doppler : 0 m/s

Sferic:

Amplitude at 10 km : 10 microvolts/m at S-Band
within a BW of 1 Khz. : 20 microvolts/m at L-Band

40 microvolts/m at UHF

of pulses/flash : 1 to 20

Duration /pulse : 20 to 35 microseconds

Spacing bwt pulses : 10 to 30 microseconds

TABLE 2.5 TURBULENT LAYERS

Mean volume reflectivity η_v

$$\eta_v = 0.38 C_n^2 k^{-0.33} m^2/m^3$$

$$C_n^2 = 10^{-13} \text{ to } 3 \times 10^{-11}$$

Fluctuation about η_v follows an Exponential distribution

Layers travel at the wind velocity

Layers can exist up to 10 km

2.1.2 Sea Clutter

Two types of sea clutter are modeled, open sea and the land-sea interface. For the open sea, amplitude and velocity statistics are given for five sea states. The mean value varies spatially from resolution cell to resolution cell and as a function of time within a single resolution cell as waves move through the illuminated volume. Table 2.6 presents the equations defining the distribution of mean and instantaneous reflectivity about the expected value of the mean reflectivity which, in turn, is related to grazing angle, polarization, frequency and sea state. Table 2.7 presents the relationships between the average mean value, sea state and wind speed.

For observations of a single cell, the temporal covariance function of σ_o is given by

$$R(\tau) = aR_1(\tau) + bR_2(\tau).$$

where $a = 1/k$, $b = 1-a$ and k is the shape parameter given above.

$$R_1(\tau) = [\sin(\pi\tau/(.707)t_w)/\pi(\tau/(.707)t_w)]^2$$

and

$$R_2(\tau) = \exp(-\tau^2/2\sigma_\tau^2)$$

where t_w is the water period of the given sea state (Table 2.7), $\sigma_\tau = 1/(2\pi\sigma_f)$ and σ_f is the standard deviation of the doppler spectrum.

The velocity density function for sea is Gaussian with a radial mean velocity μ_v and standard deviation σ_v given by

$$\mu_v = 1.15 w \cos \theta_w \text{ (knots) HH}$$

$$\mu_v = .13 w \cos \theta_w \text{ (knots) VV}$$

$$\sigma_v = .1 w \text{ (knots) HH, VV}$$

where w is the wind speed in knots. The corresponding doppler components μ_f and σ_f can be obtained by

$$\mu_f = 1.03 \mu_v/\lambda$$

and

$$\sigma_f = 1.03 \sigma_v/\lambda.$$

Several of the differences between shallow and deep water waves given above could account for the "land-sea interface" effect often observed. Shallow depths cause both increased wave height and increased density which can increase the mean reflectivity above that observed in the adjacent deeper water. Plunging breakers creates a transitional wave travels at the wave

TABLE 2.6 AMPLITUDE DENSITY FUNCTION OF SEA CLUTTER REFLECTIVITY COEFFICIENT

* The mean reflectivity σ_o is a function of range R varies around a nominal expected value $\underline{\sigma}_g$ which is a function of the grazing angle ϕ_g . The pdf of σ_o follows a gamma density function

$$p_k(\underline{\sigma}_o) = [k^k \underline{\sigma}_o^{k-1} \exp(-k\underline{\sigma}_o/\underline{\sigma}_o)] / \{\Gamma(k)(\underline{\sigma}_g)^k\}$$

where

k = the effective number of scatterers in a resolution cell
 $\approx [(c \tau/2D) |\cos \theta_w| + (R \theta_a/D) |\sin \theta_w|] * \phi_g^b$
 b = 2
 $\underline{\sigma}_g$ = the nominal expected value as a function of grazing angle
 θ_a = -3 db two-way antenna beamwidth in azimuth (degrees)
 θ_w = the azimuth angle between the wind and wave direction and the antenna beam
 λ = wavelength (meters)
 $\Gamma(\)$ = gamma function
 ρ_g = correlation length, distance between uncorrelated samples of σ_o
 v = pulse width in microseconds
 v_d = time delay
 ϕ_e = -3 dB two-way antenna beamwidth in elevation
 R = range, feet
 c = .984 ft/nsec
 D = .5 water wavelength, feet for HH; 3 feet for VV

The normalized gamma distribution function defined as

$$\text{PROB}(y < y) = \int p_k(x) dx$$

* Conditional pdf of instantaneous surface reflectivity σ_o

$$p(\sigma_o/\sigma_o=\sigma) = \exp(-\sigma_o/\sigma)/\sigma$$

Compound pdf of instantaneous surface reflectivity σ_o

$$\begin{aligned}
 p(\sigma_o) &= \int_0^{\infty} p(\sigma_o/\sigma_o=\sigma) p_k(\sigma) d\sigma \\
 &= [2k((k+1)/2) (\sigma_o/\underline{\sigma}_o)((k-1)/2)/\Gamma(k)] K_{k-1}(2(k\sigma_o/\underline{\sigma}_o).5)
 \end{aligned}$$

where $K_v()$ is the modified Bessel function of the second kind of order v.

TABLE 2.7 RELATIONSHIP BETWEEN MEAN REFLECTIVITY, GRAZING ANGLE AND SEA STATE

The nominal expected value σ_g is related to grazing angle by

$$\sigma_g = A(\phi_g) * [B(\phi_i) + C(\phi_i)]$$

where $\phi_i = 90 - \phi_g$ (degrees)

the propagation factor $A(\phi_g)$ is given by

$$A(\phi_g) = \varphi^2 / (1 + \varphi^2)$$

$$\varphi = \theta_g h_{1/3} (.2 + .11/\lambda)$$

$$h_{1/3} = (w/17)^2$$

w = wind speed for sea state in knots

The plateau factor $B(\phi_g)$ is given by

$$B(\phi_g) = [5 s_b^{1.6} / \ln(s_b^{.5})(\phi_d + s_b)(2\pi)^{.5}] * \exp\{-(\ln(\phi_d + s_b))^2 / 2(\ln(s_b))^2\}.$$

$$s_b = 10 \text{ for VV; } (2 + s_c) \text{ for HH}$$

The near incidence factor $C(\phi_g)$

$$C(\phi_g) = (100/s_c(2\pi)^{.5}) * \exp\{-(\phi_d/2s_c)^2\}$$

$$s_c = (13 + 1.3 w)^{.5}$$

w = wind speed for sea state in knots

Values of Water Wavelength λ_w , Wave Period t_w and Wind Speed w as a function of Sea State and Polarization (Open Sea)

	Water Wavelength			Water Period (sec)	Wind Speed (knots)
	λ_w (feet)	λ_w nom	λ_w max		
	λ_w min		t_w nom	w nom	
Sea State 1	--	10	20	1	5
Sea State 2	20	40	70	2.8	9
Sea State 3	70	90	110	4	13
Sea State 4	110	140	190	5	17
Sea State 5	190	230	260	6.3	21

velocity which is much faster than the velocities of water mass in deeper water caused by orbital motion. Finally, the foam and spray is more dense in the shallower water creating more spread in the observed velocities.

No radar measurements of these phenomena were found during this study and it is suggested that measurements be obtained if performance at the land-sea interface is important. In the absence of data, the trends described above are presented by modeling the mean amplitude from sea within 1000 feet of land as twice the value for the sea state in the adjacent deeper water. The power of the return is evenly split between two velocity components. The first component has the same mean and standard deviation as that for deeper water. The second component will have a mean velocity = $(gd)^{.5}$ where g is 9.8 meters/sec² and d is the wave height associated with the sea state in deeper water. The spectral spread is the same as that given for deeper water.

2.1.3 Terrain Clutter

The three types of distributed terrain are modeled: farmland, forests and mountains. The expected value of the mean reflectivity from each type varies as a function of grazing angle with a Gaussian shape near vertical incidence and a constant gamma model in the plateau region and lower angles. The near-incidence factor $C(\phi_i)$ can be given by

$$C(\phi_i) = 10 \log((C1/\lambda) (1/s_c(2\pi)^{.5}) * \exp{-(\phi_i/2s_c^2)})$$

where $\phi_i = 90 - \phi_g$, $s_c = 10$, scale factor $C1$ is 50 for farmland and woodland and 10 for mountainous regions and λ is the wavelength in meters. The proposed constant gamma values are .2, .1 and .032 for mountains, forest and farmland respectively.

The variation of the mean reflectivity about the expected value is defined to be gamma, resulting in a K distribution for the instantaneous reflectivity. The shape parameter k is a function of both resolution cell size and grazing angle and is given by

$$k \sim (R\theta_a/D_r) (c\tau/2D_r) \phi_g^2$$

for farmland and forest and

$$k \sim (R\theta_a/D_r) (c\tau/2D_r) (\phi_d - \phi_h)^2$$

for mountains where ϕ_d is the depression angle, ϕ_g is the grazing angle and ϕ_h is the depression angle at the horizon. For grazing angles below 10 degrees, a the "macro-shadowing" noted in mountainous regions is modeled by patches similar to the ARSR-4 model where P_1 , the probability that a resolution cell will contain a patch of strong clutter, is given by

$$P_1 = \exp[-\ln(2) (R/100)^2]$$

and R is the range to the resolution cell in nm. $P_2 = 1 - P_1$ is the probability that the return from the resolution cell will be dominated by thermal noise.

The range of temporal fluctuation from terrain can be described by a Rician density function

$$p(\sigma_o(t)/\sigma_0) = (m^2 + 1) \exp[-\sigma_o(m^2 + 1)/\sigma_0] \exp[m^2] I_0[2m((m^2 + 1)(\sigma_o/\sigma_0))^{.5}]/\sigma_0$$

where m^2 is the DC-to-AC ratio, σ_0 is the mean reflectivity value of the cell and $I_0[]$ is the modified Bessel function of the first kind of zero order. For mountains, m^2 is 27 for all wind conditions. For farmland and forest, m^2 is 27 for calm winds, 5 for light winds (~ 5 knots), ~1 for 20 knot winds and ~0 for winds over 30 knots.

The spectral density function for farmland and forest terrain is given by

$$S(f) = m^2/(1-m^2) \delta(f) + a\lambda/[1+(|f|\lambda/b)^n]$$

where λ is the wavelength in meters, b is a function of wind speed and vegetation type as given in Figure 5.7, $n = 4$ and a is a scaling factor such that the DC-to-AC power ratio is satisfied. For mountains, b can be assumed to be .046.

2.1.4 Manmade Structures

The manmade structures modeled include buildings, vehicles, and vessels. These structures make up much of the "discrete" clutter observed on the terrain and sea. The models assume that the density of structures is

proportional to the population density in each of five general regions: Atlantic, Pacific, Gulf Coast, Great Lakes and Interior. The RCS per square mile from the structures is a function of the number of buildings per square mile and the RCS per building. For the densely populated Atlantic Coast, the derived distribution of RCS per square mile is log-normal with a standard deviation of 7 dB and a median value of 45.5, 49 and 51 dBsm/nm² for UHF, L-Band and S-Band, respectively. Lesser values are given for the other regions.

The number and distribution of vehicles traveling on the roads at a given time is approximated by Table 2.8. With an average of 10 dBsm per vehicle, the RCS and velocity observed by ADI radar can be calculated for both highway and rural conditions.

	Urban Interstate Highway	Rural Interstate Highway	Rural Single-lane Roads
Traffic Flow/Hr	2400	660	50
Average Speed (mph)	50	55	50
Average Number of Vehicles/ lin. mile	48	12	1

Table 2.8 Summary of vehicle traffic for Interstate and Rural roads.

The average RCS of large ships can be related to its tonnage using

$$RCS = -12.8 + .5 f_{db} + 1.5 M_{db} \text{ (dBsm)}$$

where f is the frequency in Ghz and M is the tonnage. An exponential distribution is used to describe the ship tonnage with a mean of 10,000 tons. The average velocity of a ship is 10 knots. The fluctuation observed from a ship is log-normal with a standard deviation of 5dB.

2.1.5 Bird and Insect Angels

For L-Band and S-Band, the derived mean RCS density for bird flocks is log-normal with a median of -16 dBsm and a standard deviation of 6.5 dB. The derived angel RCS density for UHF is a Weibull distribution with a median of

-24 dBsm and a shape factor of .34. The variations about the mean for a single bird vary as a function of observation time. For intervals short relative to a wingbeat period ($t \ll$ a few milliseconds), the RCS is approximately constant. For intermediate time intervals containing several wingbeat period, but no aspect change, the RCS fluctuations will follow the wingbeat pdf, assumed to be an exponential distribution. For longer time intervals, the distribution function is a compound distribution where the wingbeat pdf is the conditional distribution and the aspect pdf is the independent distribution. The RCS variation about the mean from flocks with many birds follow an exponential distribution.

The distribution of bird angel velocities is given as

$$f(V_b) = (1/2V_o)(V_b/V_o)^2 \exp[-(V_b/V_o)]$$

where V_b is the velocity of a bird and V_o is 9 knots. The altitude distribution is exponential with a mean of 1500 feet. Other general characteristics as a function of height are given in Table 2.9.

Altitude Interval (kft)	% of angels	Heading changes (deg.)	Time Between Heading Changes
0-1	50	+180/-180	.1 sec to 60 seconds
1-2	25	+180/-180	1-5 minutes
2-4	20	+90 /-90	over 5 minutes
4-8	4.5	+30 /-30	over 5 minutes
8-16	0.5	+30 /-30	over 5 minutes

Table 2.9 Flight characteristics of bird angels versus altitude

The mean amplitude of a single insect is log-normal with a median = -41 dBsm - 40 log λ and a standard deviation of 6 dB where λ is the radar wavelength in cm. A log-normal density is recommended for the distribution of angel density. The recommended median is .001 per cubic meter and the standard deviation is 6 dB. This density exists in a 100 meter layer located at 300 meters and is zero elsewhere. The corresponding median areal density is $3.4 \cdot 10^5$ per nm^2 . The velocity of the insects is the environment winds given in Section 3.

2.1.6 Auroral Clutter Model

Auroral clutter is caused by backscatter from irregularities in the electron-density found in the ionospheric plasma. In this model, the aurora clutter comes from a 30 km thick layer located between 92 km and 122 km. The boundary is abrupt at the bottom and top of this layer. No studies on the spatial inhomogeneity or temporal nonstationarity were found although a few studies allude to such variability. In the absence of quantitative data on the spatial variability, this model will assume that auroral clutter within this layer is homogeneous.

The mean volume reflectivity from aurora can be given by

$$\eta_v(f_r, \alpha, \beta) = \eta_v(f_r) g(\alpha) \rho(\beta)$$

$$\text{where } \eta_v(f_r) = 32 \pi^4 r_e^2 N^2 |\Delta N/N|^2_{\max} = S_o \exp(-(f_r - f_o)/f_s)$$

$$|\Delta N/N|^2_{\max} = |\Delta N/N|^2_{f_o} \exp(-(f_r - f_o)/f_s)$$

$$r_e = 2.82 \times 10^{-15} \text{ meter} = \text{electron radius}$$

$$S_o = 32 \pi^4 r_e^2 N^2 |\Delta N/N|^2_{f_o} = 2 \times 10^{-8}$$

$$f_o = 400 \text{ Mhz}$$

$$f_s = 132 \text{ Mhz}$$

$$g(\alpha) = \exp[-\{\pi \cdot 5 AB \ln(10)/20\} \operatorname{erf}(\alpha/B)]$$

$$A = 10.2$$

$$B = 8.4$$

$$\rho(\beta) = 0.1 \exp(2.3 \cos^2 \beta)$$

β = flow angle as given in Figure 8.3.

Since the aurora is modeled as scatter from a large number of randomly positioned rods within the radar resolution volume, the pdf defining the fluctuation about the mean reflectivity is exponential. The temporal correlation properties of this fluctuation depends on the spread of auroral velocities illuminated by the antenna pattern. The radial or doppler velocity from a section located at angle β is

$$V_d = -\underline{V}_e \cdot \underline{k} / |\underline{k}|$$

where \underline{V}_e and \underline{k} are vectors defined in Figure 8.3 and $|\underline{V}_e| = 400 \text{ m/s}$.

2.2 Effects of Platform Motion

The effects of platform motion cause the observed clutter characteristics to differ from the intrinsic clutter characteristics given in this model. First, the mean frequency of the intrinsic spectra from each range-azimuth-elevation cell will be shifted by the mean doppler frequency f_d produced by the platform motion

$$f_d = (2v/\lambda) \cos \phi_d \cos \theta_a \quad \text{Hz}$$

where v is the relative speed of the aircraft with respect to the surface, λ is the wavelength, ϕ_d and θ_a are the depression angle and azimuth angle to the range-azimuth-elevation cell.

The observed spectral spread is a function of several factors related to platform motion. First, the spectral shape of the clutter return depends on the antenna and doppler filter sidelobes in the formed space-time beam and the azimuth extent and elevation extent of the clutter. Second, the motion of the aircraft changes the relative number of wavelengths to each scatterer in the resolution cell, broadening the spectra due to decorrelation. The time interval for decorrelation depends on whether the clutter is a collection of random scatterers or is dominated by a physically large discrete. A third component is the platform instability which is a function of weather and platform design. An equation defining the spectral shape of the different clutter types requires that all of the antenna, signal processing and platform parameters be defined.

2.3 Recommendations for Future Work

Several clutter sources or clutter-related phenomena that may present false alarm problems to an ADI system have not been modeled during this effort due to a lack of measurements at UHF through S-band and a lack of theoretical background. A brief list of these sources and phenomena are as follows:

- * the backscatter and spectra from fans, air conditioner compressors, car wheels and other rotating structures;
- * the frequency of occurrence and operational impact of elevated ducts.
(This includes any doppler spread and radar "holes" as well as extend range

effects. Some limited observations on the operational impact of ducting is given by Glaeser (1979);

- * the extent that airborne illumination will couple into a surface duct;
- * the frequency of occurrence, amplitude and doppler of dust storms, particularly in the Southwest;
- * the correlation of sea spike amplitudes with respect to carrier frequency;
- * the frequency of occurrence and backscatter from meteors.

Some of the models given in this report are based on conflicting or limited data and require further investigation. These areas are briefly given below:

- * the RCS of cars, trucks, buildings and other manmade objects at UHF through S-Band;
- * the doppler tails of wind-blown vegetation as a function of vegetation type;
- * the amplitude and doppler characteristics of the land-sea interface;
- * the correlation properties of K-distribution clutter with respect to sea state;
- * the change of amplitude density functions with respect to resolution cell size for all distributed clutter types.

3.0 TROPOSPHERIC CLUTTER

The tropospheric clutter reviewed in this section includes backscatter from precipitation, turbulent layers and local changes in the index of refraction. Each clutter type is treated as a volumetric scatterer where the backscatter or volume reflectivity is described as a random process. First, the scatter relationships are developed. Then, the general locations and movements of these scatterers are described. Finally the statistics of the volume reflectivity are provided including the mean and the variability of reflectivity with space and time.

3.1 Precipitation Clutter

Backscatter from precipitation has been studied extensively by the radar meteorological community. Numerous studies have been published periodically in conferences sponsored by the American Meteorological Society and have been summarized in Battan (1959), Battan (1973) and Doviak and Zrnic (1985). Most studies treat the precipitation as targets rather than clutter and their measurements do not usually correspond to those useful for clutter modeling. Two notable exceptions are Nathanson and Reilly (1968) and Gordon and Wilson (1983). Nevertheless, a significant amount of useful information can still be gleamed from these studies.

Some basic categories are rain (stratiform, thunderstorm and orographic), snow, hail and sleet. This model uses only the first two categories in modeling a wide-spread light-to-moderate distributed rain representing stratiform rains with embedded stronger thunderstorm cells. Each rain type is first modeled by a physical space-time structure which shows how the density and velocity of water mass varies in altitude and areal extent as a function of time. From these physical representations, the models of radar reflectivity and doppler are derived.

3.1.2 Reflectivity from a Volume of Rain

A simple model for a raindrop is a water sphere with diameters typically between 1 and 4 mm. From Mie theory (Mie, 1908, Battan, 1973), it has been shown that the backscatter cross section of a spherical drop is

$$(1) \quad \sigma = \pi(a/\alpha)^2 \left| \sum (-1)^n (2n+1) (a_n - b_n) \right|^2$$

where a is the drop radius, $\alpha = 2\pi a/\lambda$ and the summation is from $n = 1$ to ∞ . The a_n terms refer to the scattering arising from the induced magnetic dipoles, quadrupoles, etc. and the b_n terms refer to the electric dipoles, quadrupoles, etc.

For the UHF through S-Band range considered in this model, $\alpha < .2$ allowing the use of the Rayleigh approximation

$$(2) \quad RCS = \pi^5 |K|^2 D_i^6 / \lambda^4 \quad \text{meter}^2$$

where $|K|^2 \approx .93$, and D_i the drop diameter and λ are in meters. For a volume of such raindrops, a reflectivity factor Z is often used in radar meteorology

$$(3) \quad Z = \sum n_i D_i^6$$

where n_i = number of drops per unit volume and Z has the dimensions of mm^6/m^3 .

A more familiar expression to the military radar community is the volume reflectivity η_v where

$$(4) \quad \eta_v = \pi^5 |K|^2 Z / \lambda^4 \quad \text{meter}^2/\text{meter}^3$$

For many rains, the drop-size distribution can be approximated by (Marshall and Palmer, 1948)

$$(5) \quad N_D = N_o \exp(-bD)$$

where N_D is the number of drops in a unit volume with diameters in the interval D to $D+dD$, $N_o = .08 \text{ cm}^{-4}$ (empirically derived), $b = 4.1 r^{-0.21} \text{ mm}^{-1}$ and r = mean rainrate in mm/hr . Integrating equation (5), this drop-size distribution leads to the $Z-r$ relationship

$$(6) \quad Z = 296 r^{1.47}$$

This compares favorably with the empirically derived formulae for stratiform rain (Marshall and Palmer, 1948)

$$(7) \quad Z = 200 r^{1.6}$$

and thunderstorm rain (Jones, 1956)

$$(8) \quad Z = 486 r^{1.37}$$

as shown in Figure 3.1. Battan (1973) also lists several other empirical measurements of the Z-r relationship made prior to 1973. Except for orographic rains, the differences between the different formula are significant only for extremely low or high rainrates. While this difference may be significant when using radar to remotely measure rainfall, it is of little significance for models used in the evaluation of military radar systems. Since Equation (7) for stratiform rain is the one usually used for system designs in temperate climates, it will be the relationship used in this model for both rain types. This gives a relationship for volume reflectivity of

$$(9) \quad \eta_v = \pi^5 |K|^2 r^{1.6} / \lambda^4 \quad \text{meters}^2 / \text{meters}^3$$

$$= 5.69 \cdot 10^{-14} r^{1.6} / \lambda^4 \quad \text{meters}^2 / \text{meters}^3$$

The difference between this equation and that used in the ATR/ARSR-4 models is $|K|^2 = .93$.

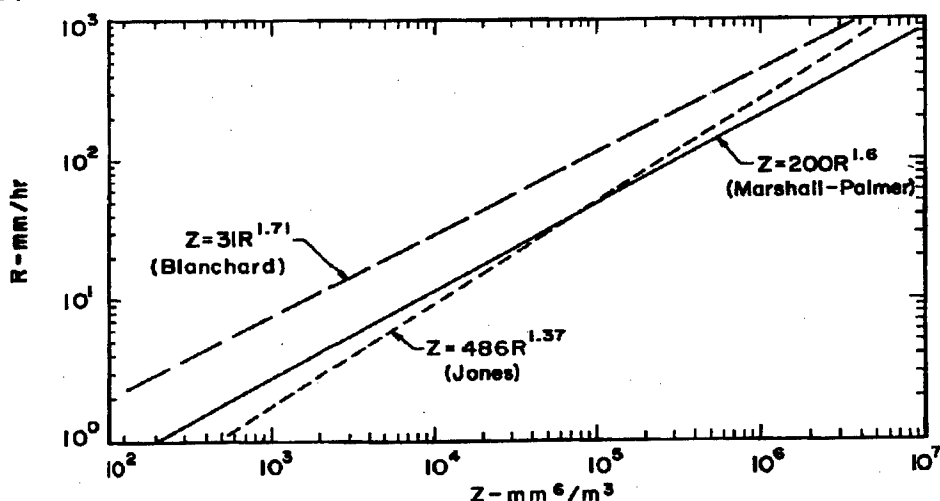


Figure 3.1 Comparison of different Z-r relationships (Battan, 1973)

3.1.2 Amplitude Fluctuations from a Volume of Rain

The received power from one raindrop can be given as

$$(10) \quad P_r = [P_t G^2 \lambda^2 / (4\pi)^3 R^4 \sum L_j] (\sigma_i) = J (\sigma_i)$$

where P_t is the transmitter power during the pulse width, G is the antenna gain, λ is the wavelength, R is the range to volume of raindrops, (σ_i) is the RCS of i th scatterer, $\sum L_j$ is the summation of the system losses and $J = [P_t G^2 \lambda^2 / (4\pi)^3 R^4 \sum L_j]$

When illuminating a large group of randomly distributed raindrops, the voltage received is the sum of the signals scattered by each of the scatterers with the phase of each signal taken into account. As the scatterers move randomly with respect to each other, the relative number of wavelengths from each scatterer to the radar (phase) will change and the received voltage will vary. After a period of time, the scatterers will assume relative positions such that the voltage received is uncorrelated with the previous voltage. Therefore, the backscatter power at any instant depends not only on the RCS of the scatterers, but also on their relative positions. If the received power is averaged over a large number of these "uncorrelated positions", this power can be given as

$$(11) \quad \bar{P}_r = J \sum (\sigma_i)$$

where the sum is taken over the volume containing the measured scatterers. If the scatterers are assumed to be uniformly distributed in a radar resolution cell, then

$$(12) \quad \bar{P}_r \sim J \eta_v R^2 \theta \phi c \tau / 2$$

where η_v is the reflectivity associated with the average rainrate in a cell, τ is the pulse width and θ and ϕ are the two-way horizontal and vertical beamwidths respectively.

One approach to describing this fluctuation is to treat the instantaneous backscatter power from a volume of scatterers as a random variable. Following the theory of fluctuating particles given by Marshall and Hitschfeld (1953)

and Wallace (1953), the density function of this instantaneous backscatter power is

$$(13) \quad p(P_r) = \exp(-P_r/\underline{P}_r)/\underline{P}_r$$

where \underline{P}_r is the average power associated with the average rainrate in the radar cell.

In this model, it is desirable to associate this fluctuation with a property of the weather clutter. Therefore, an instantaneous volume reflectivity is defined as a random variable such that

$$(14) \quad p(\eta_v) = \exp(-\eta_v/\underline{\eta}_v)/\underline{\eta}_v$$

While this model can state the mean values of rainrate and volume reflectivity, radar systems can only use estimates of this parameter. The average volume reflectivity can be estimated by averaging uncorrelated estimates of volume reflectivity. Several studies (Marshall and Palmer, 1953, Kerr (1951)) have shown that uncorrelated estimates can be obtained by shifting the carrier frequency by $1/\tau$. Experimental evidence from more recent studies (Nathanson and Reilly, 1967, Nathanson and Reilly, 1968, Nathanson, 1969) support this theory.

Uncorrelated estimates can also be obtained by averaging in time. The time interval required for the signal voltages to decorrelate depend on the shape and spread of the doppler spectra which, in turn, depend on the distribution of scatterer velocities within the resolution cell, the shape of the beam pattern and the wavelength of the radar. For Gaussian distributed spectra, theoretical studies (Atlas, 1964, Battan, 1973) show that

$$(15) \quad t_{0.01} = 1.71 \lambda/\sigma_v 10^{-3} \text{ (seconds)}$$

where $t_{0.01}$ is the time required for the autocorrelation function to fall to 0.01, λ is in centimeters and σ_v is the standard deviation in meters/second. For $\sigma_v = 1.0 \text{ m/sec}$, $t_{0.01} = 17.1, 42.75$ and 119.7 msec for wavelengths of 10, 25 and 70 cm, respectively. At least 10 uncorrelated samples are required to obtain a good estimate of $\underline{\eta}_v$. Therefore, for wavelengths of 10, 25 and 70 cm, at least .17, .43 and 1.2 seconds of data from a cell is required.

The time-averaging approach is of limited value when the number and size of the scatterers change during the averaging interval. It is well known that even wide-spread light rains are seldom uniform in intensity with respect to range and azimuth. Therefore, as the winds blow volumes of different rainrates through a radar cell, the mean volume reflectivity changes. As discussed in a later section, this change in reflectivity of a cell is treated statistically with the rate of change being a function of the spatial correlation function and structure of the rain type and the velocity of the rain.

3.1.3 Polarization Effects

Battan (1973) notes that the Z-r expressions referenced above were obtained by measuring raindrop spectra, not by radar reflectivity measurements. The rainfall intensity r was either calculated from the raindrop data or observed directly and the reflectivity factor Z was obtained by computing ΣD^6 in a unit volume. Since a spherical model was used to calculate the cross section of a drop, the HH return and the VV return would be equal and the same sense return for circular polarization would be zero.

Measurements of water droplet shapes indicate that small water droplets tend to be nearly spherical. Large water droplets falling at their terminal velocities have oblate shapes with axial ratios that oscillate from .1 or .2 to values close to 1. Measurements by Wexler (1955) indicated axial ratios of 0.4 in snow, .5 in the melting (bright band) region and .75 in rain leading to cancellation ratios of -18 dB for snow, -15 dB for the bright band and -20 dB for rain. Similar measurements by Newell et al. (1955) obtained cancellation ratios of -19 (limited by the antenna) to -13 dB for snow, -16 to -7 dB for the bright band and -19 to -12 dB for rain. Of particular note, the cancellation ratios were not found to be a function of Z . Based on these measurements, the recommended ratio of the volume reflectivity for the same sense circular polarization and linear polarization is the same as that given in the ATR/RSR-4 models: -10 for the bright band and -15 for precipitation above and below the bright band.

3.1.4 Statistical Occurrence of a Rain Rate within the Radar Search Volume

Rainrates on the ground are measured by the volume of water collected over a period of time. Measurements over an hourly period are referred to as "clock hourly" rainrates while measurements over a shorter period, such as 1 minute, are referred to the "instantaneous" rainrate. Since the rainrate in a radar resolution cell can change rapidly, the statistics of instantaneous, not clock-hourly, rainrates are useful to predicting the statistics of radar volume reflectivity. However, the knowledge of point, horizontal and vertical distributions of instantaneous water fields is severely limited. Most rain rate measurements occur only at the surface and can not measure the water mass stored in the atmosphere that would represent clutter to an air surveillance radar. Figures 3.2 and 3.3 show that even moderately strong storms can store a large amount of water mass at much higher densities than observed at the surface. Furthermore, most surface rainrate measurements are "clock-hour" measurements. When high rainrates do occur at the surface, they usually occur for a short duration and are associated with fast moving systems. Therefore, they are over a point for only a fraction of an hour and their frequency of occurrence is severely underestimated by clock-hour data.

Several studies have attempted to relate the instantaneous rainrate statistics with the statistical occurrence of precipitation echoes existing at a weather radar site and the clock-hour rates measured at various locations. The probabilities of precipitation echoes existing within 100 nm was studied by Grantham and Kantor (1967). This report presented the frequency of occurrence of precipitation echoes observed at 30 weather radar stations in the US over a two-year period. For 6 sites in representative locations of the US, the probabilities of the azimuthal widths of echo-free sectors within a 100nm radius were also presented. Bussey (1950) suggested a relationship between clock-hour rates and instantaneous rates and proposed that the instantaneous rates measured at a point are similar to the instantaneous rates existing along a path. Other studies (Winner 1968, Lenhard et al 1971, Burroughs 1967) have shown that regions with similar climates and rainfall statistics would have similar instantaneous rainrate statistics. Recent studies justify this general approach (Jones and Sims, 1978, Crane, 1980, Grantham et al, 1983, Feldman, 1979). Figure 3.4 presents a map of rain rate climatic regions for the U.S. where regions B thru F represent polar taiga, temperate maritime,

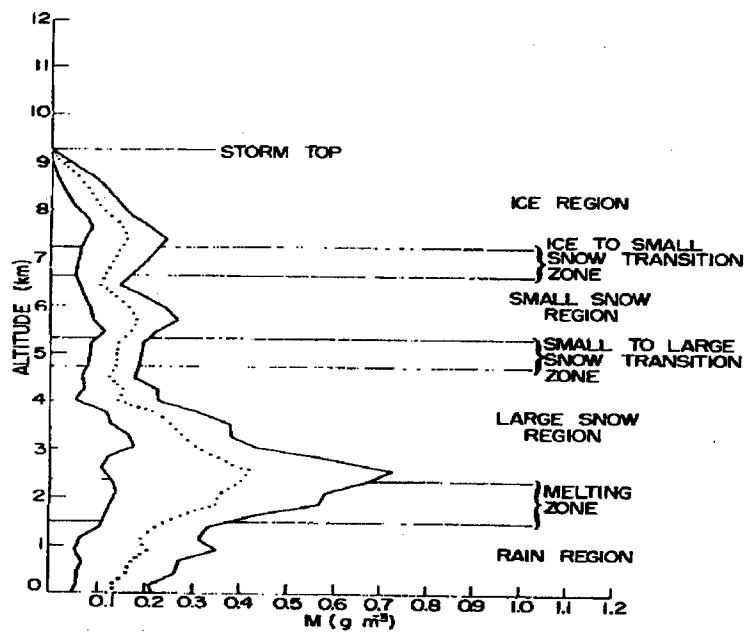


Figure 3.2 Liquid water content M vs altitude for stratiform storms (Grantham et al., 1983)

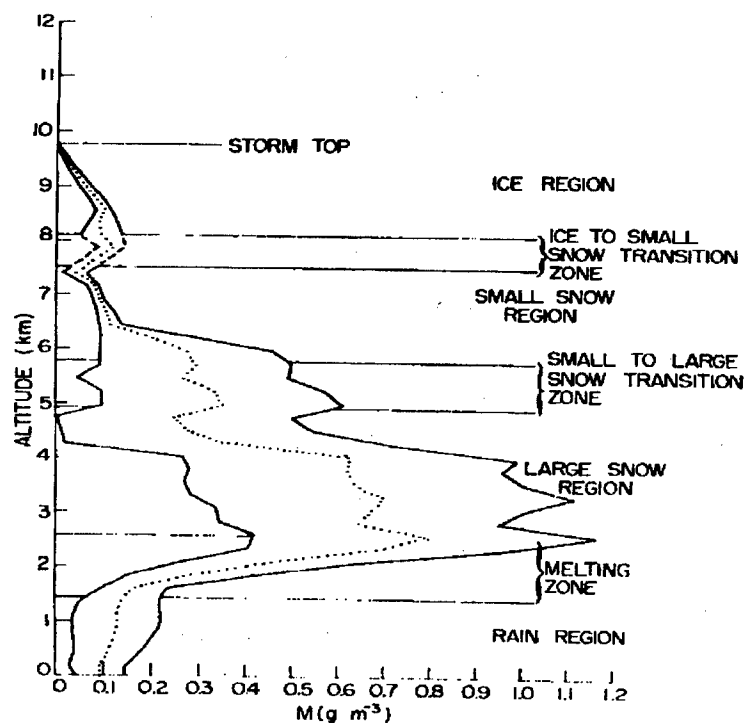


Figure 3.3 Liquid water content M vs altitude for convective storms (Grantham et al., 1983)

temperate continental, sub-tropical wet and subtropical arid respectively. The point rain rate statistics associated with these regions are given in Table 3.1.

O'Reilly (1971) investigated the relationship between clock-hour and instantaneous rainrate data for several US sites located in different climatic regions. Using raindrop camera and rain guage measurements performed under the sponsorship of the Illinois State Water Survey, composite clock-hour rates were derived from the instantaneous data. Then, for each interval of clock-hour rate, the percentages of an hour that the instantaneous rain rate exceeds given thresholds were determined. This provides the conditional probability of an instantaneous rain rate given that the clock-hour rate is within a stated interval.

Beals, O'Reilly and Davis, (1971) used the work of Bussey, Grantham et al, O'Reilly and the available clock-hour statistics to create a model for the evaluation of radar systems in weather. Various sites in the US and other regions of the world were associated with one of three general climatic regions: tropical, mid-latitude and high latitude. The statistics for these three regions were similar to the averages for the sub-tropical, temperate and polar regions given in Figure 3.4.

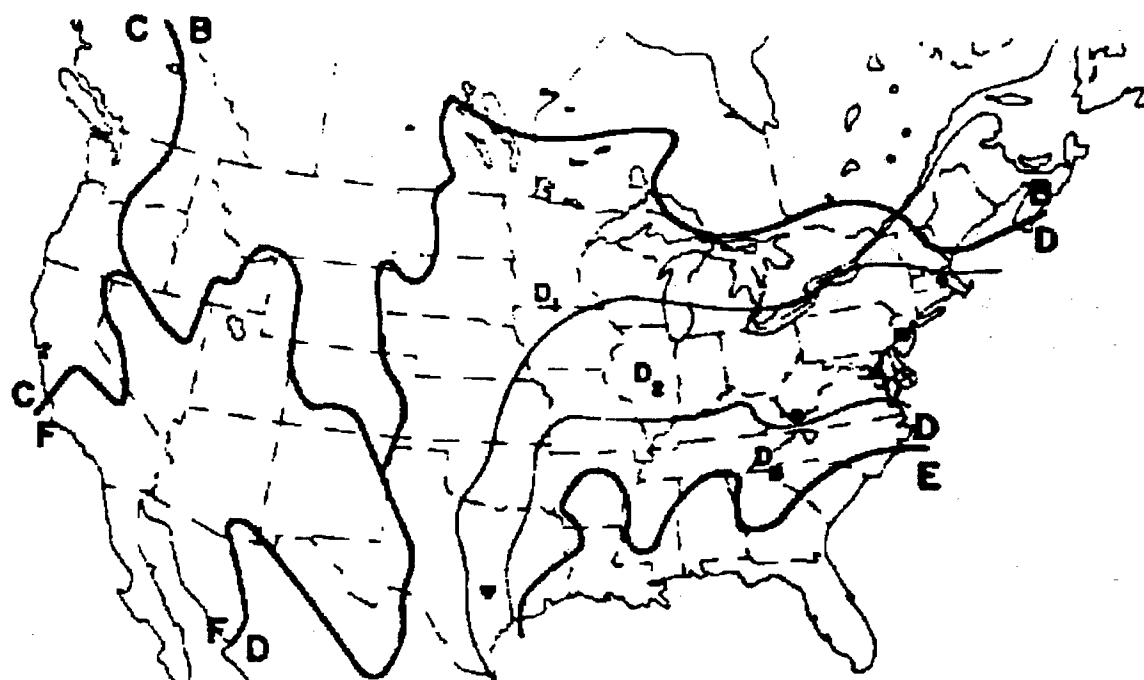


Figure 3.4 Climatic regions in the continental US (Crane (1980))

RAIN CLIMATE REGION

Percent of Year	B	C	D ₁	D ₂	D ₃	E	F
.001	54	80	90	102	127	164	66
.002	40	62	72	86	107	144	51
.005	26	41	50	64	81	117	34
.01	19	28	37	49	63	98	23
.02	14	18	27	35	48	77	14
.05	9.5	11	16	22	31	52	8
.1	6.8	7.2	11	15	22	35	5.5
.2	4.8	4.8	7.5	9.5	14	21	3.2
.5	2.7	2.8	4	5.2	7	8.5	1.2
1.0	1.8	1.9	2.2	3	4	4	0.8
2.0	1.2	1.2	1.3	1.8	2.5	2.0	0.4

Table 3.1 Point rainrate statistics for US climatic regions given in Figure 3.4 (Derived from Grantham et al (1983))

For each climatic region, the instantaneous rainrate statistics for a specific sites were obtained using the methodology given by O'Reilly (1971). The results were the instantaneous rainrate statistics along 20 nm and 100 nm radials for each interval of clock-hour rate measured at the site. Using the assumption that the rain is uniformly distributed in range, the percentage of area occupied by each instantaneous rainrate intensity within 20 nm and 100 nm radius were calculated. These areas were then represented by a number of raincells with diameters typical for the rainrate intensity.

The ATR (1981) and ARSR-4 (1985) models were based on this model and methodology. The ATR model used a European and an Asian site for the respective middle latitude and tropical sites, while the ARSR-4 (1985) model used the values for mid-latitude and sub-tropical U.S. sites. These results were revisited for use in the ADI model and the results are given in a later section.

3.1.5 Wide-spread Rain

The wide spread or distributed precipitation represents a low level rainrate that exists over a large area and generally moves with the local winds. The structure typically found in widespread rain is given in Figure 3.2. (Grantham et al, (1983)) It has three components, frozen precipitation above an altitude associated the freezing level, a bright band in the melting zone just below the freezing level and rain below the bright band.

The bright band is associated with a melting layer containing a mixture of ice and liquid water and has a significantly stronger volume reflectivity than the other two components. However, its vertical width is quite narrow. The vertical velocity of precipitation within most of the bright band and above is in the order of 1-2 m/s.

Rain exists below the melting layer and has a volume reflectivity that is 5 to 10 db less. Measurements by Caton (1964) revealed that this reflectivity changes very little with altitude below the melting layer. The vertical velocity of the rain is increased to typically 5 to 6 m/s.

Figure 3.2 indicates that the frozen precipitation above the melting layer has approximately the same liquid water content M as the rain below. However, because the dielectric constant is .21% of that of rain, the volume reflectivity approximately 6.8 dB less.

Measurements (Lhermitte and Atlas(1963)) indicate that other factors often cause the volume reflectivity above the melting layer to be even less. Figure 3.5 presents simultaneous profiles of the measured effective reflectivity factor Z_e and the particle fall velocity for stratiform precipitation. Z_e at 800m above the layer is 22.6 db less than the Z_e of the melting layer while Z_e just above the melting is about 15 db less. Since only 6.8 db could be attributed to melting, Lhermitte and Atlas (1963) attributed the difference to more ice-crystal aggregation at the lower altitudes and throughout the melting layer.

Because Z_e for the frozen precipitation was much smaller than the other two, the ARSR-4 and the ATR models ignored it, defining the volumes above the melting layer as clear of precipitation. While this simplification had little impact on those procurements, this may not be true for ADI. Therefore, this model will define a liquid water content above the melting layer equal to that below the melting layer. This water exists as snow with a fall velocity of 2

knots. The volume reflectivity η_v can be calculated using Equation (9) and $|K|^2 = .197$. Other useful relationships between Z, liquid water content M, and r can be given as

$$(16) \quad Z = 3.8 \times 10^4 M^{2.2} \quad (\text{Douglas 1964})$$

$$(17) \quad M = .25 r^{0.90} \quad (\text{Gunn and Marshall 1958})$$

$$(18) \quad Z = 1800 r^2$$

The rainrate of stratiform rains is seldom uniform with time or range. This can be inferred from the spread of liquid water content given in Figure 3.2. Figure 3.6 presents the height-time record of stratiform rain as viewed by a vertically pointing radar. While the amplitude values are not given, it is clear that the rainrates of all three components vary significantly as the rain was blown over the site. Thus, it is reasonable to treat the rainrate and the mean volume reflectivity within a radar resolution cell as a random variable. Furthermore, if it is assumed that a fixed pattern is being moved at the wind speed of the generating level, then the probability density function (pdf) of rainrates observed in one cell as a function of time is the same as the pdf of rainrate with respect to range. While patterns of widely spread rains do change with time, they change little over the small time intervals used by most radar techniques. (Possible exceptions are trackers, threshold maps for land clutter and other similar processes that integrate data for several minutes.) Therefore, a quasi-static spatial pattern of mean rainrate is useful for the evaluation of radar system design.

The spatial inhomogeneity is modeled as a random variation about a mean value. The ATR and ARSR-4 models used 10 mm/hr for the mean rainrate of the bright band and 1 mm/hr for the rain below the melting layer. Referring to Figure 3.2, this bright band value is between the mean and upper standard deviation and is at a value appropriate for radar design. The rain intensity, however, is near the lower standard deviation. For ADI, the suggested mean rainrates are 10 mm/hr for the bright band and 2 mm/hr or $M \approx .13 \text{ gm/m}^3$ for precipitation below and above the bright band. Further discussion on the pdf and other statistics describing this spatial inhomogeneity is provided in Section 3.1.7.

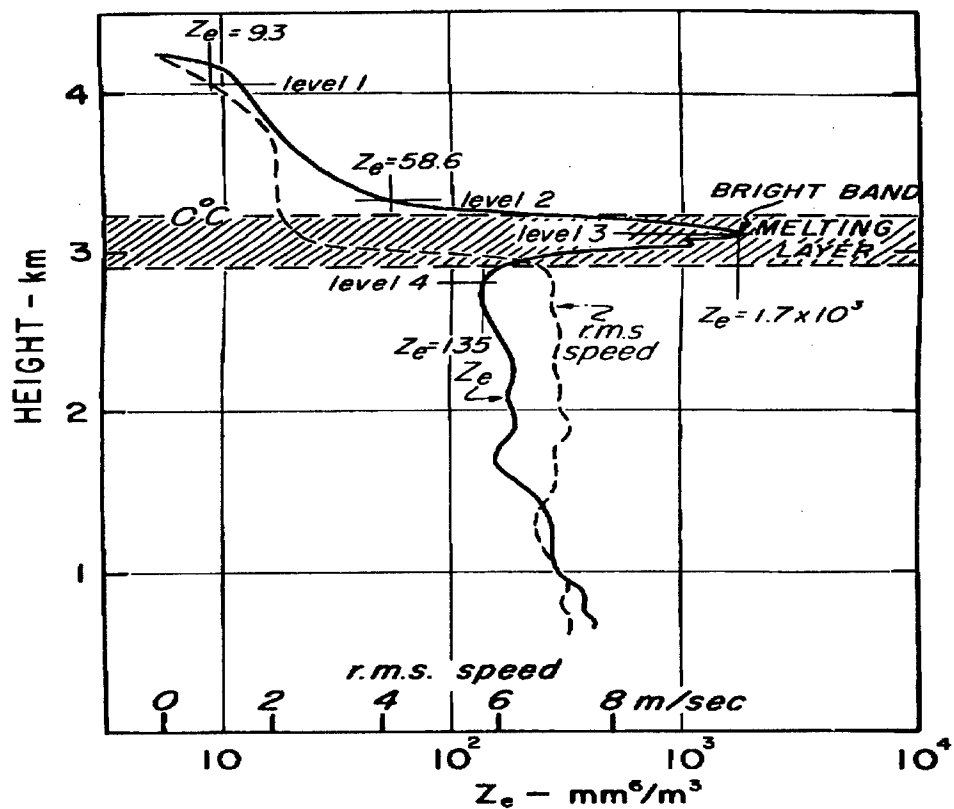


Figure 3.5 Profile of Reflectivity Values (Lhermitte and Atlas, 1963 as given in Battan ,1973)

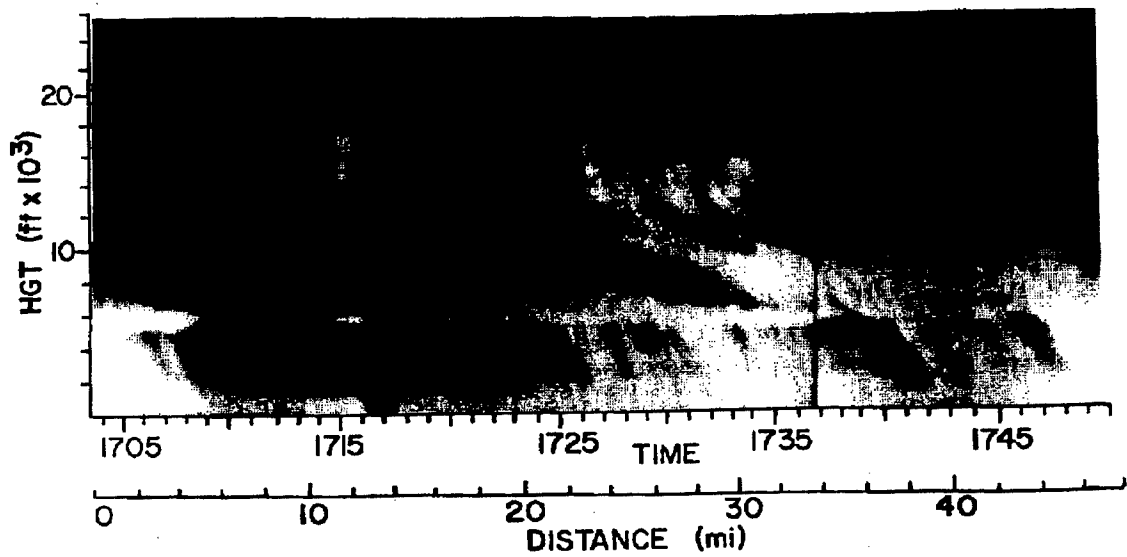


Figure 3.6 RHI plot of wide-spread rain (Stormy Weather Group, McGill University as given in Battan, 1973)

3.1.6 Cellular Rain

Cellular rain describes convective and thunderstorm cells that are more intense, have shorter lifetimes and exist over smaller areas than distributed rain. The structure of cellular rain is also more complicated. Figure 3.7 presents the structure of a thunderstorm over its lifetime. When the atmosphere is unstable, a volume of air having an upward displacement for any reason will continue to move upward at an accelerating rate. A cloud will form when a sufficiently large mass of moist, unstable air rises. Early in the growth in the cloud, the air motions along the periphery of the strengthening updraft are mostly a series of rising, rolling eddies. As the cloud grows, size of the precipitation particles grow until the mass becomes too large to be maintained, causing a downdraft. During its mature stage, a thunderstorm cell can have updrafts and downdrafts side-by-side. Isolated cells formed in environments with little vertical wind shear have structures similar to Figure 3.7c. More intense storms with strong winds at the generation level have structures similar to Figure 3.7d. In the later stages, the updraft becomes weaker and the intensity of the storm dissipates as the precipitation falls out. Storm cells typically travel in clusters with adjacent cells at different stages of development.

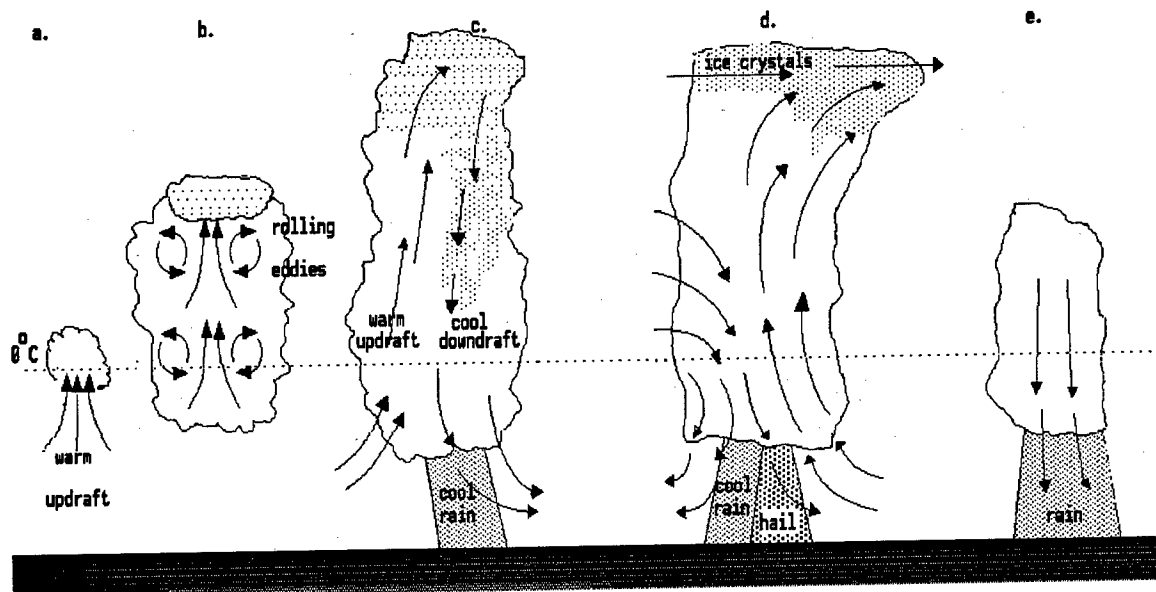


Figure 3.7 Life Cycle of a Thunderstorm

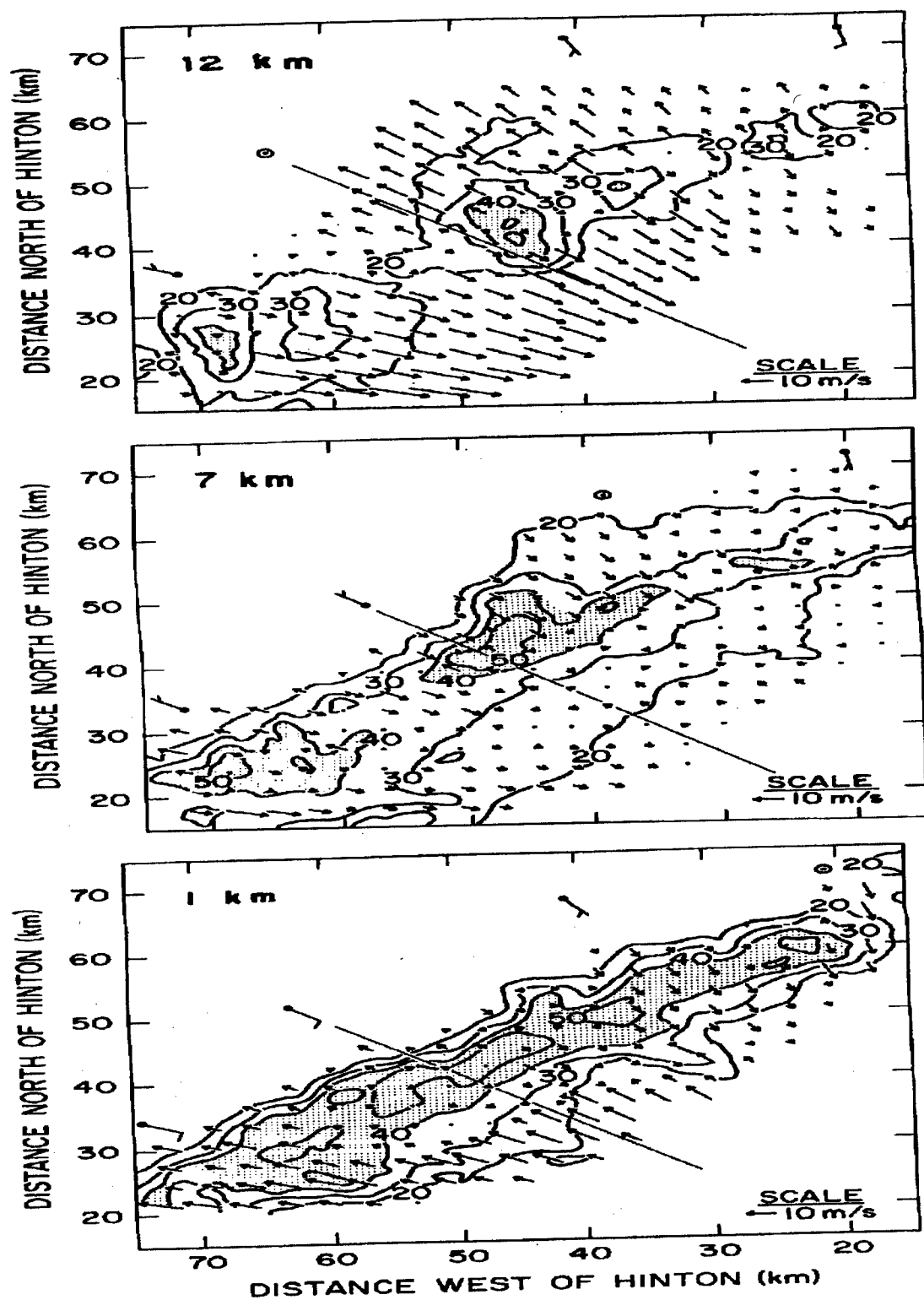


Figure 3.8 Radial and Wind Profiles of storm given in Figure 3.8 at Three Altitudes (Hjelmfelt and Heymsfield, 1981)

Storms as shown in Figure 3.7d can display large directional and velocity shear as a function of altitude. Figure 3.8 shows typical radial velocity and reflectivity fields from such a storm at altitudes of 1, 7 and 12 km (Hjelmfelt and Heymsfield 1981). At 1 km, there is a strong wind component into the southwest part of the storm from the southeast. At the northeast part of the storm, the winds are in the opposite direction, suggesting a cellular structure not apparent by the reflectivities.

At 7 km, the reflectivity pattern clearly shows separate discrete cores. The radial velocities have variations along the storm which are also indicative of a cellular structure. The areas of high reflectivity at 12 km indicate that large precipitation particles were carried to appreciable heights in this storm.

Figure 3.9 shows an RHI display taken along the line indicated in Figure 3.8. The storm's structure is very similar to that presented in Figure 3.7d. At the lowest level, the strong inflow from the front is opposed by winds of a gust front diverging from under the high reflectivity core. At a slightly higher level, the inflow penetrates deeper, suggesting a sloping updraft. Inflow from the rear is found at the mid-levels with strongly divergent flows at the higher levels.

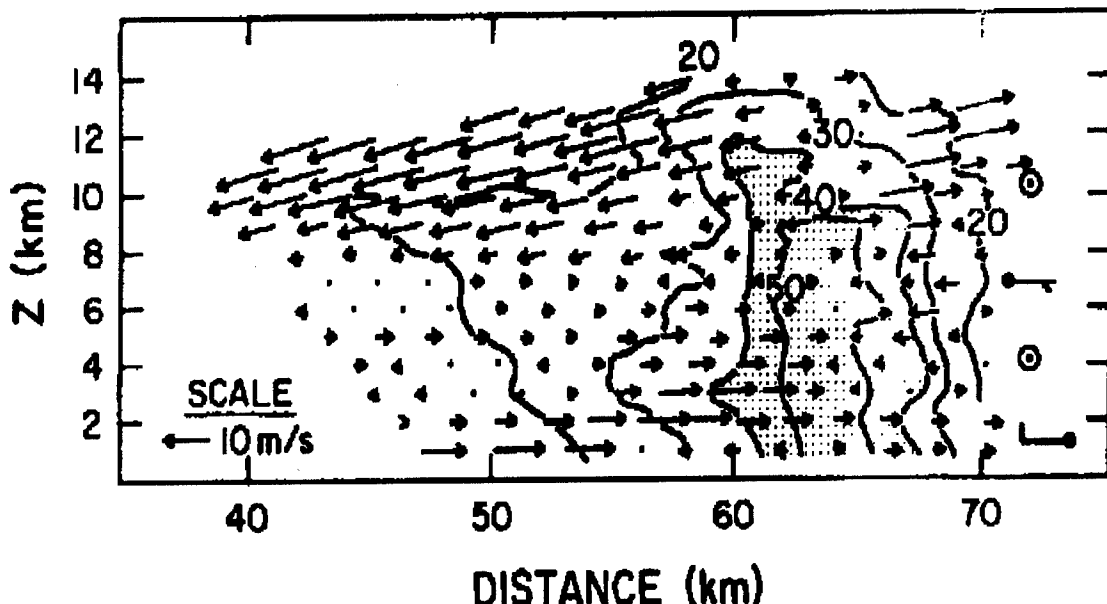


Figure 3.9 RHI plot of wind and reflectivity from a convective storm (Hjelmfelt and Heymsfield, 1981)

Figures 3.8 and 3.9 present only a "snap-shot" of one time interval in the life of one storm. Many studies have presented similar "snap-shots" for similar storm cells each with different reflectivity and velocity profiles and a simple model useful for the evaluation of radar designs can only crudely approximate some of these observed features. For ADI, the suggested model has two scales of spatial inhomogeneity. The large scale inhomogeneity is deterministic and is represented by defining a cellular structure for the heavier rainrates as given in Figure 3.10. The intense rain is confined to a cylindrical core of height H and diameter D . The values for H and D versus average core intensity are given in Table 3.2 for mid-latitude and tropical environments.

The small scale inhomogeneity within the core is a random variation about the given average value. As for the widely spread rain, the spatial inhomogeneities are considered to be static over small periods of a couple of minutes. Further discussion on the pdf and other statistics describing this spatial inhomogeneity is provided in the next section.

Around and above each core, the rainrate gradually decreases with distance from the core. The rates of change or gradients in reflectivity with respect to range have been estimated by Drufuca and Zawadzki (1983) and Torlaschi and Humphries (1983). Torlaschi and Humphries (1983) performed measurements of the gradients of $G = \text{Log } Z$ in both the down range and azimuth or cross range directions. Their results are given in Figures 3.11a and 3.11b. The S-band data used corresponded to weather returns at a height of 3 km. Each sample represents an average over 1 km in range (4 - 1.75 usec. samples) and 1 beamwidth in azimuth (10 pulses over 21 msec). At the shorter ranges where the azimuth and range resolutions were comparable, both the distribution of the gradient in cross-range G_x and the gradient in down range G_y seem to follow an exponential distribution. At longer ranges, the distribution of G_x in azimuth narrows drastically due to spatial averaging. The spatial averaging effects of G_y with respect to increasing range is not as severe. Torlaschi and Humphries (1983) estimated the mean gradients to be between 5 and 7 dBZ/km (9.25 and 12.95 dBZ/nm). However, they note that these mean values underestimate the actual reflectivity gradients due to the non-coherent integration in range.

The ADI model given in Figure 3.10 uses a falloff rate of 10 dBZ/nm in range and cross-range. This value differs from those used in the ATR and ARSR-4 models which used falloffs expressed in mm/hr/nm. The ATR and ARSR-4

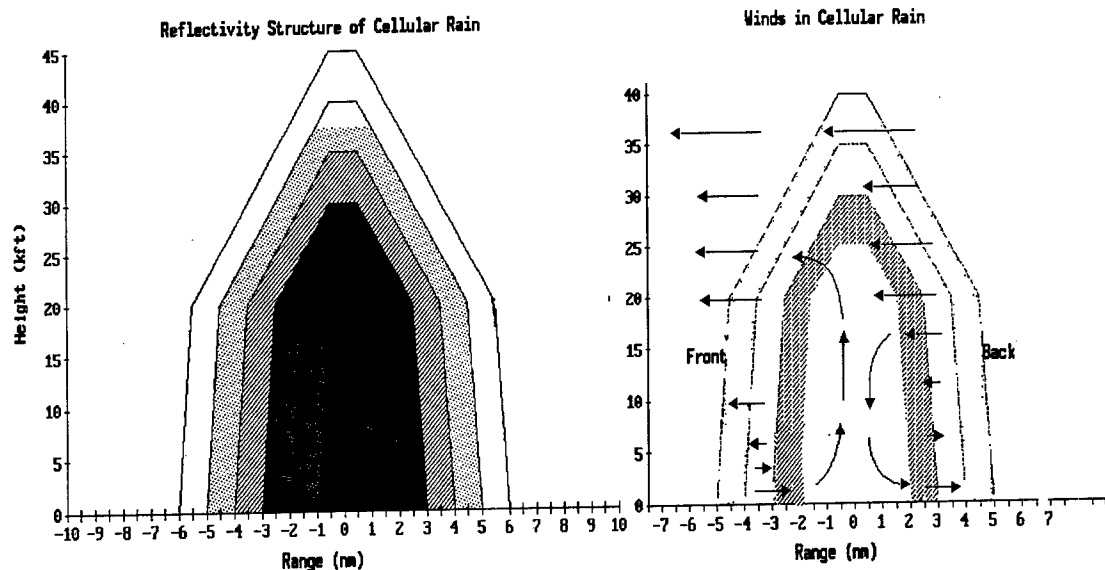


Figure 3.10 Model of storm reflectivity and wind structure

	MIDDLE LATITUDES	TROPICAL LATITUDES
Cellular Precipitation		
* Core height (ft)	0 - 15,000	0 - 20,000
* Number of cells within 200 nm storm	172	211
* Spatial distribution of cells	Uniform	In uniformly distributed clusters
* Cluster size	N/A	400 nm ²
* Cell Size and Rainfall Rate		
Mean Rainfall Rate (mm/hr)	Number of cells	Diameter (nm)
3.5	51	3.1
9.0	58	2.8
18.0	50	2.4
35.0	10	1.6
70.0	3	1.2
175.0	2	.7
350.0	---	---
		Number of cells
		Diameter (nm)

Table 3.2 Number, diameter, height and spatial distribution of cellular rain

rainrates prior to 1981. Comparing the two models, the log relationship presents sharper reflectivity boundaries at higher rainrates and gentler boundaries at lower rainrates. Similarly, a review of the literature indicates that a more appropriate falloff rate in height is 2 dBZ/kft rather than the 1-1.5 mm/hr used in the earlier models.

The wind structure presented by Figures 3.8 and 3.9 would present a large shear to an air defense radar throughout the storm regardless of aspect, especially when the vertical beamwidth is broad enough to illuminate most of the core. An airborne ADI system will probably have vertical beamwidths ranging from a minimum of about 3 degrees at S-Band to over 15 degrees at UHF. Thus an S-Band system will fully illuminate a 15,000 foot core at 50 nm while a UHF system will do so at 10 nm. For this reason, the model for spectral spread is relatively constant with respect to aspect as in the ARSR-4 model.

The equations for calculating this spread are given in Table 3.3. The mean velocity of the cell structure is 20 knots in the same direction as the environmental winds. Below 20 kft, a wind shear with respect to both speed and direction is present within the cell and the extended edges. A constant velocity shear exists for the back and the sides with a slightly different shear in the front. Above the cell core between 20 and 34 kft, the wind speeds are constant but the direction changes uniformly in the direction of the environmental winds. Above 34 kft, the environmental winds dominate.

3.1.7 Distributions and Correlation Functions of Rainrate and Volume Reflectivity

The "instantaneous" volume reflectivity η_v from a radar resolution cell containing rain is given as

$$\eta_v = |(\sum (\sigma_i)^{.5} \exp(j\psi_i))|^2/V \quad \text{meters}^2/\text{meters}^3$$

where σ_i is the radar cross section of raindrop i , $\exp(j\psi_i)$ contains the phase change and phase delay due to distance from the radar, V is the volume of the radar resolution cell and the summation is over all of the raindrops in the cell. The "mean" volume reflectivity $\bar{\eta}_v$ is given by

$$\bar{\eta}_v = 5.69 \cdot 10^{-14} r^{1.6}/\lambda^4 \approx \sum \eta_v / N_s \quad \text{meters}^2/\text{meters}^3$$

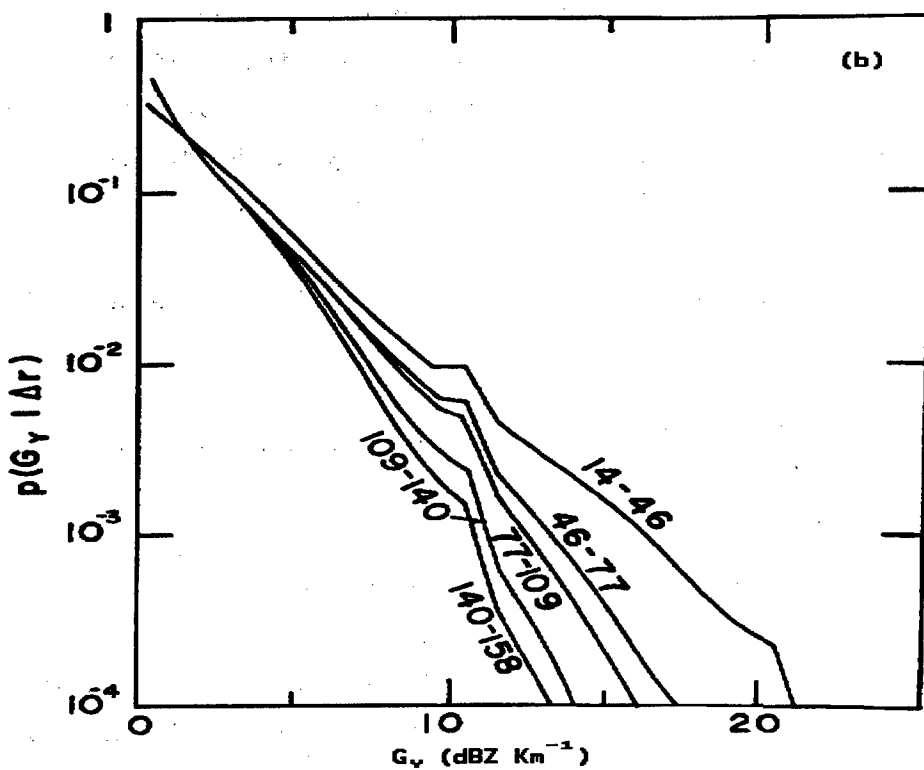
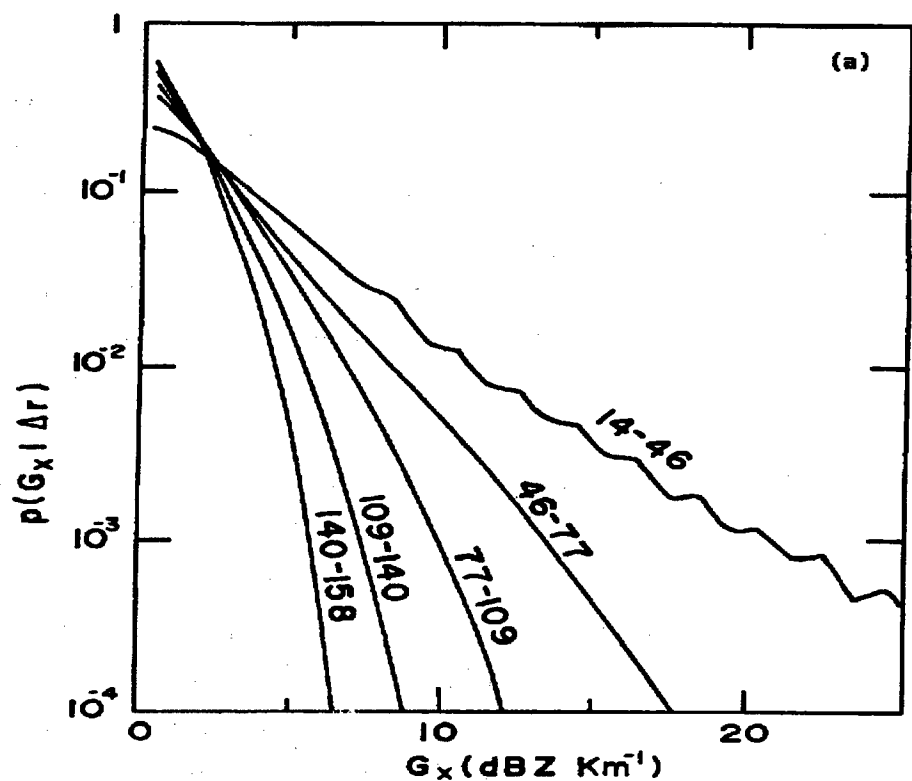


Figure 3.11 Measured density function of reflectivity gradients in the cross range (a) and the down range (b) directions. (Torlascji and Humphries, 1983)

* ENVIRONMENTAL WINDS IN CLEAR WEATHER OR IN DISTRIBUTED RAIN

* Mean Velocity = 10 knots, gusting to 20 knots $h < .2 \text{ kft}$

* Mean Velocity = $10 + \text{SHR1} * h$ (knots) $.2 \text{ kft} < h < 20 \text{ kft}$

* Mean Velocity = $20 + \text{SHR2} * (h - 20)$ (knots) $20 \text{ kft} < h$

SHR1 = .5 knots/kft; SHR2 = 1.7 knots/kft

* WINDS IN CELLULAR RAIN

At the front quadrant of the storm, the mean velocity V as a function of altitude is given as

$$V_{\text{front}} = \text{SHR3} * (h-3) \text{ (knots)} ; \text{SHR3} = 2.55$$

For the back of the storm,

$$V_{\text{back}} = \text{SHR4} * (h-10) + 20 \text{ (knots)} ; \text{SHR4} = 2.35.$$

where the sign of the velocity for both equations is relative to the environmental winds.

For the side quadrants,

$$V_{\text{side}} = j \text{SHR4} * (h-10)$$

where $j = +1$ for one side and -1 for the other. In this case, the sign represents the velocity relative to the storm center.

Above the cell core between 20 kft and 34 kft, the wind velocities are constant, but the direction of the side winds slowly change uniformly in the direction of the environmental winds. Above 34 kft, the environmental winds exist.

For rain illuminated by a complete Gaussian antenna pattern, the spectral shape of the rain will be Gaussian with a standard deviation σ_r given as

$$\sigma_r = [(TURB)^2 + (FALL)^2 + (WIND SHEAR)^2 + (BEAM)^2]^{.5}$$

where

TURB = standard deviation of the wind turbulence = 1.4 (knots)

FALL = s.d. of the fall velocities = $2 |\sin \phi_e|$ (knots)

BEAM = s.d. of the beam spread = $.42 V \theta |\sin \theta_w|$ (knots)

WIND = s.d. of the vertical wind shear

SHEAR = $2.55 * (\text{SHRx}) * R \phi \cos \phi_e |\cos \theta_w|$ (knots)

SHRx = shear values given in above for $x = 1, 2, 3, 4$

R = Range in nm

ϕ = two-way elevation beamwidth (radians)

θ = two-way azimuthal beamwidth (radians)

θ_w = angle between wind direction and the center of the beam (radians)

ϕ_e = elevation angle

V = mean velocity at the center of the beam (knots)

h = altitude, (kilofeet MSL)

Table 3.3 Velocity Relationships

where the summation is taken for $N_s > 10$ uncorrelated samples. Since the raindrops can be assumed to be randomly positioned,

$$\bar{\eta}_v = \sum \sigma_i$$

and

$$\eta_v = \bar{\eta}_v |\sum \exp(j\psi_i)|^2$$

Rainrate r and the corresponding mean volume reflectivity $\bar{\eta}_v$ is spatially inhomogeneous. This is reflected in the examples for widely-spread and cellular models given in Sections 3.1.5 and 3.1.6, respectively. A deterministic structure is given for the large scale inhomogeneity of cellular rain. The small scale variation within the cellular cores and throughout the wide-spread rain is represented by a random variation about an average rainrate r and its associated reflectivity value $\eta_r = E(\eta_v)$ where $E(\eta_v)$ is the expected value of η_v within the cellular core. If the pdf of η_v over a range-azimuth interval is $p(\eta_v)$, the pdf of the instantaneous volume reflectivity $p(\eta_v)$ with respect to range and azimuth can be given as a compound distribution

$$p(\eta_v) = \int_0^{\infty} p(\eta_v/\bar{\eta}_v) p(\bar{\eta}_v) d\bar{\eta}_v$$

The conditional pdf $p(\eta_v/\bar{\eta}_v)$ represents the fluctuation observed due to the random position and motion of N raindrops in a resolution cell where N is proportional to the cell's mean reflectivity $\bar{\eta}_v$. For practical long-range air defense systems, N is always large and $p(\eta_v/\bar{\eta}_v)$ is accurately described by the exponential function. Since the rain moves through space, the temporal statistics from one range-azimuth cell will have the same pdf as the spatial statistics.

The functional forms of $p(\eta_v)$ and $p(\bar{\eta}_v)$ are not obvious from current meteorological theory. In this model, $p(\bar{\eta}_v)$ is given as a gamma density function

$$p_k(\eta_v) = [k^k \eta_v^{k-1} \exp(-k\eta_v/\eta_r)] / \{\Gamma(k)(\eta_r)^k\}$$

and $p(\eta_v)$ is given as a K-distribution (Jakeman and Pusey, 1976, Lewinski 1979)

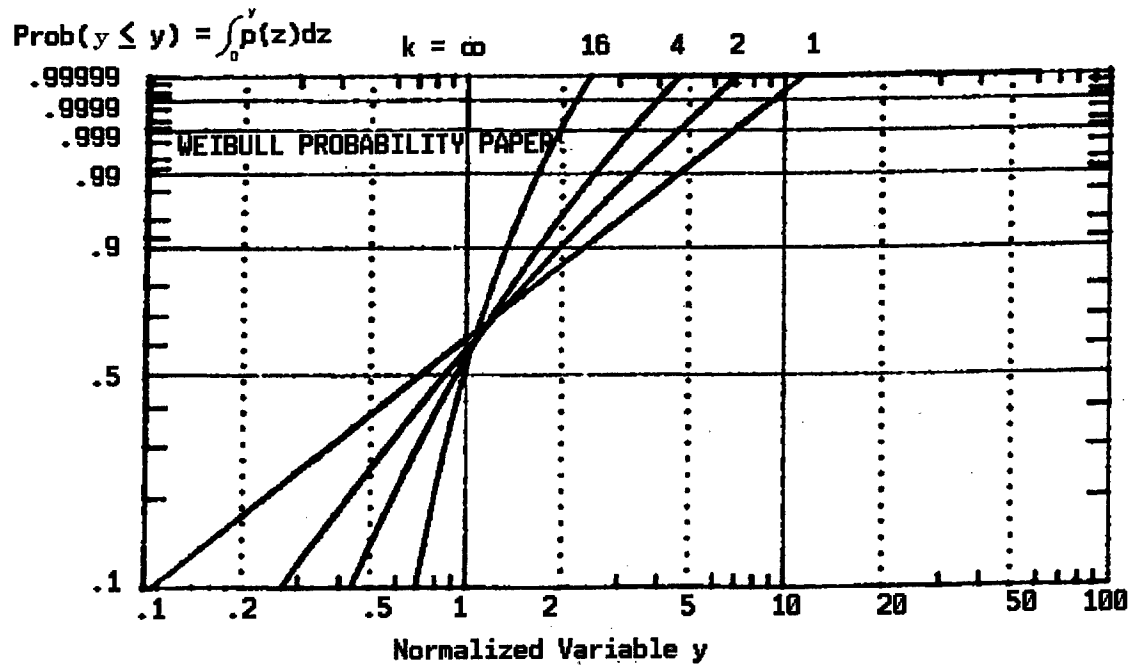
$$p(\eta_v) = [2k^{(k+1)/2} \eta_v^{(k-1)/2} / \eta_r^{(k+1)/2} \Sigma(k)] K_{k-1}[2(k\eta_v/\eta_r)^{1/2}]$$

where $K_v()$ is the modified Bessel function of the second kind of order v. Figure 3.12 show the shape of the gamma and K distributions for various values of k.

From a theoretical viewpoint, the number of raindrops in a volume depends on the rate of immigration from and to adjacent volumes and the combination or breakup of raindrops as they fall through the volume. This process is similar to the birth-death-immigration problem which Jakeman (1980) shows can lead to K distributed fluctuations.

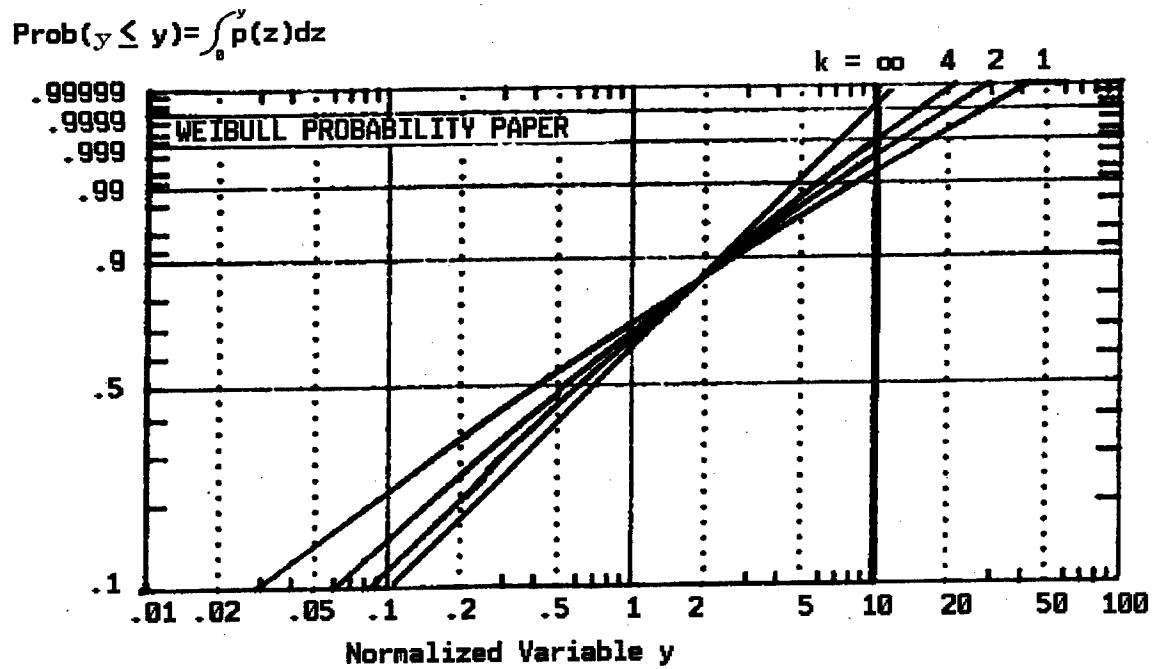
This choice of distribution is also supported by the few published measurements of weather reflectivity distributions. Sekine (1979) and Sekine et al (1981, 1984) reported that the amplitude (voltage) distributions of envelope-detected weather clutter over several range and azimuth sectors fit well to a Weibull distribution. Sekine (1979) reported fitted Weibull shape factors (voltage) ranging from 1.25 to 2.00 (Rayleigh) with an average value of 1.77. Sekine et al (1984) reported Weibull shape factors (voltage) ranging from 1.654 to 2.00 with an average of 1.844. These values were measured for resolution cell sizes ranging from .2 to .3 nm².

As pointed out by Jakeman (1980), the Weibull and K distributions are very similar for Weibull shape factors in this range. The appropriate K distribution and gamma shape parameters can be estimated by matching the standard deviation-to-mean ratios to the Weibull parameters given by Sekine. As the Weibull shape factor c approaches 2.00 (1.00 for power pdf), k approaches infinity meaning that the spread of the gamma density function $p(\eta_v)$ approaches 0 about η_r . Therefore, those weather sectors with c = 2.0 (1.0 for power) have a constant mean value through the sector and represent a homogeneous condition. In contrast, when c = 1.844 (.922 for Weibull power density), k = 7.54 for the matching K distribution for η_v . In this case, $p(\eta_v)$ has significant spread about η_r indicating a non-homogeneous condition where η_v varies with respect to range.



$$p(y) = k^k y^{k-1} \exp(-ky) / \Gamma(k) \quad y = \sigma_0 / \sigma_0 \text{ or } \eta_r / \eta_r$$

NORMALIZED GAMMA DISTRIBUTION



$$p(y) = \frac{2k^{\left(\frac{k+1}{2}\right)} y^{\left(\frac{k-1}{2}\right)}}{\Gamma(k) x} K_{k-1}(2\sqrt{ky}) \quad y = \sigma_0 / \sigma_0 \text{ or } \eta_r / \eta_r$$

$$x = \sigma_0 \text{ or } \eta_r$$

NORMALIZED K DISTRIBUTION

Figure 3.12 Gamma and K distributions for various values of shape parameter k

The parameter k depends on the size of the resolution cell and the distance between uncorrelated gamma samples. This distance is called the "correlation length". Physically, it can be interpreted as the distance between two volumes having a different number and size distribution of raindrops. The ARSR- 4 model used a formula where k was a function of resolution cell size. The suggested formula for ADI is

$$(19) \quad k = Rh(500*\tau)/D^2$$

where τ is the pulse width in usec, h is the two-way azimuth beamwidth in radians, R is range in feet and D is the correlation distance between uncorrelated samples of η_v in feet. By this equation, the correlation distance providing a value of k comparable to Sekine's average values is approximately 1100 feet. The only other measurement found during this study is one by Nathanson (1969) who reported longer correlation lengths ($\rho = .5$) of .6 to 1.4 nm in showers and 2 - 3 nm for "uniform" rain. In the proposed ADI model, a value of 1000 feet will be assumed for both distributed rain and within the cores of the cellular rain. Figure 3.13 shows how k varies with resolution cell size. Note that, for cellular rain, the size of the cell limits the maximum value of k .

3.1.8 Attenuation

Ryde (1946) studied the attenuation of microwaves by rain and showed the attenuation could be expressed as a function of rainrate. Wexler and Atlas (1963) computed the one-way attenuation as a function of rainfall rate for the raindrop-size distributions given by Marshall-Palmer for stratiform rain, Mueller and Jones (1960) for sub-tropical showers and Gunn and East (1954). The results for 1 mm/hr rainrates are plotted in Figure 3.14.

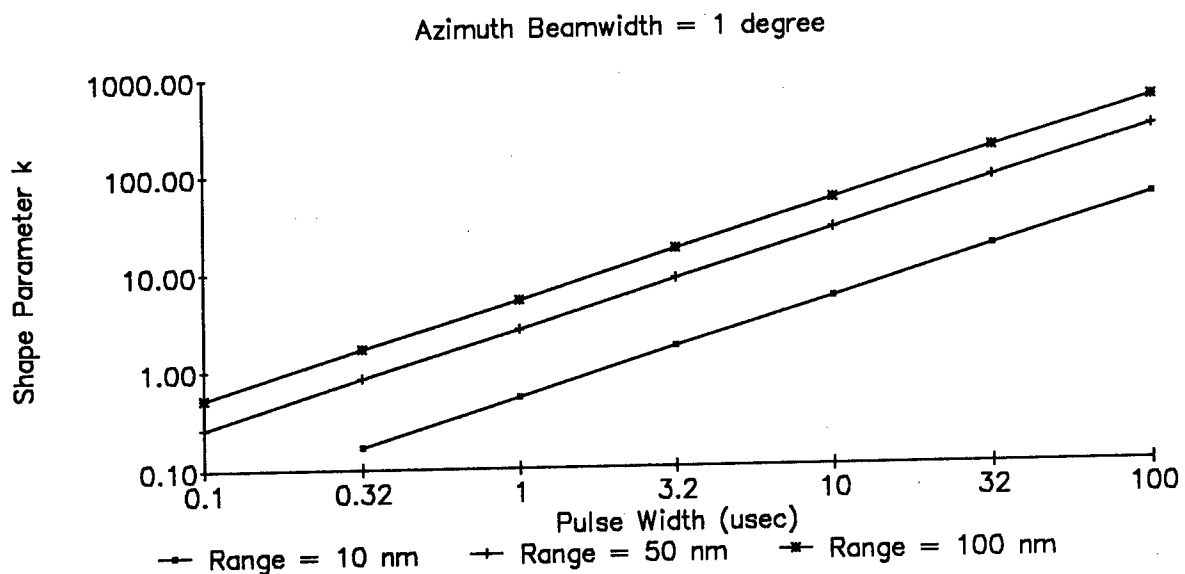


Figure 3.13 Shape parameter k versus pulse width for different ranges. Two-way azimuthal beamwidth is 1 degree.

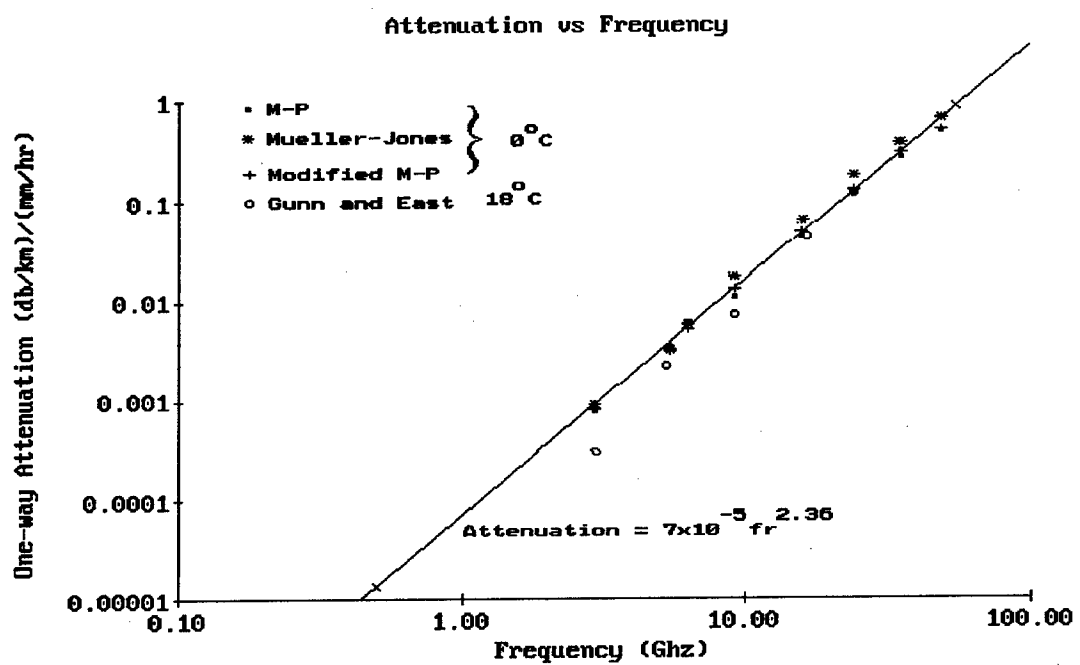


Figure 3.14 One-way rain attenuation K (dB/km/mm/hr) versus frequency.

The difference between the Gunn and East results and the others are attributed primarily to temperature. As shown in Figures 3.2 and 3.3, the temperature of the water mass above a few thousand feet is 0°C or below. As the rain falls from the melting level or is carried down from higher altitudes by convective downdrafts, its temperature will increase, but will typically remain between 0°C and 10°C. Therefore, a conservative model for attenuation would use the 0°C data.

Some of the studies mentioned above reported a weak nonlinear relationship between attenuation and rainrate for some wavelengths. However, the values proposed are not consistent for different wavelengths and the difference from a linear relationship is small. Figure 3.14 shows a linear fit to the 0°C data. The correlation coefficient of this fit is .95. Therefore, the proposed ADI model for one-way attenuation a is

$$a = .00013 f^{2.36} r_p R$$

where f is the carrier frequency in Ghz, R is the range in nm and r_p is the path averaged rainrate.

As discussed in Section 3.1.4, the percentage of path length containing a given rain intensity is equal to the percentage of area occupied by that rain intensity. Using the percentages for the mid-latitude, the path average rainrate is 2.275 mm/hr/nm. Since calculations for the sub-tropical region is similar, this value is suggested for the tropical regions as well.

3.2 Turbulent Layers and Index of Refractive Index Inhomogeneities.

During the past 50 years, echoes have also been observed from an atmosphere clear of precipitation. Some were correlated with birds and insects. Other echoes, however, have been related to inhomogeneities in the refractive index. As noted in several published studies which are summarized by Battan (1973), scatter can occur from turbulent horizontal layers and vertical convective currents.

Radar echoes structured in horizontal layers were found to correspond in height to regions of refractive-index inhomogeneities. When there is a considerable amount of turbulence in atmospheric regions having a high spatial

gradient of refractive index n , the irregular, small-scale fluctuations of n can cause appreciable backscatter.

Tatarski (1961) showed that the reflectivity in the backscattered direction is given by

$$\eta_v = \pi^2 k^4 F_n^*(k)$$

where k is the wave number ($= 4\pi/\lambda$) and $F_n^*(k)$ is the spatial power-spectral density. Hardy, Atlas and Glover (1966) obtained

$$F_n^*(k) = .033 C_n^2 k^{-11/3}$$

where C_n^2 is a measure of the mean-square fluctuations of the refractive index. Therefore,

$$\eta_v = 0.39 C_n^2 \lambda^{-1/3}$$

Measurements of C_n^2 have been performed by several investigators (Hardy and Katz (1969), Atlas et al (1966), Lane (1967)). These values typically range from 10^{-15} to 10^{-13} although values may be as high as $10^{-12} \text{ cm}^{-2/3}$. At $\lambda = 10 \text{ cm}$, these values provide volume reflectivities in dB of -137.4, -117.4 and

-107.4 dB m^2/m^3 . L-Band and UHF would be 1.3 dB and 2.8 dB less, respectively.

These layers travel at the wind velocity and can exist up to 10 km. The refractivity fluctuations are considered homogeneous and the magnitude of the instantaneous volume reflectivity will follow an exponential density function.

3.3 Lightning

Lightning is both a source of noise and a source of radar clutter. When the electromagnetic energy generated during a discharge has sufficient power at the radar frequency to be detected, such a signal is called a "sferic". Detections of microwave sferics by UHF, L-Band and S-Band radars were reported by Hewitt (1953), Ligda (1956) and Atlas (1958). As summarized by Battan (1973), the lightning signals were sometimes composed of several pulses (~ 10 avg.) of about 27.5 usec duration with approximately 20 usec spacing between

pulses. In a 1 khz bandwidth and at 10 km range, the signal amplitudes are about 60 μ v/meter at VHF and about 10 μ v/meter at S-Band.

The ionized channel created by the discharge can be a significant source of backscatter. Dawson (1972) calculated the radar cross sections for X-, S-, L- and VHF bands and concluded that radars operating at wavelengths of 10 cm or greater should received backscatter from a lightning channel for up to 100 msec after the initial discharge. He also found that the RCS should vary little between 10 and 150 cm. Gerlach and Mazur (1983) measured UHF lightning echoes at least 25dBZ higher than the 50 to 60 dBZ precipitation echoes in the storm. The RCS of the lightning channels ranged from -10 to +20 dBm² and the frequency of occurrence ranged from 2 to over 16 flashes/min per kilometer of range within the intense rain areas of the storm.

In summary, lightning is a significant source of backscatter and should be represented in the clutter model. The suggested ADI model is given in Table 3.4.

Table 3.4 Lightning Model

Number of flashes/min/nm: 20

Backscatter:

Average RCS per flash : 10 dBsm, UHF thru S-Band

Duration of echo : 100 msec exponential time constant

Mean radial doppler : 0 m/s

Sferic:

Amplitude at 10 km
within a bandwidth
of 1 kHz : 10 microvolts/m at S-Band
20 microvolts/m at L-Band
40 microvolts/m at UHF

of pulses/flash : 1 to 20

Duration /pulse : 20 to 35 microseconds

Spacing bwt pulses : 10 to 30 microseconds

4.0 SEA CLUTTER

The characterization of sea clutter is complicated by its dependence on a number of parameters, including grazing angle, polarization, radar frequency, radar resolution cell size and the condition of the sea surface. In order to describe the backscatter properties of the sea surface, Goldstein (1946) introduced a dimensionless quantity σ_0 , the RCS per unit area sometimes called surface reflectivity. Since Goldberg's paper, many measurements and theoretical studies have been published on the relationships between σ_0 and these parameters. Good summaries on the results of these studies can be found in several texts (Long (1975), Nathanson (1969), Skolnik (1962) and Skolnik (to name but a few). The sea clutter model proposed in this section is based on these studies.

4.1 Structure of the Sea Surface

The sea surface can be represented as a random function of position x (space) and time t , $f(x,t)$ where $f(x,t)$ is often approximated by a Gaussian surface (Kinsman 1965). The random heights of the surface in deep water is caused primarily by waves created by the wind. Parameters describing the sea, at least in a statistical sense, include wave height h , slope s , period T , length L_d and velocity. In deep water (depth $d \geq L_d/2$), the height (slope) and other characteristics of the waves depend on the duration of the generating winds and the distance or fetch over which these winds blow. Kinsman (1965) notes that the processes describing random seas may or may not be stationary and, if stationary, may not be ergodic. Table 4.1 presents the spatial and temporal properties of the processes used to model different sea conditions.

<u>Sea Condition</u>	<u>Process</u> <u>Time Variable</u>	<u>Process</u> <u>Space Variable</u>
Fetch-limited	stationary	inhomogenous
Duration-limited	nonstationary	homogeneous
Fully aroused	stationary	homogeneous
Swell	stationary	homogeneous

Table 4.1 Properties of processes for various sea conditions

Duration-limited refers to waves created by winds of limited duration. When the wind begins to blow over a fetch, statistically similar waves are created throughout the fetch and the statistics of wave heights (or slope) will be uniform (homogeneous) with position in the fetch. However, if one observes the statistics at one point within the fetch, the moments of the wave height (slope) will increase with time, inferring a non-stationary process. As the wind continues to blow for a sufficient length of time, the temporal statistics observed at one position will become constant (stationary). However, the spatial statistics will display an increase in wave height (slope) with respect to the distance from the upwind shore, an inhomogeneous condition. This corresponds to the fetch-limited case. If the fetch is long enough, a distance will be reached where the spatial statistics will cease to increase. At this distance and beyond, the sea is a "fully aroused sea" where the spatial statistics are constant representing a homogeneous process. When the waves leave the area of generating winds, they retain their stationary and homogeneous character and are referred to as swell.

Data on required fetch and wind duration is given by many sources including Undersea Technology (Nathanson (1969)). For 10 knot winds, a fully aroused sea of sea state 2 will exist 50 nm downwind from shore after 5 hours duration. For 20 knot winds, a sea state 5 condition will be reached beyond 200 nm if the winds last for about 25 hours. Most of the time, strong winds do not exist over the required fetch for the required durations. Therefore, the most seas are either duration-limited or fetch-limited creating temporally nonstationary or spatially inhomogeneous conditions with backscatter amplitudes less than the "sea state" for a given wind speed.

The two extreme sea regions will be considered in this model, the deep water areas where fully aroused conditions will be assumed for sea states up to 5 and the shallow waters near the land-sea interfaces. For each sea region, the sea surface can be broken down into many components with different scales. In this model, only two components will be discussed: a large scale roughness, a small scale roughness and short term features. The large scale roughness represent swell and the larger undulations of waves being generated by current winds. Small scale roughness refers to capillary, short gravity waves and the "white caps" and breaking wave crests.

4.2 Deep Water Sea

As discussed in Section 4.1, the surface of the sea is a random function that can be nonstationary with respect to time and inhomogeneous with respect to space. Since the mean reflectivity $\underline{\sigma}_0$ is a function of the surface, it is also a random function of time and space. Conceptually, the mean value of $\underline{\sigma}_0$ can be related to the average number and size of elemental surface scatterers per unit area. Katzin (1957) described these elemental scatterers as small "facets" on the large scale wave pattern or swell. Wright (1968), visualized them as patches of water waves. However, these scatterers may exist, it is useful to visualize the scattering mechanism as a density of N_{eff} effective scatterers on the sea surface.

The instantaneous surface reflectivity σ_0 from a single radar resolution cell can be given as a compound density function (Trunk 1972, Valenzuela and Laing 1971, Jakeman and Pusey 1976, Lewinski 1979, 1983)

$$(1) \quad p(\sigma_0) = \int_0^{\infty} p(\sigma_0/\underline{\sigma}_0) p(\underline{\sigma}_0) d\underline{\sigma}_0$$

where $p(\underline{\sigma}_0)$ is the pdf of the mean reflectivity, $p(\sigma_0/\underline{\sigma}_0)$ is the instantaneous reflectivity given that the cell has a mean value and $p(\sigma_0)$ is the pdf of the instantaneous reflectivity over the range of σ_0 . This formulation is analogous to that given in the discussion of precipitation clutter in Section 3.0.

The suggested functional form for the pdf of $\underline{\sigma}_0$ at a given grazing angle is that proposed by Jakeman and Pusey (1976) and used in the ATR (Simkins, 1981) and the ARSR-4 (Simkins, 1984) models.

$$(2) \quad p(\underline{\sigma}_0) = [k^k \underline{\sigma}_0^{k-1} \exp(-k\underline{\sigma}_0/\underline{\sigma}_g)] / [\Gamma(k)(\underline{\sigma}_g)^k]$$

where

k = the effective number of scatterers in a resolution cell

$$\approx [(c r/2D) |\cos \theta_w| + (R \theta_a/D) |\sin \theta_w|] * \phi_g^b$$

b = .666 for vertical polarization and 2 for horizontal polarization

ϕ_g = grazing angle in degrees

$\underline{\sigma}_g$ = the expected value of reflectivity as a function of grazing angle

θ_a = -3 db two-way antenna beamwidth in azimuth (degrees)

θ_w = the azimuth angle between the wave direction and the antenna beam
 λ = wavelength (meters)
 $\Gamma(\)$ = gamma function
 τ = pulse width in microseconds
 ϕ_e = - 3 dB two-way antenna beamwidth in elevation
 R = range, feet
 c = .984 ft/nsec
 D = correlation length, distance between uncorrelated samples of σ_o ;
~.5 water wavelength, feet for HH; 3 feet for VV

$\underline{\sigma}_g$ can be considered the expected value of σ_o at grazing angle ϕ_g while $\underline{\sigma}_o$ is the mean value at a given instant. For practical ADI waveforms and antenna sizes, the illuminated sea surface will always have many effective scatterers. Therefore, $p(\sigma_o/\underline{\sigma}_o)$ follows an exponential density function. As described for precipitation clutter, $p(\sigma_o)$ is approximately equal to $p(\sigma_o/\underline{\sigma}_o)$ for large k because $p(\underline{\sigma}_o)$ has very narrow spread about $\underline{\sigma}_g$. For small k , $p(\underline{\sigma}_o)$ can have significant spread and $p(\sigma_o)$ will deviate significantly from $p(\sigma_o/\underline{\sigma}_o)$.

$\underline{\sigma}_g$ varies significantly with grazing angle. Long (1965) pointed out that the range of possible grazing angles can be divided into three reasonably distinct regions: near vertical incidence, a plateau region and near grazing incidence. (Figure 4.1) For the near vertical incidence angles, the variation of $\underline{\sigma}_g$ with angle can be reasonably approximated by a Gaussian shape. The return in the plateau region can be represented as a compound function of the density function of tilts due to the large wave structures and the density function of the angle of the smaller facets given a tilt. (Trunk 1972, Valenzuela and Laing 1971, Jakeman and Pusey 1976) Such relationships often give rise to Weibull, log-normal and K distribution functions. In this report, a log-normal representation will be used. At near grazing angles, the effective number of scatterers corresponding to the plateau region is reduced by shadowing and multipath. While the boundaries ϕ_o and ϕ_c are a function of wavelength, surface condition and polarization, each region has general characteristics useful for modeling.

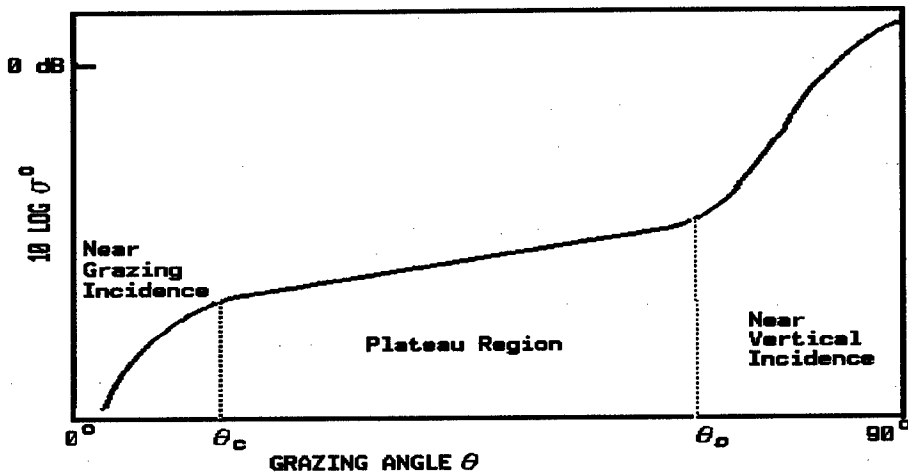


Figure 4.1 Dependence of reflectivity on grazing angle (Derived from Long et al 1965)

The proposed relationship between σ_g and grazing angle is

$$\sigma_g = A(\phi_g) * [B(\phi_i) + C(\phi_i)]$$

where $\phi_i = 90 - \phi_g$ (degrees). The propagation factor $A(\phi_g)$ is given by

$$A(\phi_g) = \varphi^b / (1 + \varphi^b)$$

where $\varphi = \phi_g h_{1/3} (.2 + .11/\lambda)$, $h_{1/3} = (w/17)^2$, w = wind speed for sea state in knots and $b = 2$. The plateau factor $B(\phi_i)$ is given by

$$B(\phi_i) = [5 s_b^{16} / \ln(s_b) .5] (\phi_i + s_b) (2\pi) .5 * \exp(-(\ln(\phi_i + s_b))^2 / 2(\ln(s_b))^2)$$

where $s_b = 10$ for VV; $(2 + s_c)$ for HH. The near incidence factor $C(\phi_i)$

$$C(\phi_i) = (100/s_c) (2\pi) .5 * \exp(-(\phi_i/2s_c)^2)$$

where $s_c = (13 + 1.3 w) .5$

Most of the sea data reviewed during this study were airborne measurements published by Daley and his collaborators at Naval Research Laboratory (NRL) reports. (Daley et al 1968, 1970, 1971, 1973) These results present the median values of the instantaneous reflectivity σ_0 , not σ_g . However, referring to equations (1) and (2), k is very large at high grazing angles and $p(\sigma_0)$ can be

approximated by an exponential pdf. This function has a mean-to-median ratio of 1.6 dB, approximately the ratio observed by the NRL researchers. Figures 4.2 thru 4.5 compares σ_g (dB) with data taken by Daley et al (1970) for sea states 2 and 6. Figures 4.6 and 4.7 compares σ_g (dB) for sea states 1 thru 6.

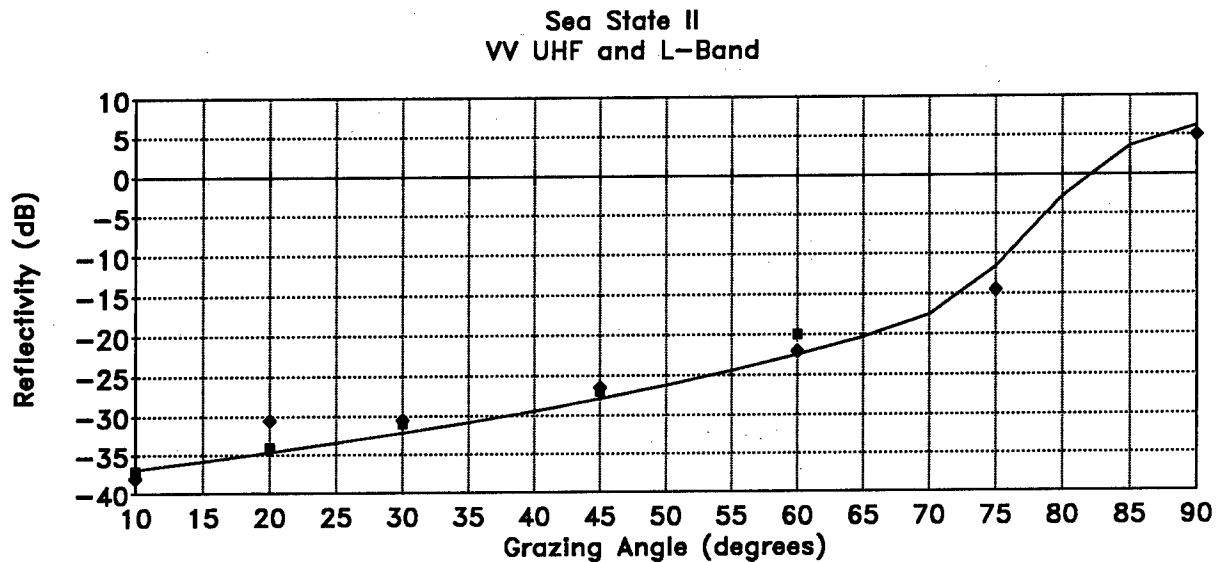


Figure 4.2 Reflectivity versus grazing angle for vertical polarization, sea state 2 (Data derived from Daley et al 1970)

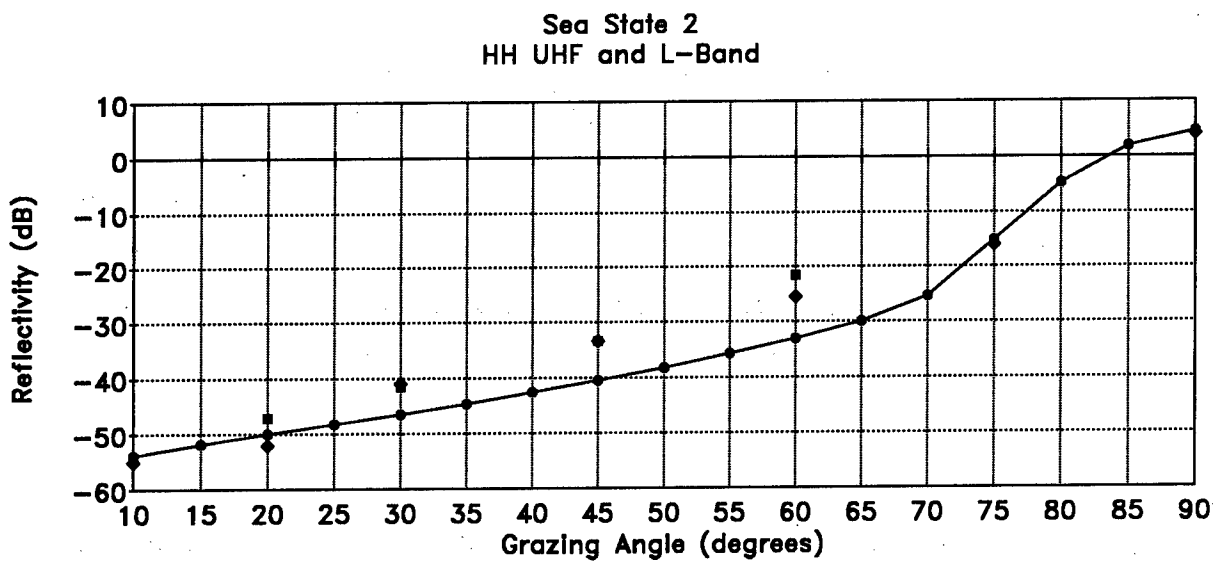


Figure 4.3 Reflectivity versus grazing angle for horizontal polarization, sea state 2 (Data derived from Daley et al 1970)

Sea State 6
VV UHF and L-Band

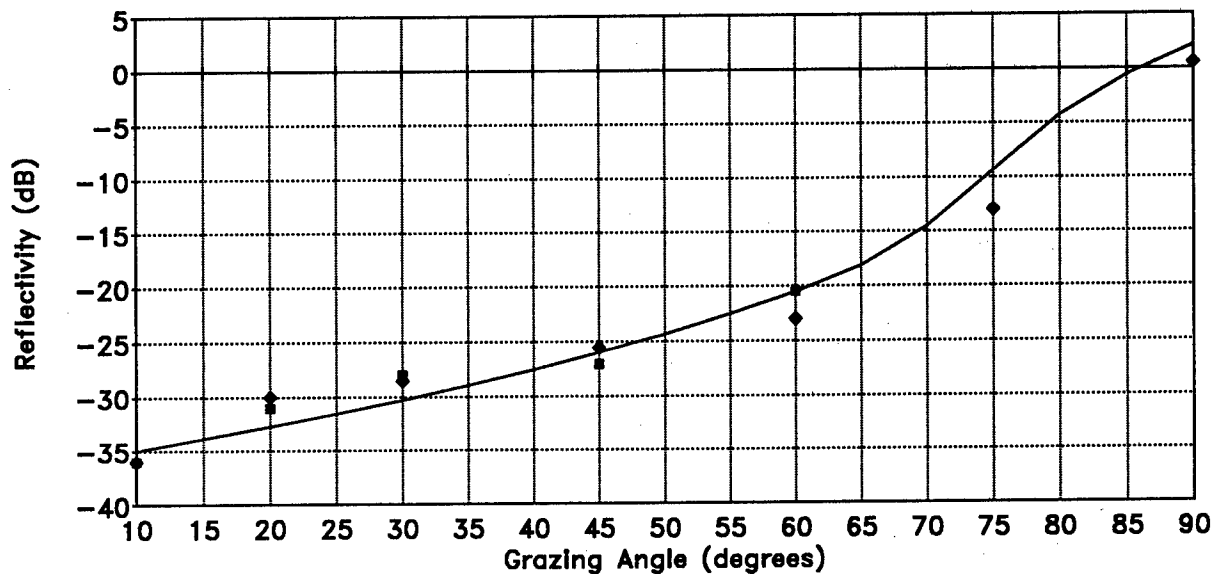


Figure 4.4 Reflectivity versus grazing angle for vertical polarization. sea state 6 (Data derived from Daley et al 1970)

Sea State 6
HH UHF, L-Band, S-Band

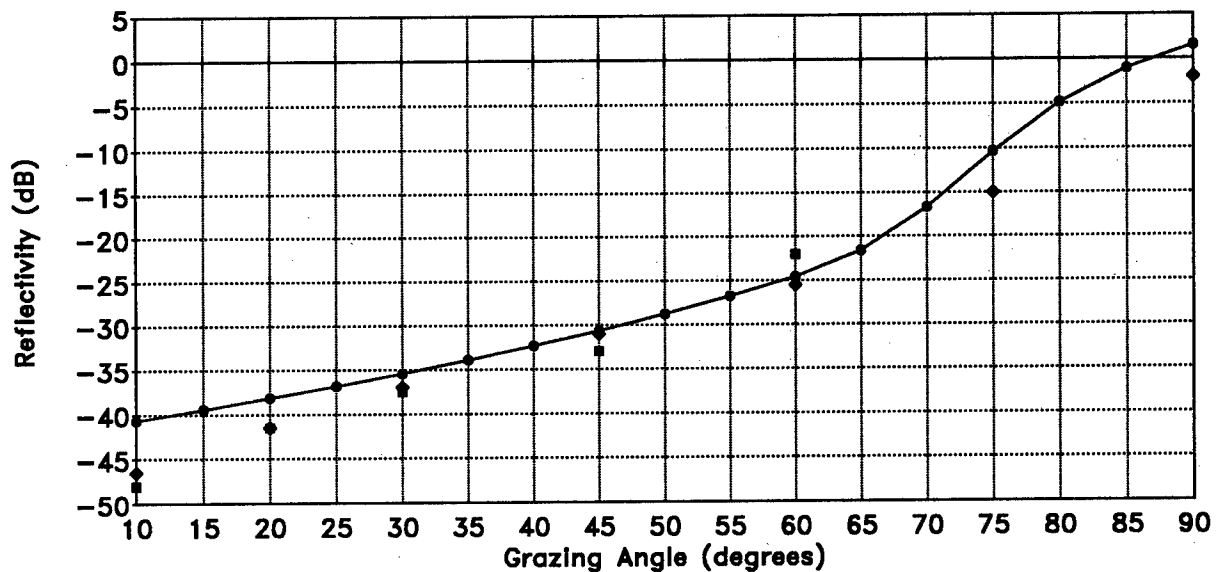


Figure 4.5 Reflectivity versus grazing angle for horizontal polarization. sea state 6 (Data derived from Daley et al 1970)

Sea State 1-6
VV UHF, L Band and S-Band

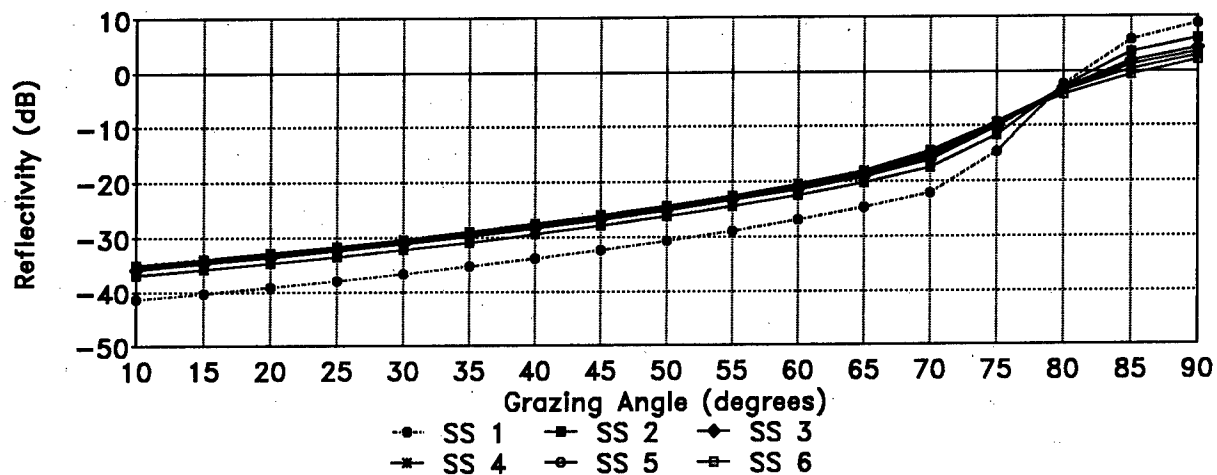


Figure 4.6 Reflectivity versus grazing angle for vertical polarization, sea state 1 - 6

Sea States 1 - 6
HH UHF, L Band and S Band

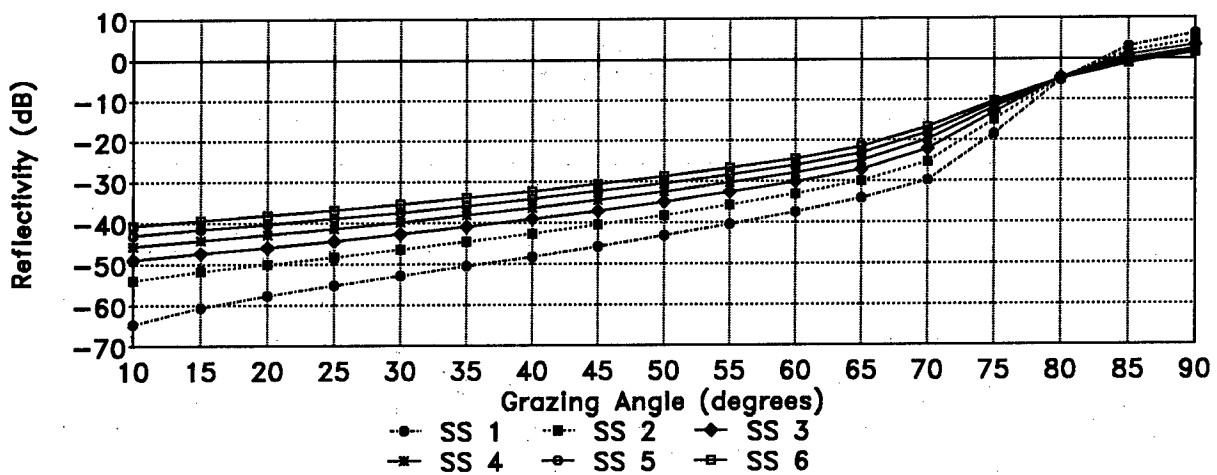


Figure 4.7 Reflectivity versus grazing angle for horizontal polarization, sea state 1 - 6

For lower grazing angles, the effective number of scatterers are reduced due to shadowing and destructive multipath interference. Daley (1970) noted that the median σ_0 for HH and VV is reduced by ϕ_g^4 at UHF thru S-Band,

especially for the lower 4 sea states. This result can be approximated by assuming that the mean value and k , which are both functions of the effective number of scatterers (Jakeman and Pusey 1976), are a function of ϕ_g^2 .

On the other hand, Ward (1982) has reported k to be proportional to $\phi_g^{.66}$ for vertical polarization at X-Band. If this relationship is applied to the mean value as well, the spread and mean of σ_o will change less with grazing angle, with a narrower spread and higher mean value than that for ϕ_g^2 at near grazing angles. Until more data or theory is available, the ϕ_g^2 relationship is suggested for both vertical and horizontal polarization. Figures 4.8 thru 4.17 present the mean and median of σ_o versus grazing angle and sea state for UHF, L Band and S-Band.

Since the pdf of σ_o is a gamma function, the pdf of σ_o about the mean is a K distribution (Jakeman and Pusey 1976) and is given by

$$p(\sigma_o) = \int_0^{\infty} p(\sigma_o/\sigma_o) p_k(\sigma_o) d\sigma_o$$

$$= [2k\{(k+1)/2\} (\sigma_o/\sigma_o)\{(k-1)/2\}/\Gamma(k)] K_{k-1}\{2(k\sigma_o/\sigma_o).5\}$$

The corresponding cumulative distribution functions for the gamma and K distributions are displayed in Figures 4.18 and 4.19, respectively, for several values of k . Figure 4.20 shows how k varies with radar bandwidth and

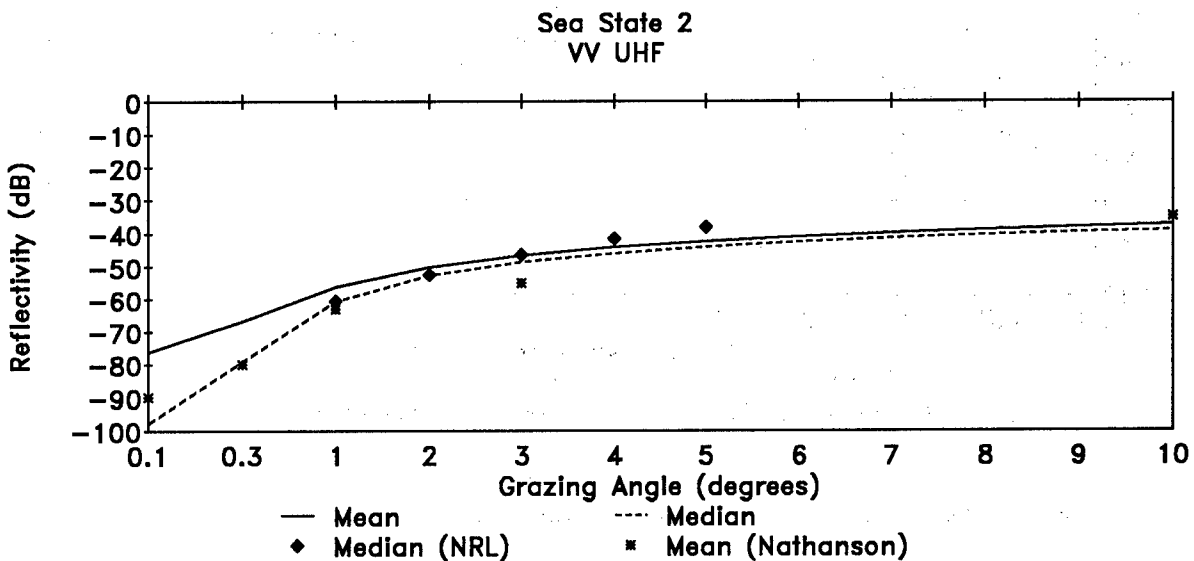


Figure 4.12 Reflectivity versus grazing angle for sea state 2, UHF VV

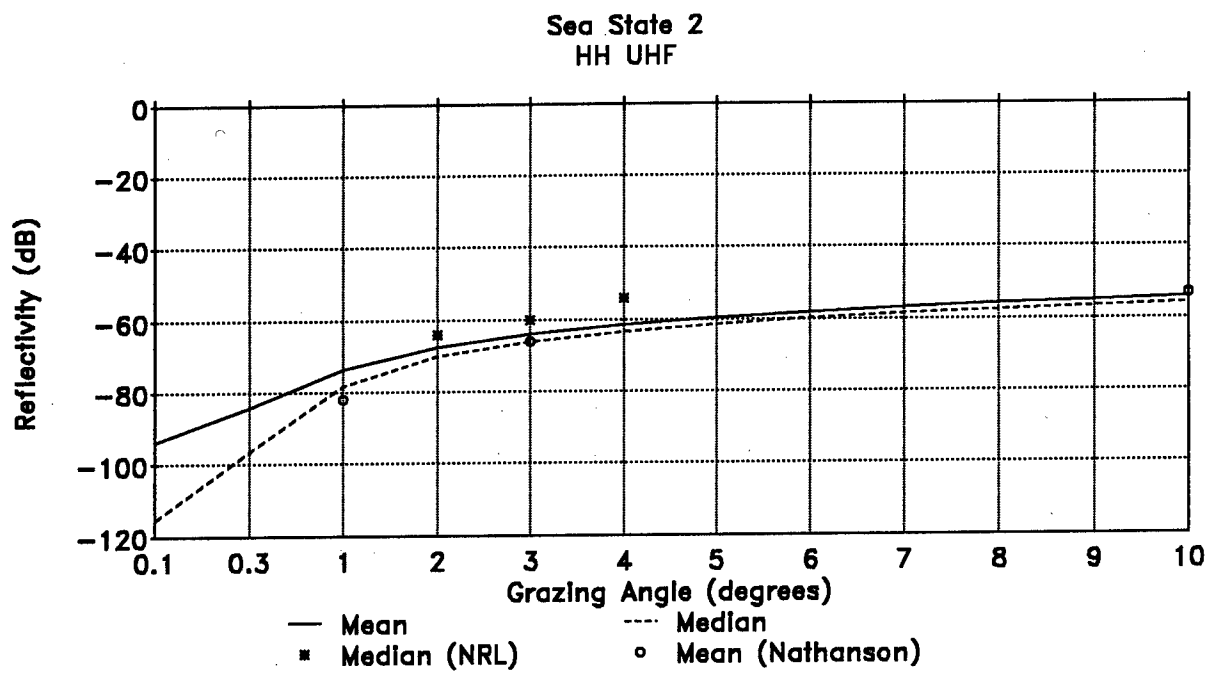


Figure 4.13 Reflectivity versus grazing angle for sea state 2, UHF HH

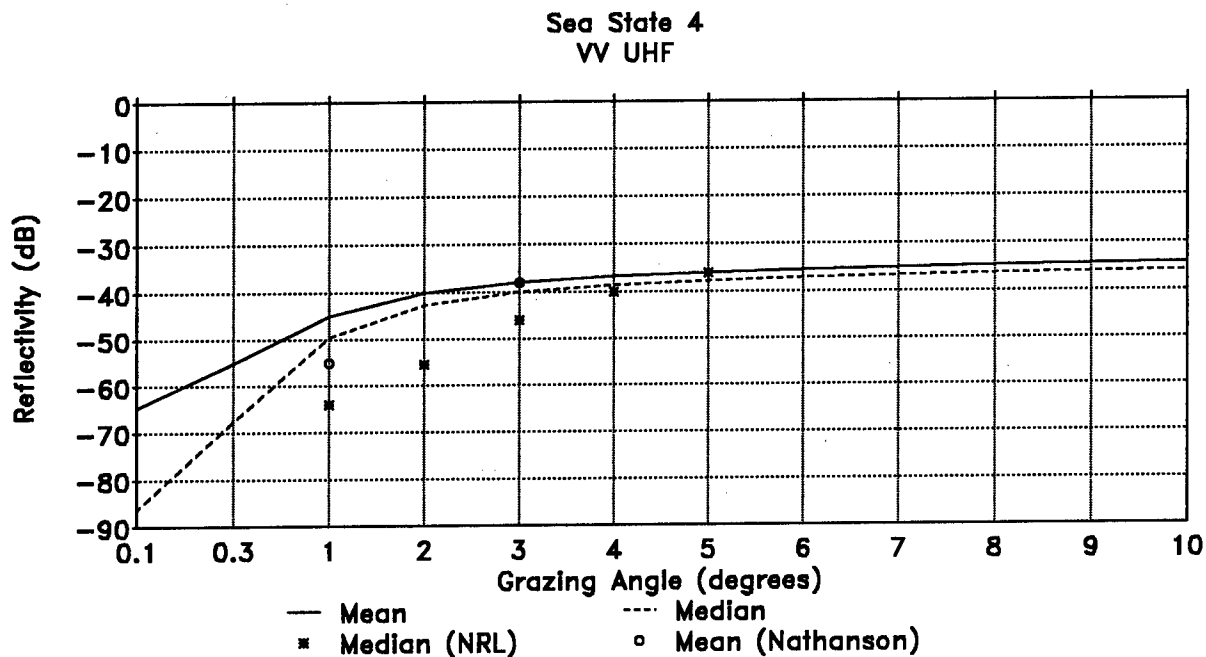


Figure 4.14 Reflectivity versus grazing angle for sea state 4, UHF VV

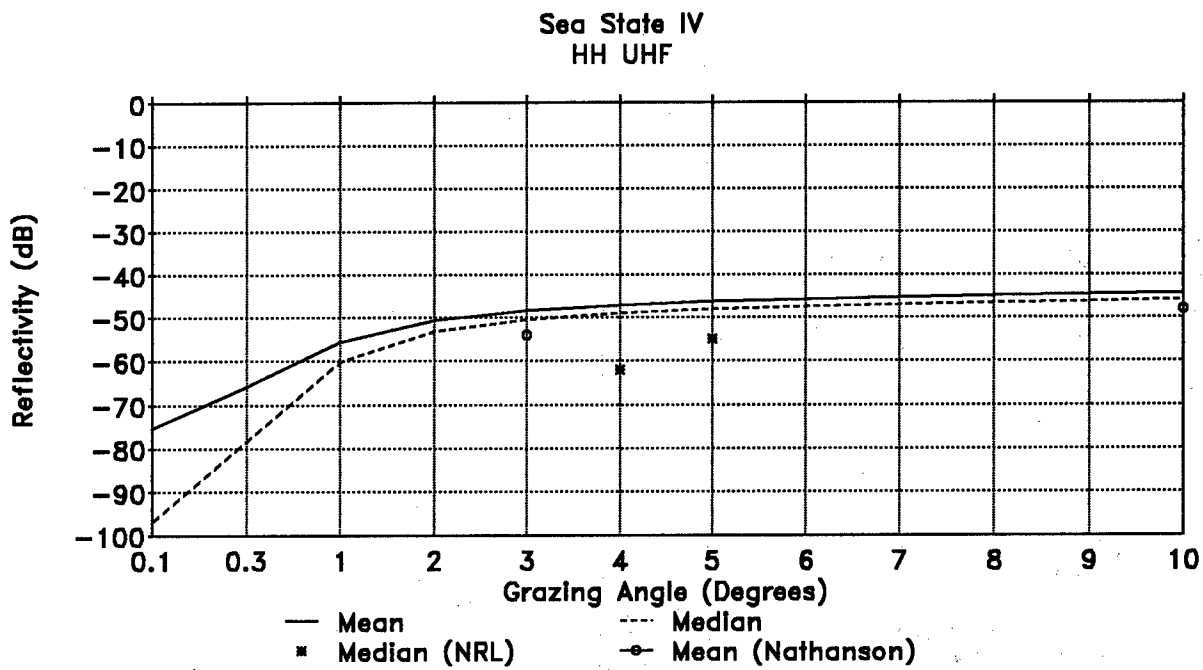


Figure 4.15 Reflectivity versus grazing angle for sea state 4, UHF HH

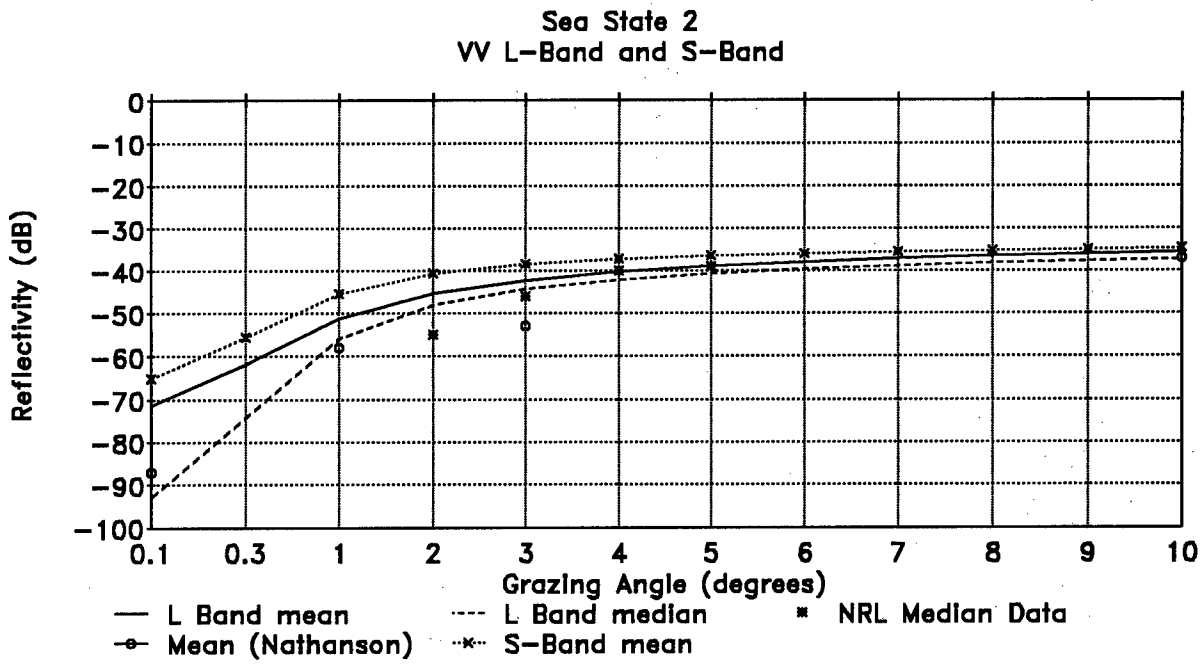


Figure 4.16 Reflectivity versus grazing angle for sea state 2, L and S Band VV

Sea State 2
HH L Band and S Band

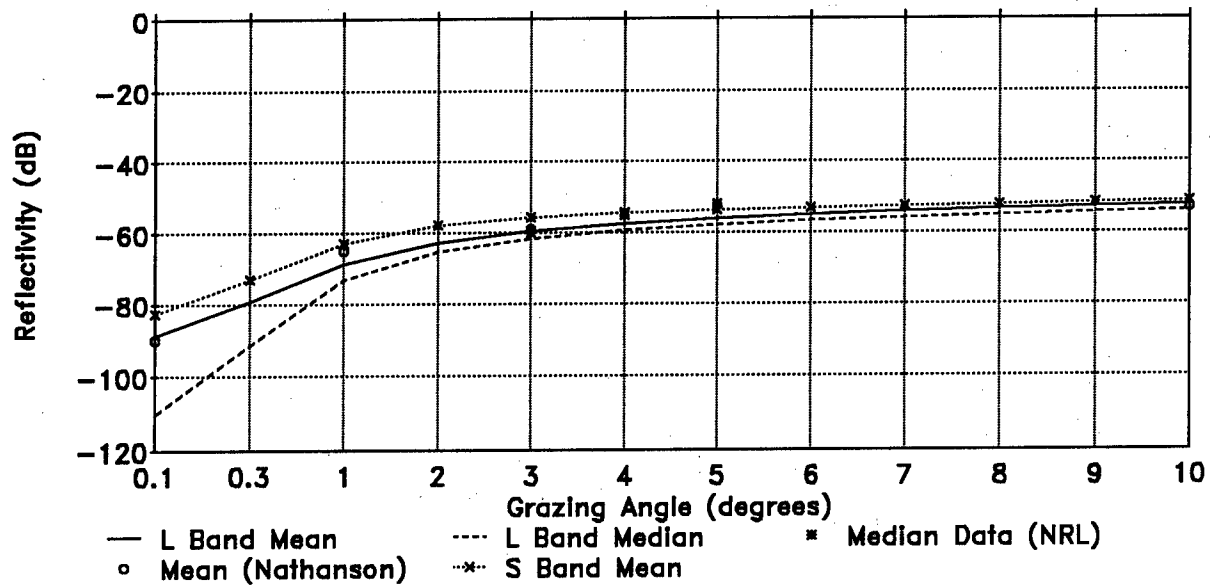


Figure 4.17 Reflectivity versus grazing angle for sea state 2, L and S band, HH

Sea State 4
HH L Band and S Band

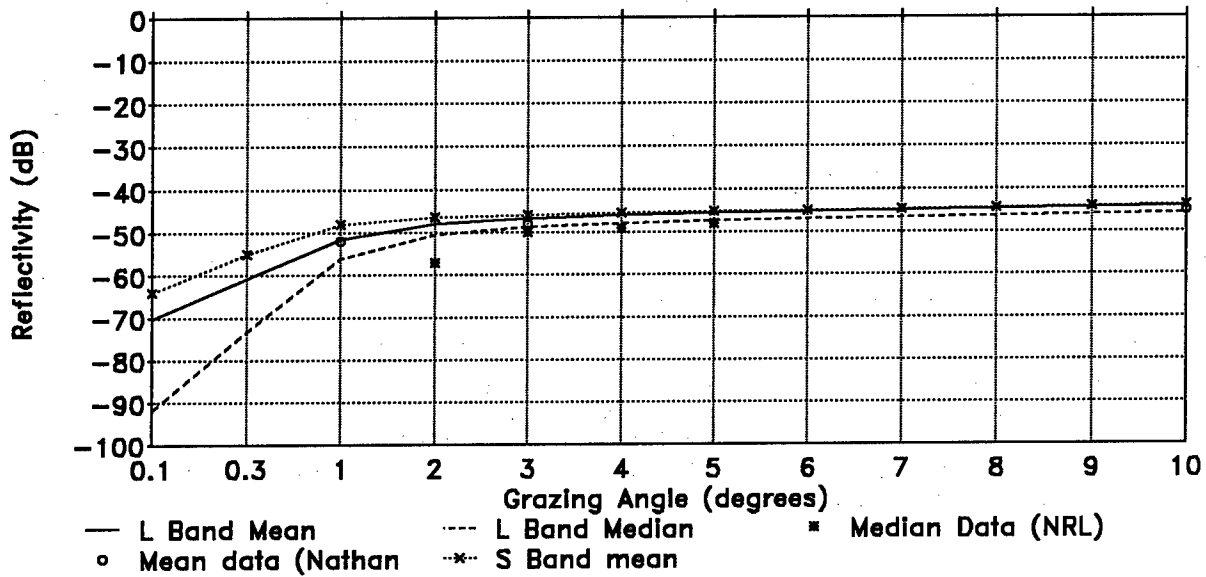


Figure 4.18 Reflectivity versus grazing angle for sea state 4, L and S Band
VV

Sea State IV
VV L Band and S Band

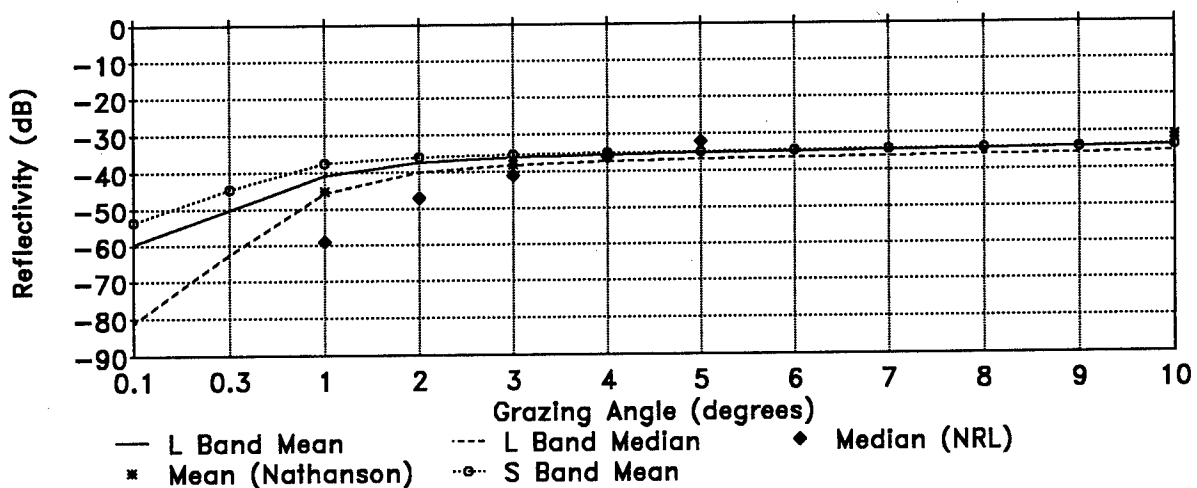


Figure 4.19 Reflectivity versus grazing angle for sea state 4, L and S Band HH

sea state for a grazing angle of 1 degree and a range of 115 nm. As explained for precipitation clutter, the temporal statistics of reflectivity for a single cell are similar to the local spatial statistics about the cell. For an airborne radar, the observed statistics versus range will vary because the grazing angle varies with range. However, at long range, the grazing angle will change little with small variations in range and the observed spatial and temporal statistics will also be similar. Figure 4.21 presents how the standard deviation-to-mean ratio of σ_o varies with resolution cell size.

For observations of a single cell, the temporal covariance function of σ_o is given by

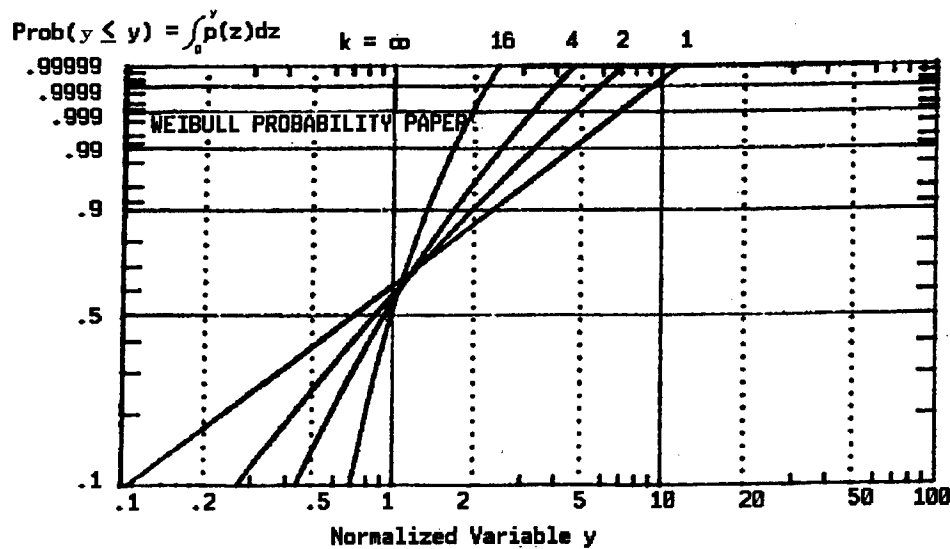
$$R(\tau) = aR_1(\tau) + bR_2(\tau).$$

where $a = 1/k$, $b = 1-a$ and k is the shape parameter given above.

$$R_1(\tau) = [\sin(\pi\tau/(.707)t_w)/\pi(\tau/(.707)t_w)]^2$$

and

$$R_2(\tau) = \exp(-\tau^2/2\sigma_\tau^2)$$



NORMALIZED GAMMA DISTRIBUTION

Figure 4.18 Normalized gamma distribution

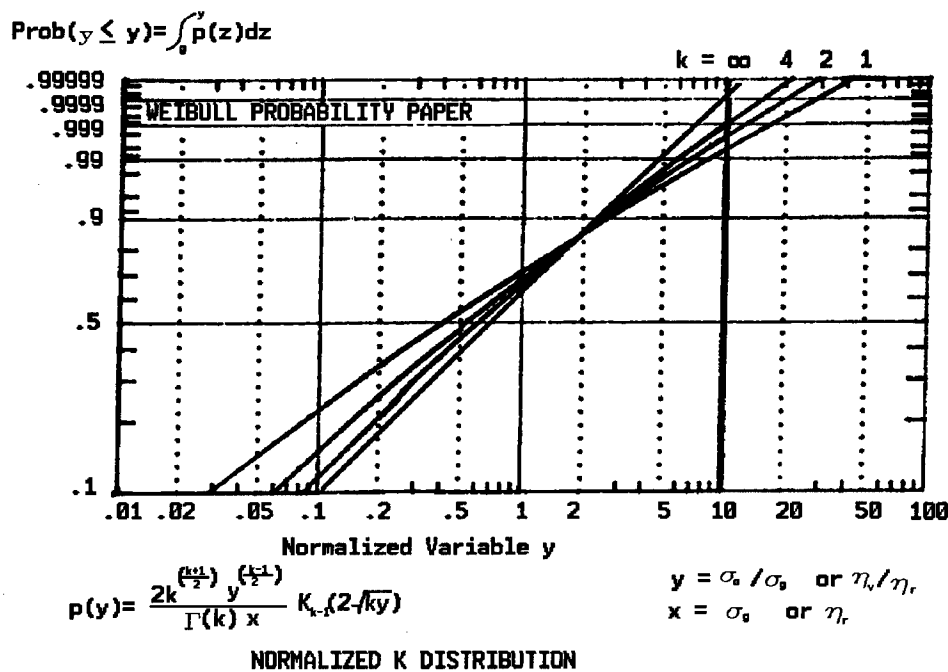


Figure 4.19 Normalized K distribution

Figure 4.20 K versus
Radar Pulse Width

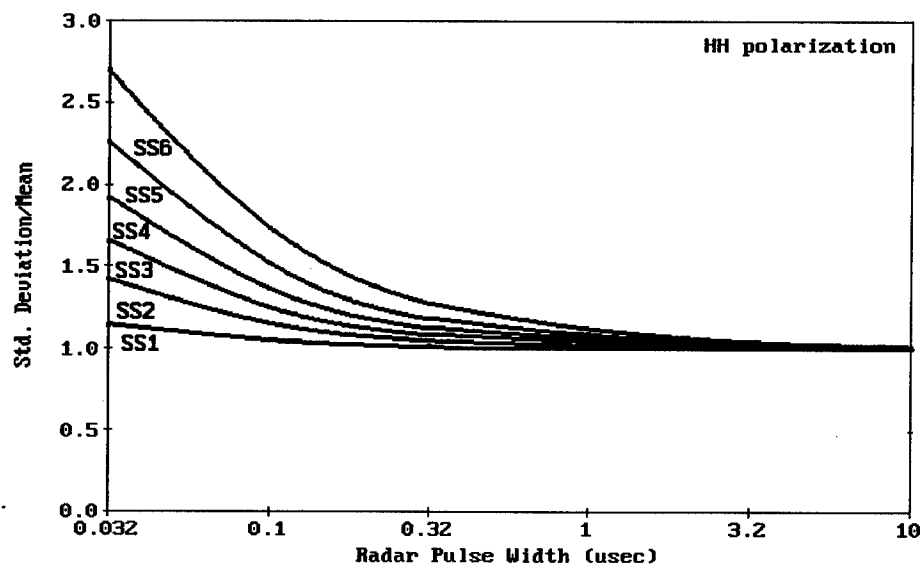
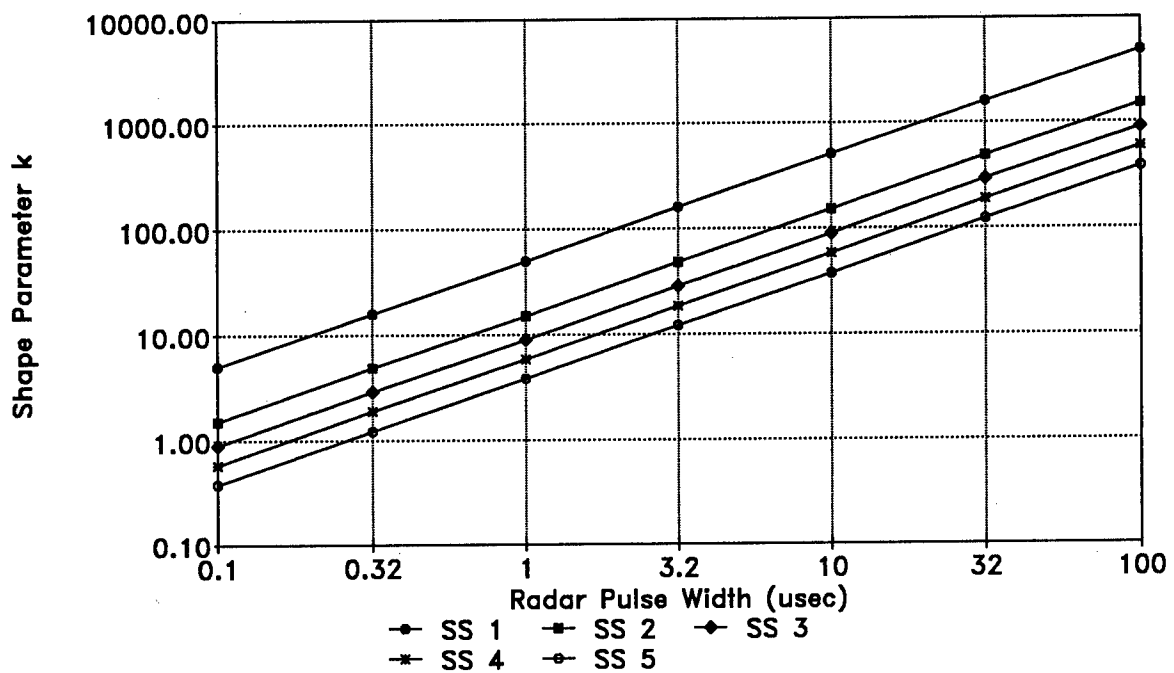


Figure 4.21 Standard deviation-to-mean ratio versus resolution cell size
(upwind/downwind)

where t_w is the water period of the given sea state, $\sigma_r = 1/(2\pi\sigma_f)$ and σ_f is the standard deviation of the doppler spectrum. The water period and other parameters relevant to a given sea state is given in Table 4.2. $R(r)$ is presented in Figure 4.22 and is similar in form to that observed by Long (1974).

The velocity density function for sea is Gaussian with a radial mean velocity μ_v and standard deviation σ_v given by

$$\mu_v = 1.15 w \cos \theta_w \text{ (knots) HH}$$

$$\mu_v = .13 w \cos \theta_w \text{ (knots) VV}$$

$$\sigma_v = .1 w \text{ (knots) HH, VV}$$

where w is the wind speed in knots. The corresponding doppler components μ_f and σ_f can be obtained by

$$\mu_f = 1.03 \mu_v/\lambda$$

and

$$\sigma_f = 1.03 \sigma_v/\lambda.$$

	Water Wavelength			Water Period (sec)	Wind Speed (knots)		
	λ_w (feet)						
	λ_w^{\min}	λ_w^{nom}	λ_w^{\max}				
Sea State 1	--	10	20	1	5		
Sea State 2	20	40	70	2.8	9		
Sea State 3	70	90	110	4	13		
Sea State 4	110	140	190	5	17		
Sea State 5	190	230	260	6.3	21		

Table 4.2 Values of Water Wavelength λ_w , Wave Period t_w and Wind Speed w as a function of Sea State and Polarization (Open Sea)

Figure 4.22 (a) $R(t)$ versus t
 SS 4 HH $k = 2.23$

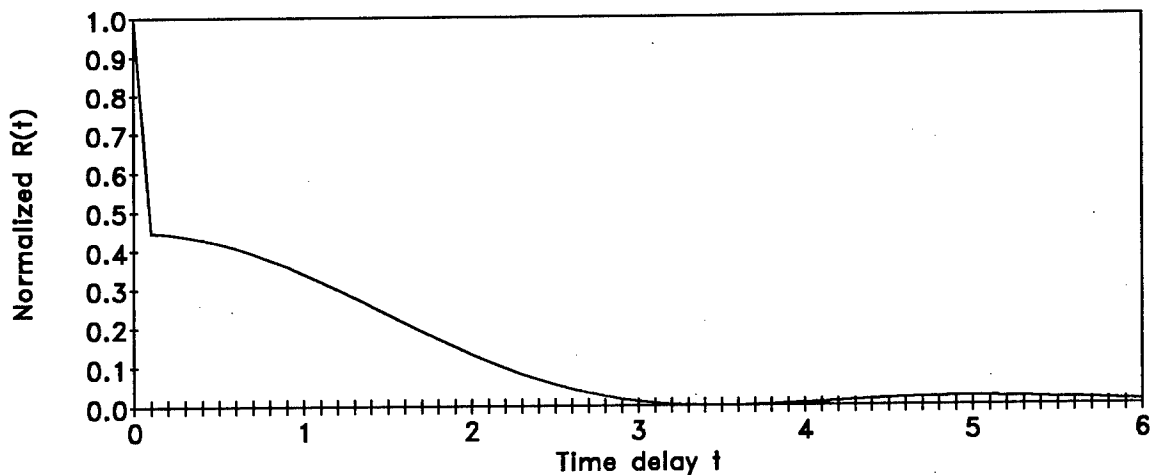
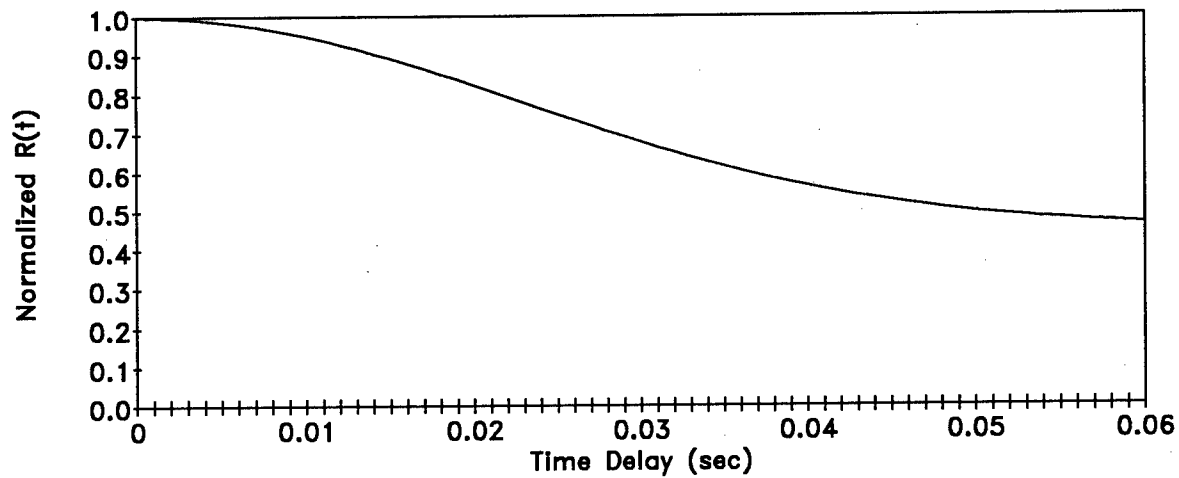


Figure 4.22 (b)
 Time Expansion about $t=0$



4.3 Land-Sea Interface

Bascom (1964) and Kinsman (1965) describe how the nature of water waves change as it approaches shallow water. In deep water, the water mass moves in an orbital motion as a wave passed through it. The water mass has very little translational motion. As the waves approach the shore, the period of the waves remain the same, but the phase velocity of the waves decrease. This creates a "bunching" effect where the water wavelength decreases from that given for the

open sea. The waves become higher and steeper as a larger part of the wave energy is placed above the water line and the energy is represented by the kinetic energy as the mass of water in the wave approaches the wave velocity. When the wave breaks, plunging breakers often entrap air, which is then compressed as the upper part of the wave collapses. The air often escapes explosively, sending spray up to 50 ft. The entire process can take place in only a few seconds. At the same time, a transitional wave is created where water is pushed forward at the wave velocity.

If the wave continues into deeper water, the water mass will again resume an orbital motion with reduced energy. If, on the other hand, the water continues into progressively shallower water, the water mass in the transitional wave will continue to move at the wave velocity determined by the depth. These waves travel above the existing water line and later waves can overtake earlier ones because the latter waves increase the effective depth and therefore the wave velocity.

Several of the differences between shallow and deep water waves given above could account for the "land-sea interface" effect often observed. Both the increased wave height and the increased density due to "bunching" can increase the mean reflectivity above that observed in the adjacent deeper water. Since the water mass in the transitional wave travels at the wave velocity, its mean doppler is much higher than that observed in the deeper water. Finally, the foam and spray is more dense in the shallower water creating more spread in the observed velocities.

No radar measurements of these phenomena were found during this study and it is suggested that measurements be obtained if performance at the land-sea interface is important. In the absence of data, the trends described above are presented by the following simple models for the land-sea interface. The mean amplitude from sea within 1000 feet of land is twice the value for the sea state in the adjacent deeper water. The power of the return is evenly split between two velocity components. The first component has the same mean and standard deviation as that for deeper water. The second component will have a mean velocity = $(gd)^{.5}$ where g is 9.8 meters/sec² and d is the wave height associated with the sea state in deeper water. The spectral spread is the same as that given for deeper water.

5.0 TERRAIN CLUTTER

Terrain clutter is more difficult to model than weather or sea clutter for several reasons. First, terrain has both volume scatterers and surface scatterers. Second, there are a wide variety of "terrain types" and vegetation, each of which can provide significant variations in backscatter seasonally or even diurnally. Third, many terrain regions contain an increasing number of manmade scatterers or manmade modifications to the terrain and vegetation which dominate the scatter statistics. Fourth, the characterization of clutter from a "terrain type" is complicated by its dependence on grazing angle, polarization, radar frequency, wind and moisture conditions, radar resolution cell size and even aspect. Finally, the roughness of the terrain prevents accurate knowledge of the power density on the surface and vegetation, especially at low grazing angles.

Nevertheless, the study of terrain clutter has been of primary interest for the last 50 years because it is the strongest and most extensive clutter problem for microwave radars. Following Goldstein (1946), the backscatter from terrain is described by its RCS per unit area or surface reflectivity σ_0 . Many measurements and theoretical studies have been published on the relationships between σ_0 and the radar-related and geometric parameters mentioned above. Highlights have been summarized in radar texts such as Nathanson (1969) and Skolnik (1970) while more extensive information has been compiled by Long (1973), Barton (1975) and the many reports recently published by MIT Lincoln Laboratory (MITLL). The terrain clutter models proposed in this section are based on a review of this literature and of earlier airborne models such as the IITRI clutter models described by Greenstein et al (1969), Carlson and Greenstein (1969) and Kazel et al (1971).

5.1 Terrain Types and Vegetation

The terrain types required for the preliminary evaluation of an ADI system are mountains, rural, urban, and farmland. However, "rural" and "urban" are vague definitions of "terrain". Because manmade scatterers have different characteristics than terrain scatterers, they have received special attention in Section 6.0. In this section, mountains, forest and farmland will be addressed. "Urban terrain" can then be constructed by the superposition of a

high density of manmade structures on a low relief terrain such as farmland. Likewise, "rural" terrain can be the superposition of a low density of manmade structures in forest, farmland or mountains.

The terrain consists of four basic components, the natural ground surface consisting of sand, loam, rocks, etc., the small bodies of water from puddles and ditches to streams and rivers, manmade structures and vegetation such as grass, crops, brush and trees. The natural ground surface provides a stable echo whose amplitude is related primarily to its roughness and permittivity and the local grazing angle of incident radiation. Since the roughness of the terrain generally changes with space (i.e., range and cross range), the mean amplitude from the terrain will also change with space. At low grazing angles, the roughness can create significant shadowing which further complicates the characterization of amplitude from the terrain surface.

The amplitude of the backscatter from the small bodies of fresh water can often be neglected. However, the rivers and streams that are large enough to displace terrain and vegetation through erosion can create boundaries where near vertical terrain surfaces or tree lines can provide higher backscatter than the surrounding areas. Furthermore, since streams tend to be oriented in one general direction, i.e., downhill, the backscatter tends to be aspect dependent. Similarly, the backscatter from roads and paths can be ignored while the anisotropic backscatter from the tree lines and manmade gouges in the terrain created by these roads cannot.

Vegetation provides a large echo whose fluctuation characteristics depend on the vegetation type, the season and the local wind turbulence. While vegetation in the open plains can be relatively homogeneous for significant distances, those along the coasts are usually not. This is especially so along the Atlantic coast where the farmland is usually divided into small areas by hedge rows and tree lines and few forests extend long distances without natural or manmade partitions.

Therefore, in general, the scatter from the terrain surface and vegetation is spatially inhomogeneous. Furthermore, within each of the broad terrain types needed for ADI, sufficient variability exists such that there is no single set of amplitude distributions or correlation functions that describes each type. Since an ADI radar system would be expected to meet minimum performance in almost all terrain environments, this section will present models representing the upper bound of reviewed measurements. If and when

performance can somehow be taylored for less stringent conditions on a geographical basis, the recent work by Billingsley, deRidder and their collaborators (1981, 1986, 1987) may be more appropriate. They have achieved some consistency in the measured statistics of terrain backscatter by segregating measurements from "analogous" terrain, i.e. terrain with similar roughness, vegetation and cultural features and a review of their more recent results is recommended.

5.2 Spatial Distribution of Mean and Instantaneous Surface Reflectivity

The instantaneous surface reflectivity σ_0 from a single radar resolution cell can be given as a compound density function (Trunk 1972, Valenzuela and Laing 1971, Jakeman and Pusey 1976, Lewinski 1979, 1983)

$$(1) \quad p(\sigma_0) = \int_0^{\infty} p(\sigma_0/\underline{\sigma}_0) p(\underline{\sigma}_0) d\underline{\sigma}_0$$

where $p(\underline{\sigma}_0)$ is the pdf of the mean reflectivity $\underline{\sigma}_0$, $p(\sigma_0/\underline{\sigma}_0)$ is the instantaneous reflectivity σ_0 given that the cell has a mean value of $\underline{\sigma}_0$ and $p(\sigma_0)$ is the pdf of the instantaneous reflectivity over the range of $\underline{\sigma}_0$. Therefore, $p(\sigma_0/\underline{\sigma}_0)$ is an exponential distribution. The functional form for the pdf of $\underline{\sigma}_0$ at a given grazing angle ϕ_g is the gamma distribution described earlier for sea clutter

$$(2) \quad p(\underline{\sigma}_0) = [k^k \underline{\sigma}_0^{k-1} \exp(-k\underline{\sigma}_0/\underline{\sigma}_g)] / \{\Gamma(k)(\underline{\sigma}_g)^k\}$$

where

k = the effective number of scatterers in a resolution cell

$$\sim (Rh_a/D_a) (c\tau/2D_r) \phi_g^2$$

$\underline{\sigma}_g$ = the nominal expected value as a function of grazing angle and terrain type

$\Gamma()$ = gamma function

ϕ_g = grazing angle in degrees

D = the distance between uncorrelated samples of the gamma distributed mean in azimuth (a) and range (r).

h_a = two-way azimuthal beamwidth in radians

$\underline{\sigma}_g$ can be considered the expected σ_0 value at grazing angle ϕ_g over larger spatial areas of a terrain type while σ_0 is the mean value at a given instant. For practical ADI waveforms and antenna sizes, the illuminated terrain surface will always have many effective scatterers. Therefore, $p(\sigma_0/\underline{\sigma}_g)$ follows an exponential density function and the functional form for $p(\sigma_0)$ is the K distribution. Jao (1983) has shown that the K-distribution provides a reasonable fit to airborne radar data. As described for precipitation clutter, $p(\sigma_0)$ is approximately equal to $p(\sigma_0/\underline{\sigma}_g)$ for large k because $\underline{\sigma}_g$ has very narrow spread about σ_g . For small k , $p(\sigma_0)$ can have significant spread and $p(\sigma_0)$ will exhibit highly skewed, Weibull-like distributions.

An analysis of SAR data by IITRI (Kazel et al 1971) revealed autocovariance functions generally of the shape given in Figure 5.1. The narrow peak had a width comparable to the size of the averaged resolution cell for all terrain types and is due partially to sampling and partially to true variations of σ_0 . The broader, low spatial frequency component determines the correlation length D . For mountains, measured values of D were typically a few hundred feet and a value of 500 feet was recommended by the IITRI model. For farm terrain, the autocovariance function falls to 0 between 1000 feet and about 6000 feet depending on the size of the farm fields. The IITRI model recommended D equal to 1000 feet for farmland and 500-1000 feet for woodland.

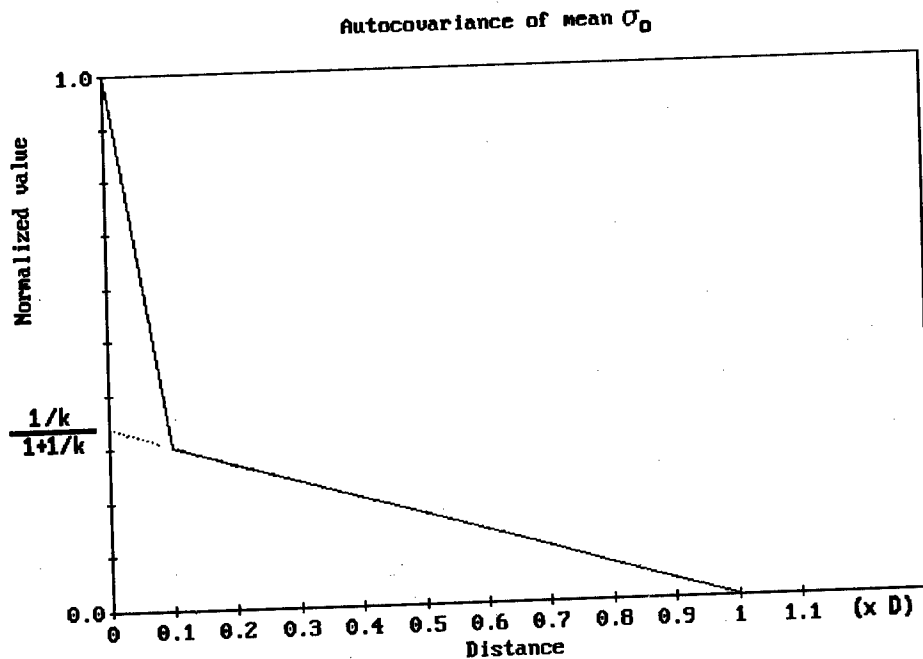


Figure 5.1 Autocovariance Function of Mean Reflectivity

The observed correlation lengths in range and cross-range can be obtained by convolving the matched filter length in each dimension with the function given in Figure 5.1. For the ARSR-4 system, the matched filter range and azimuth resolutions were comparable or exceeded D. Therefore, a simple shape for the covariance function was proposed. For ADI waveforms with bandwidths less than 1 or 2 mHz and short coherent integration times, the correlation length will be approximately D for most terrains. As the system resolution increases, the effective correlation length will approach the width of the narrow peak.

For expected ADI search waveforms, k has a value $\gg 1$. This leads to a narrow density function for $p(\sigma_0)$ about σ_g and the observed instantaneous density function $p(\sigma_0)$ is exponential. The use of a high resolution waveform such as SAR for some special purpose such as target classification may lead to non-exponential distributions at angles up to 20 degrees.

The σ_g varies significantly with grazing angle. As with sea clutter, the range of possible grazing angles can be divided into three reasonably distinct regions: near vertical incidence, a plateau region and near grazing incidence. (refer to Figure 4.1) Correspondingly, the value of σ_g is related to grazing angle by

$$\sigma_g = B(\phi_g) + C(\phi_g)$$

where $B(\phi_g)$ is the plateau factor and $C(\phi_g)$ is the near incidence factor.

The most important region for an airborne system is the plateau region with grazing angles ranging from 10 to 60 degree. The return in the plateau region is often reasonably approximated by a constant gamma model $B(\phi_g) = \gamma \sin(\phi_g)$. Figures 5.2 and 5.3 present data measured by Daley et al (1968) compared with the constant gamma model. As observed by Daley, several of the terrain types seem to fit well to a constant gamma model. However, the recommended choice of γ for the three terrain types varies significantly. Figure 5.4 presents several measurements and models for farmland and forest, respectively. The recommended values of γ range from .2 (-7 dB) to .01 (-20 dB). Similarly, the values of γ for mountains range from .4 (-4 dB) for the AN/APS-125 radar procurement to approximately -13 dB for the NRL data provided by Daley et al (1968). The recommended values for the ADI model are .2 (-7 dB) for mountains, .1 (-10 dB) for forest and .032 (-15 dB) for farmland. In this region, there is still very little shadowing and the value for k as given

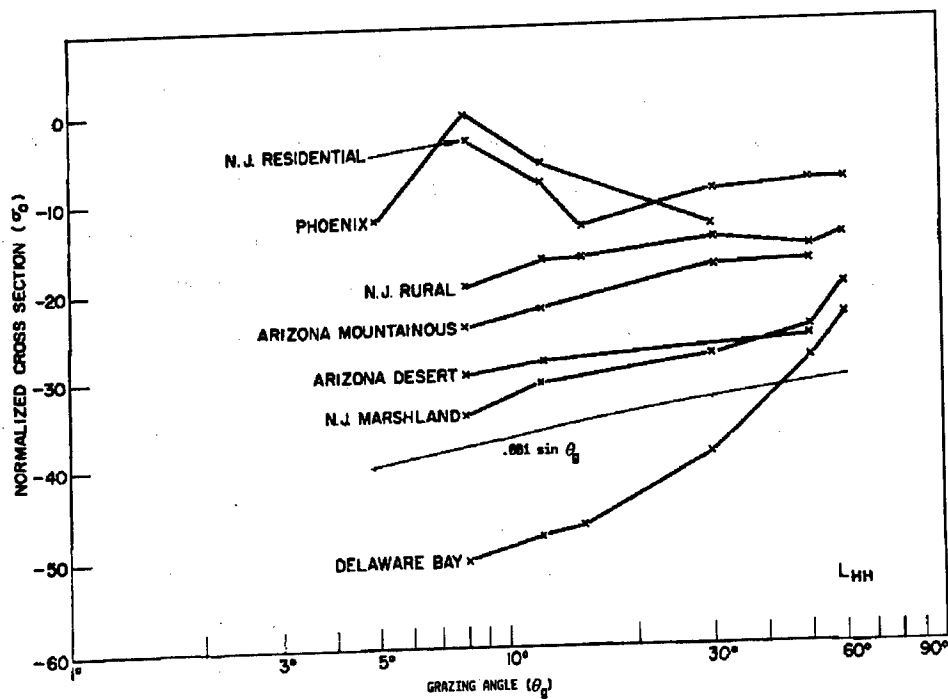


Figure 5.2 Variation of Median Reflectivity with Grazing Angle (Derived from Daley et al 1968)

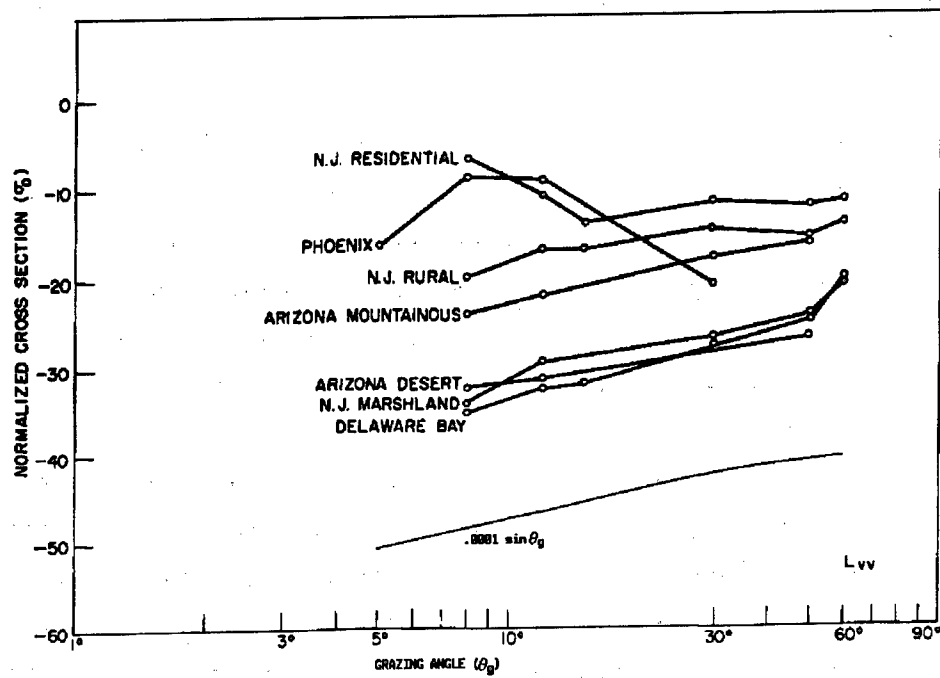


Figure 5.3 Variation of Median Reflectivity with Grazing Angle (Derived from Daley et al 1968)

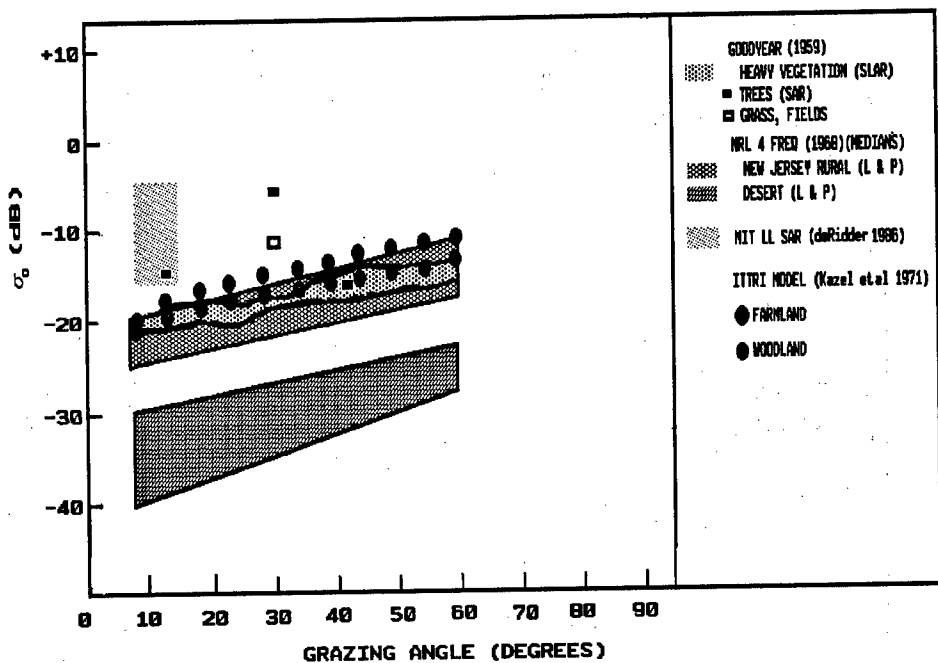


Figure 5.4 Summary of Airborne Measurements and Models

by (2) will be equal to or greater than 10 for typical ADI search waveforms.

Clutter from near vertical incidence (grazing angles greater than 60 degrees) is important only for ambiguous waveforms. Figure 5.5 displays near vertical measurements of σ_g made at UHF and S-Band by the Sandia Corporation (Janzen et al 1959) as presented by Moore (1969) and Long (1973). The smoother terrain provides a higher backscatter than rougher terrain and the S-Band reflectivity is generally higher than the UHF data. The variation of σ_g with angle can be reasonably approximated by a Gaussian shape and the near-incidence factor $C(\phi_g)$ can be given by

$$C(\phi_g) = 10 \log((C1/\lambda) (1/s_c(2\pi)^{.5}) * \exp\{-(\pi 90 - \phi_g)^2/2s_c^2\})$$

where $s_c = 10$, scale factor $C1$ is 50 for farmland and woodland and 10 for mountainous regions and λ is the wavelength in meters. Figure 5.6 presents the recommended models of σ_g for grazing angles between 10 and 90 degrees.

In this region, there is essentially no shadowing and, for typical ADI waveforms, k assumes large values much greater than 10. As for the plateau region, this leads to a narrow density function for $p(\sigma_0)$ about σ_g and the observed instantaneous density function $p(\sigma_0)$ is exponential.

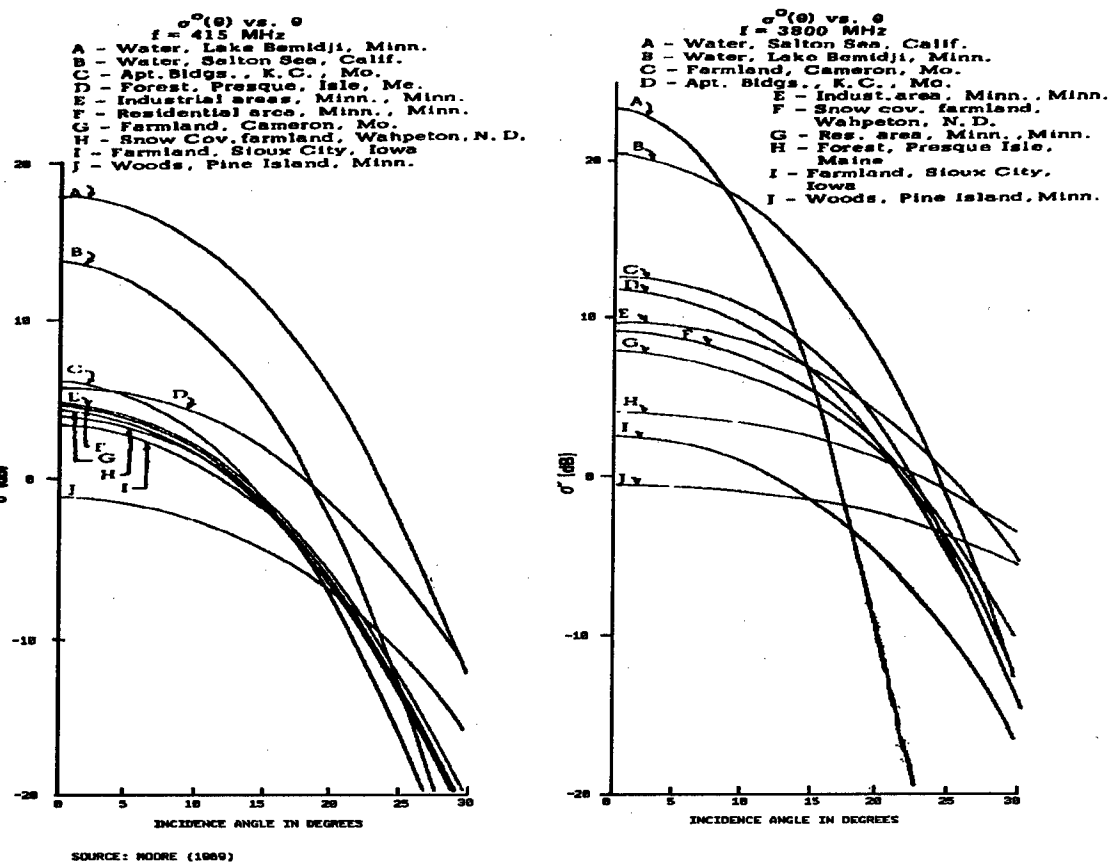


Figure 5.5 Reflectivity measurements near vertical incidence at UHF and S-Band (Janza et al 1959)

Proposed ADI Model for Terrain
L-Band, Grazing angles > 10 degrees

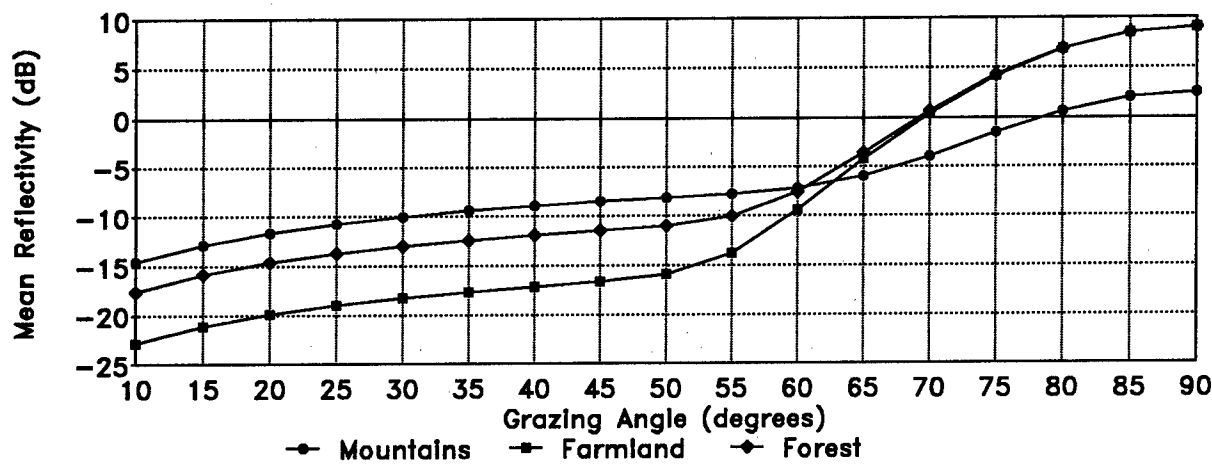


Figure 5.6 Proposed ADI models for grazing angles > 10 degrees at L-Band

At near grazing angles, the effective number of scatterers corresponding to the plateau region is reduced by shadowing and multipath. For forest and farmland, only "microshadowing" is assumed and the constant gamma model for σ_g in the plateau region is extended to 0 degrees. Since the manmade vehicles and buildings are modeled separately, most of the forest and farmland clutter is considered to be distributed with only a few "discrete" echoes from hedge rows, tree lines and other natural scatterers.

In the ATR model (1981) and the ARSR-4 model (1985), the functional form for the pdf of σ_o was the Weibull distribution

$$(2) \quad p(\sigma_o) = (\ln 2)(c\sigma_o^{(c-1)}/\sigma_m^c) \exp[(-\ln 2)(\sigma_o/\sigma_m)^c]$$

where σ_m is the median reflectivity and c is the shape parameter. The values for wooded hills and mountains were derived from Weibull fits to data published by Simkins et al (1977) as used in the SEEK IGLOO radar procurement. Since σ_m and c, in general, vary with resolution cell size, values were given for the minimum expected resolution cell size for the ADI and ARSR-4 systems, about 50,000 square feet or $\sim 4650 \text{ m}^2$. By giving a correlation distance, the appropriate values of c and σ_m for larger cells could then be derived for larger cells by determining the corresponding reduced standard deviation-to-mean ratio of σ_o . For wooded lowlands, σ_m and c were given as functions of the grazing angle.

$$\sigma_m = .1 \sin^2 (\phi_g)$$

$$4.22/10 \log(\sigma_{84} - \sigma_m) = 4.22/10 \log[(.078/\phi_g^{1.4}) + 1.1]$$

$$c = \begin{cases} & \text{for } \phi_g \geq .052 \text{ radians} \\ .2 & \text{for } \phi_g < .0052 \end{cases}$$

A correlation length of 3000 feet was provided to allow the calculation of σ_m and c for larger resolution cell sizes. These formulas were derived to approximate three characteristics observed in low angle measurements published by Linell (1963), Long (1973), Nathanson (1969), Daley et al (1968), Maffett et al (1978) and Simkins (1977). First, the median value decreases approximately as ϕ_g^n where n is between 2 and 3. Second, the standard deviation-to-mean ratio increases approximately as ϕ_g^{-n} where, again, n is

between 2 and 3. Finally, Linell (1963) observed that the mean value decreased gradually from 5 to about 2 degrees and then increased again. Similar trends have been observed in extensive measurements recently performed by MITLL and published by Billingsley (1987) and deRidder (1986).

While these trends are reflected by the above formulae, they are awkward to use. For ADI, a gamma distributed mean given by Equation (2) is recommended, resulting in a K-distribution for the observed instantaneous density function $p(\sigma_0)$. The simple formula for k given with equation (2) presents the effects of grazing angle similar to the ARSR-4 model and inherently includes effects of increasing resolution cell size. While this model is a generalization of forest and farmland clutter, it is adequate for preliminary system design and evaluation. When a more sophisticated model of farmland and forest is required including cultural features and terrain roughness, a review of the work published by Billingsley (1987), deRidder (1986) and Jao (1983) is recommended.

The above expression is adequate for low relief terrain where micro-shadowing predominates. However, for mountains, a statistical model must include the effect of large scale shadowing which provides areas of strong echoes surrounded by areas where noise dominates. Such "macro-shadowing" presents a patchy display on a PPI where the mean reflectivity within the patches tends to be independent of range, but the frequency of occurrence and size of the patches decreases with range. For grazing angles below 10 degrees, a patch model similar to the ARSR-4 model is suggested where P_1 , the probability that a resolution cell will contain a patch of clutter exceeding noise, is given by

$$P_1 = \exp[-\ln(2) (R/100)^2]$$

where R is the range to the resolution cell in nm. The value of 100 nm was chosen for the Pacific coast where 14,000 foot mountains will be observed by an ADI craft operating off the coast. By this formula, 50% of the resolution cells illuminating mountains at 100 nm would contain clutter while mountains at 200 and 260 nm would present clutter in only 6.25% and .9% of the cells, respectively.

The roughness of mountains is such that grazing angle no longer has any useful meaning and a more useful parameter is depression angle. Therefore, for mountains, it is suggested that k be defined by

$$k \sim (R\theta_a/D_a) (cr/2D_r) (\phi_d - \phi_h)^2$$

where ϕ_d is the depression angle and ϕ_h is the depression angle at the horizon.

5.3 Temporal fluctuation from Terrain and Vegetation

Terrain scatterers can be either randomly moving, stationary or combination of the two. Since most scatterers except for the ground itself move to some extent, it is useful to separate the scatterers into two classes. The first class are moving scatterers that move such that (1) the phase of each scatterer varies randomly over $+\/- 180$ degrees and (2) the amplitude and phase received from each scatterer is independent of the amplitude and phase from other scatterers in the cell. Wind blown leaves and branches often meet this criterion. The second class includes the rocks, tree trunks and other scatterers moving less than $.25\lambda$. For the purposes of this model, these scatterers are considered stationary. The relative population of stationary and moving scatterers within a cell depends on the wind speed and carrier wavelength and is described by the DC-to-AC power ratio m^2 .

The range of temporal fluctuation from terrain can be described by a Rician density function

$$p(\sigma_o(t)/\underline{\sigma}_o) = (m^2+1) \exp[-\sigma_o(m^2+1)/\underline{\sigma}_o] \exp[m^2] I_0[2m((m^2+1)(\sigma_o/\underline{\sigma}_o))^{.5}]/\underline{\sigma}_o$$

where m^2 is the DC-to-AC ratio, $\underline{\sigma}_o$ is the mean reflectivity value of the cell and $I_0[]$ is the modified Bessel function of the first kind of zero order. S-Band measurements published in Kerr (1951) revealed m^2 to be 30 for rocky terrain with sparse vegetation and 5.2 for heavily wooded terrain in 10 mph winds. For the wooded terrain, m^2 drops to ~ 1 at about 22 knots and ~ 0 for winds over 30 knots. L-band measurements at 5 Alaskan sites published by Simkins et al (1977) revealed similar values and recent low grazing measurements reported by Billingsley and Larrabee (1987) showed m^2 ranging

from approximately 1 to near zero for 17 knots winds. None of the data sets measured the same or similar wooded terrain at the same geometries or wind conditions and it is impossible to determine why the differences exist. Since the impact of the different measurements on radar design is small, it is recommended that the ARSR-4 models be used until further data can be obtained.

Several measurements of the correlation and spectral properties of terrain clutter have been made during the last 40 years with a wide range of results. The two factors characterizing the AC component is the spectral shape and -3dB width.

Long (1973) summarizes some of the spectral shapes proposed for the AC component by different authors as of 1973 including Gaussian (Barlow 1949), f^{-3} (Fishbein et al 1967), and bimodal shapes such as Gaussian and f^{-2} (Ivey et al 1956). More recent measurements have not yet settled this issue. Simkins et al (1977) performed measurements at several Alaskan sites comparing the spectra of resolution cells causing false alarms with adjacent cells of similar amplitude which did not cause false alarms. The cells causing false alarms tended to have a spectral shape approximated by f^{-3} to f^{-4} at frequencies several Hertz from the carrier while the clutter cells of similar intensity not causing false alarms tended to have a narrower f^{-5} or exponential shape.

Measurements of similar spectral shapes have been reported by Kapitanov et al (1973), Armand et al (1975), Andrianov et al (1976), and Andrianov et al (1976). Kapitanov (1973) placed a small lamp on one of the tree branches and recorded the motion of the branches on film. Analysis of the spectrum of the branch motion revealed two segments. Below 0.8 Hz, the spectrum was described well by $f^{-5/3}$ while above 0.8 Hz, the spectra of the moving branch was well approximated by f^{-4} , the same spectral shape observed by the X-band radar. Using wider dynamic range equipment, Armand et al (1975) demonstrated that this shape exists down to -100 dB Hz^{-1} and up to 2500 Hz at X-Band (~80 knots). Andrianov et al (1976) published measurements showing the spectral shape within 20 dB of the 1 Hz amplitude is well approximated by an exponential while the higher frequency tails followed f^{-n} where $n = 5.6, 3.8$ and 3.4 for birch, alder and pine respectively.

In contrast, recent measurements published by Billingsley and Larrabee (1987) fitted well to an exponential shape over a 60 dB dynamic range and the

f^{-n} tails were not observed. While it is not obvious why f^{-n} tails should be observed by some investigators and not others, possible explanations include the type of vegetation, season and geometry. Since the limitation to MTI performance is determined by the tails, the models proposed for the ARSR-4 effort had an f^{-n} shape. The same models are proposed for the ADI effort for the same reasons.

Figure 5.7 presents measurements of -3dB widths for mixed forest published by Kapitanov (1973) and for alder, pine and birch published by Andrianov et al (1976). The values chosen for the ARSR-4 model are also indicated. This figure shows that the -3 dB width increases linearly with wind speed. This model is also proposed for ADI with the customer choosing the wind speeds appropriate for the worst case operating environment.

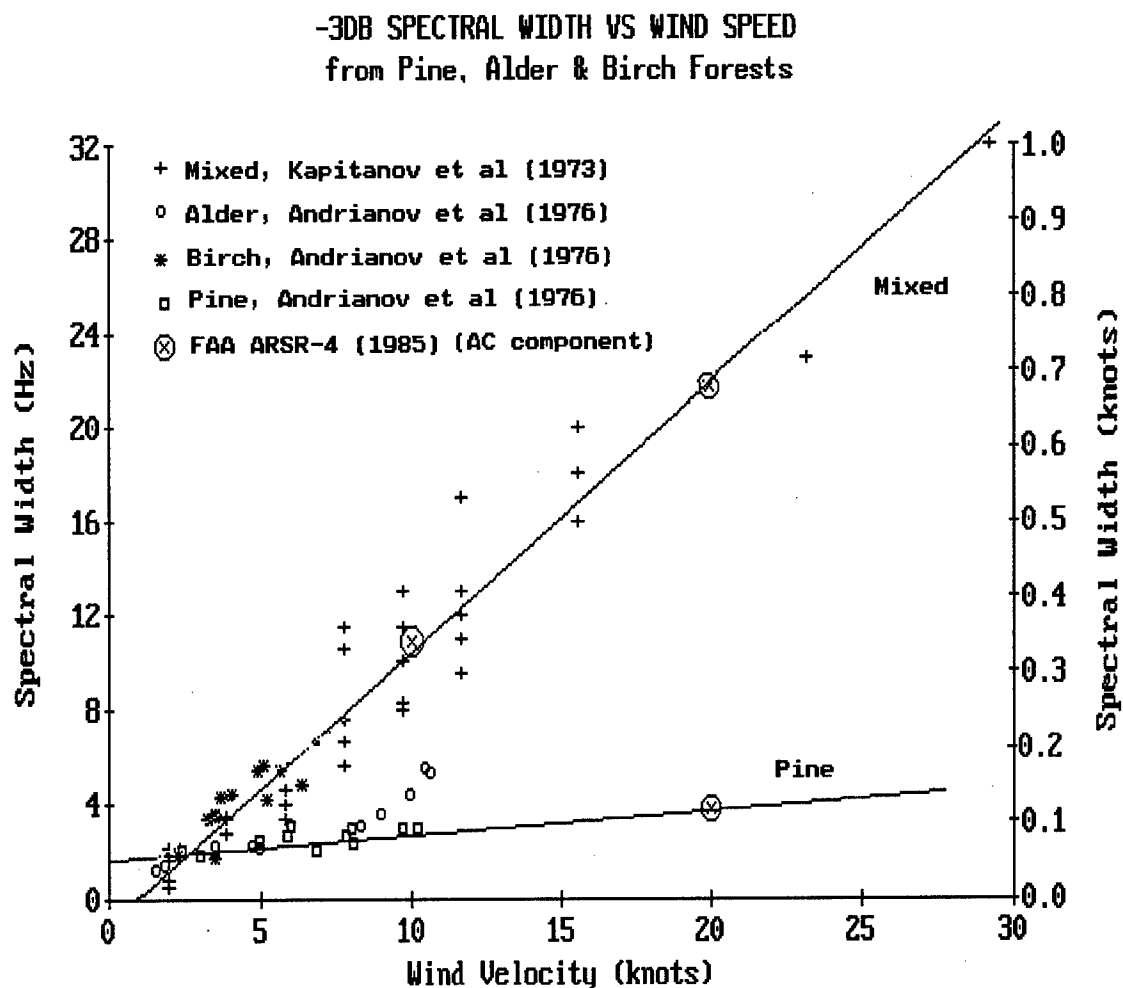


Figure 5.7 Measured -3 dB spread (one-sided) versus wind speed

6.0 MAN-MADE STRUCTURES, VEHICLES AND VESSELS*

6.1 Introduction

A major clutter source on the terrain and sea are the many large man-made objects built or moving on the surface. Most of these objects are dimensionally small compared to the resolution volume of an air defense radar and have been given the name "discrete" or "point" clutter. However, they are also dimensionally large compared to the radar wavelength and can have RCS values far larger and backscatter characteristics that are different than that from the surrounding surface. Consequently, it is important to model these objects separately.

The number of vehicles and vessels in the US can be related to the population. Figure 6.1 presents the current estimates as of 1978 for autos, bicycles, trucks, motorcycles, buses, railroad cars, recreational boats and freight vessels. Similarly, the number of residential and commercial buildings in the US as of 1985 is approximately 10^8 or about .4 buildings per person.

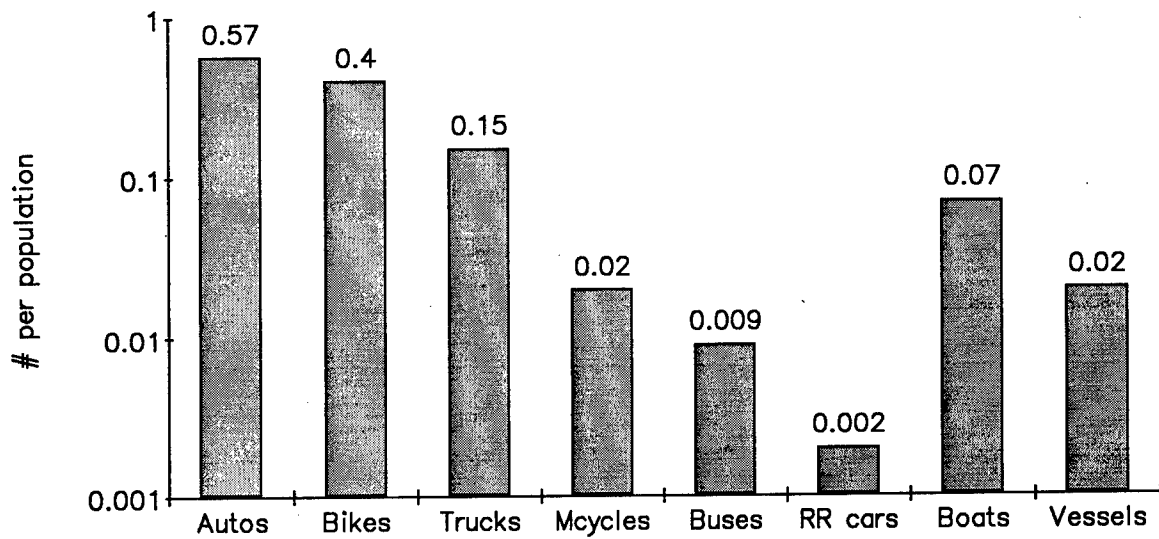


Figure 6.1 Relative population of Vehicles and Vessels in the US (Derived from Environmental Trends (1980))

* Except where otherwise referenced, most of the statistics on population and man-made structures, vehicles and vessels were obtained from the Statistical Abstract of the US (1989)

In order to use such statistics in this clutter model, it is assumed that the density of buildings, vehicles and vessels per square mile are also related to the population density. As will be shown in the following sections, this assumption leads to a useful description of urban, suburban and rural regions in terms of the high, medium and low density of manmade structures, respectively.

6.2 Population Density

The dominant pattern of population distribution in the last 50 years has been the movement to coastal areas. Figure 6.2 shows five general regions and their estimated average population density as of 1987. Nearly 53 % of the Continental US (CONUS) population resides in the 50 mile width represented by these coastal regions. Since the primary operating environment of an air defense system is along these coastal areas, the statistics from these areas are the most important.

The population density has a significant spread about the mean values. An analysis of the Atlantic Coast reveals that 3.3% or about 4000 sq miles have population densities over 4500 and .5% or 584 sq miles have population



Figure 6.2 Population density along major coasts, 1987

densities over 10000 persons per square mile. This represents a highly skewed density function which may be approximated by a log normal with a median of 294 (24.7 dB) and a standard deviation of 6 db. The standard deviation is similar for the other regions and the median values are .66% of their average values. (Figure 6.3)

To use these distribution in later sections, two other parameters have to be defined. First, while urban and rural areas are obviously represented by high and low population densities, the boundary between the two is not clear. This model will use the term urban to include both urban and suburban regions and define urban densities to be above 300 persons per square mile.

Second, if a small area comparable to a radar resolution cell ($\approx .1 \text{ nm}^2$) has a certain density, it is highly likely that the adjacent cells will have a similar density. No statistics were found describing this parameters. In this model, this characteristic will be represented by an exponential correlation function

$$q(D) = \exp(-R/D)/D$$

where D is assumed to be one nautical mile for urban and .1 nm for rural.

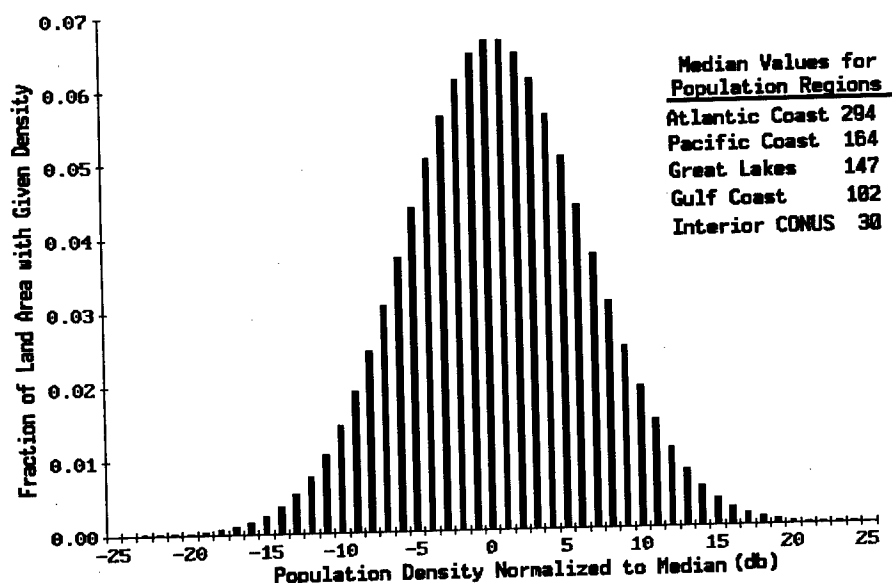


Figure 6.3 Assumed normalized population density

6.3 RCS Distributions

6.3.1 Buildings

There are approximately 10^8 buildings or .4 buildings per person in the CONUS. Therefore, the pdf of the building density along the Atlantic Coast is log-normal with a median of 118 with a standard deviation of 6 dB. Figure 6.4 presents the distribution of building sizes as of 1985. Approximately 90% of these buildings are three stories high, or less. For n story squarish structures, the area of one side can be estimated by

$$\text{Area} \sim (10n+5) * (\text{FS}/n)^{.5}$$

where FS is the floor space in square feet. Taking a weighted average over all n story structure,

$$\text{Area} \sim 18 (\text{Floor Space})^{.5}$$

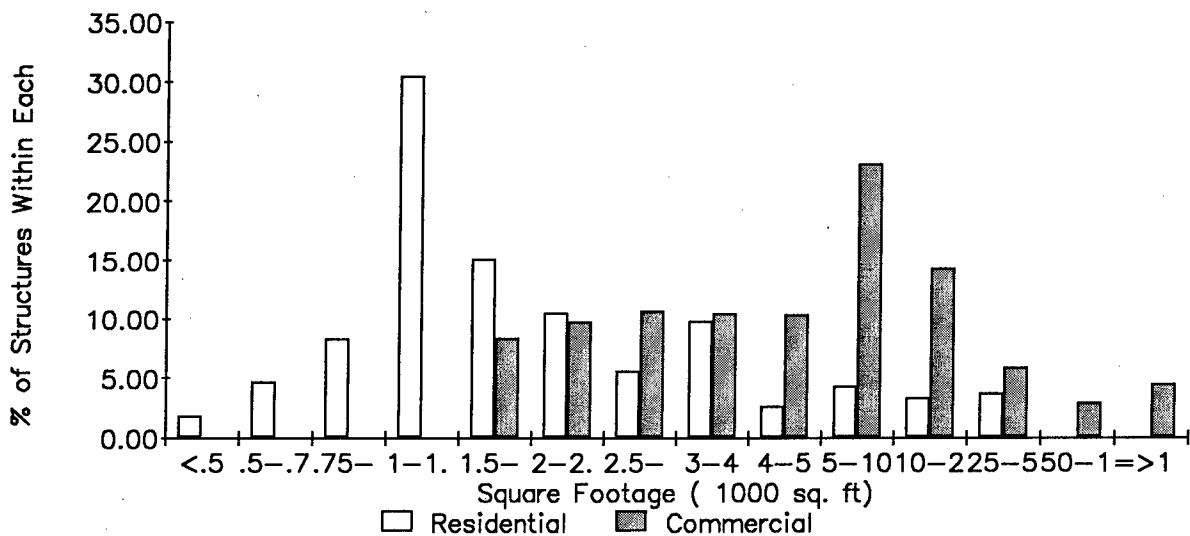


Figure 6.4 Distribution of the size of Residential and Commercial Buildings
(Derived from Statistical Abstract of the US (1989))

Using a relationship similar to that given in Rivers and Katz (1979), an estimate of the median RCS from a building can be given as

$$\text{Median RCS} = 8.5 \log(\text{floor space}) + 4.24 \log(f) \text{ dBsm}$$

where floor space is in sq. ft and f in ghz.

Figure 6.5 compares the derived distribution of median building RCS at UHF using the size distribution given in Figure 6.4 and a log-normal fitted to the median and 84 percentile. While the derived distribution presents a higher percentage of high RCS buildings, the formulas are approximate and do not account for shadowing. Therefore, the log-normal approximation is used as a reasonable approximation to the distribution of building RCS. The standard deviation is approximately 3 dB and the median values for UHF, L-Band and S-Band are 25, 27 and 28.5 dB, respectively.

The density function of median RCS/nm² throughout a region can be given as

$$p(\text{RCS/nm}^2) = \int_0^{\infty} p(\text{RCS/building}) p(\text{buildings/nm}^2) d(\text{buildings/nm}^2)$$

Figure 6.6 presents the resulting distribution functions for the Atlantic coast and provides the scale adjustments for the other four regions. For typical resolution cell sizes of .1 nm², the median RCS at L-Band from buildings would be ~ 38 dBsm respectively. For the Atlantic coast, his median value also corresponds to the assumed boundary between urban and rural building densities. Thus, for urban areas, typical values would be closer to the 80% (~45 dBsm) while rural regions would be presented by the 30% or ~35 dBsm. Normalizing these values to the resolution cell size provides equivalent σ_0 of -10, -17 and -25 dB for urban, intermediate and rural areas. The values compare well with the measured values given by Daley et al (1968).

The RCS of a building fluctuates about its median value as a function of aspect. The distribution is assumed to be log normal with a standard deviation of 5 dB. The aspect change required to obtain an uncorrelated sample of this distribution depends on the length L of the building and λ the radar wavelength

$$\theta \sim \lambda/L$$

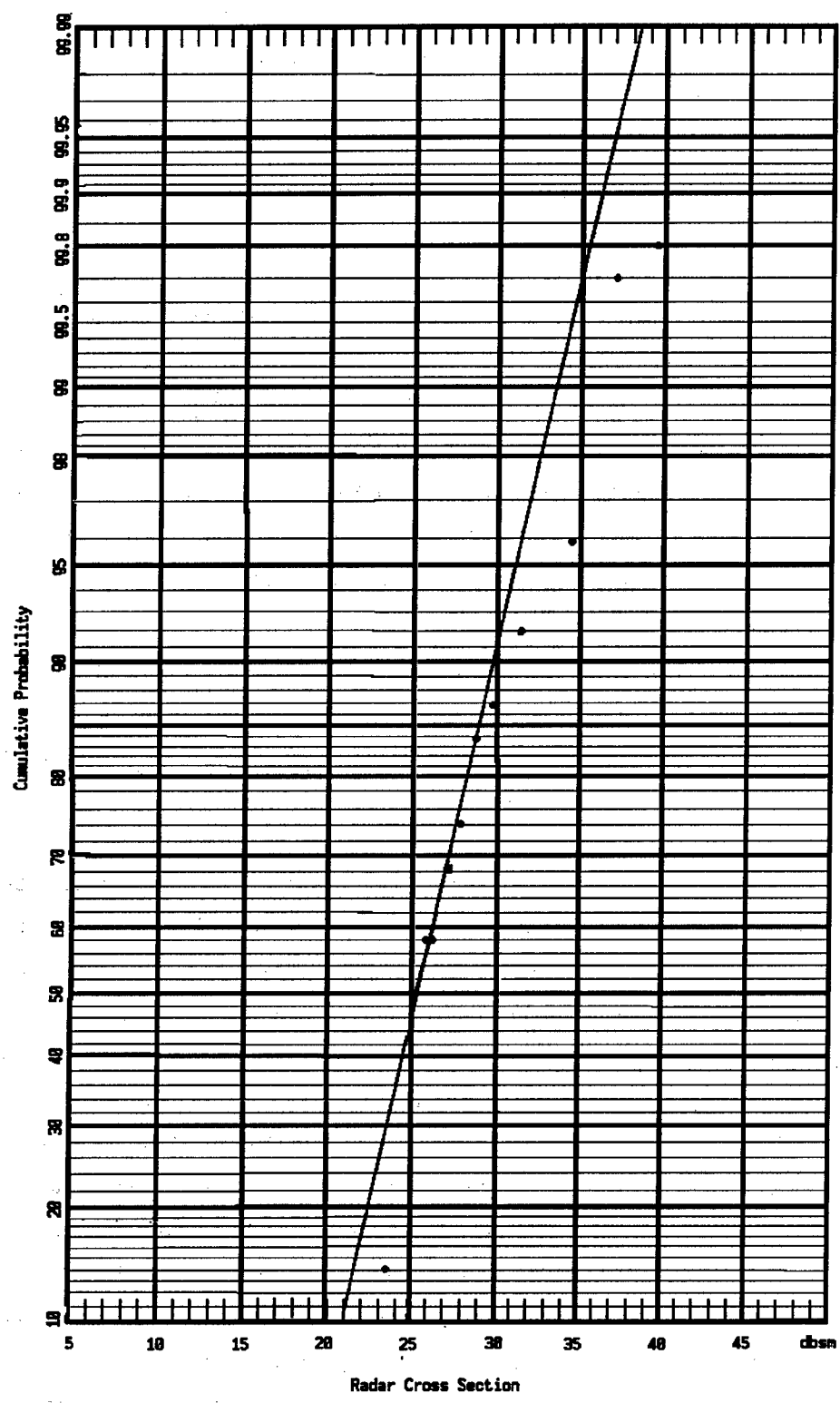


Figure 6.5 Distribution of derived median RCS of building distribution given in Figure 6.4

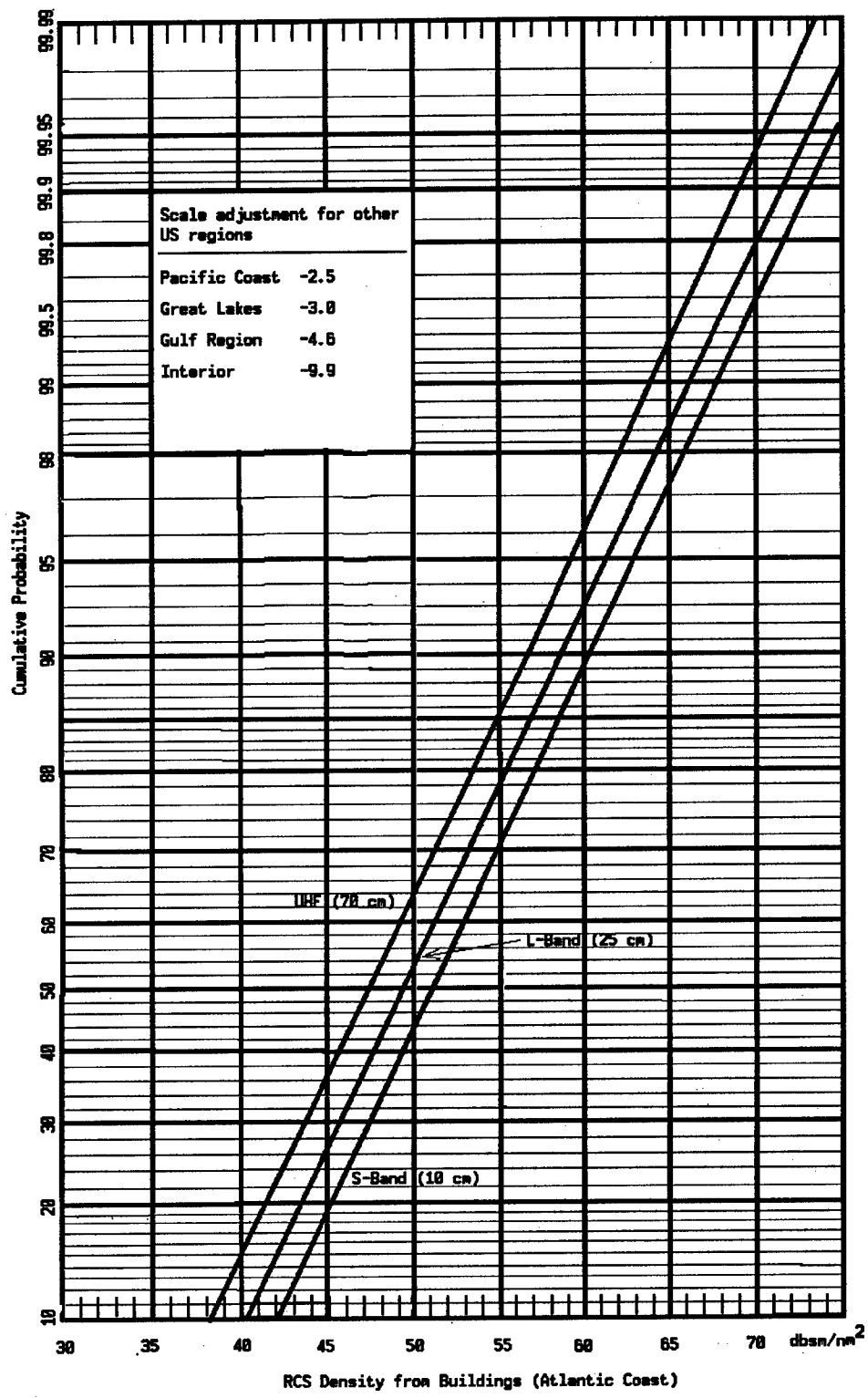


Figure 6.6 Statial distribution of building RCS for the Atlantic Coast.

Inverting the formulas given above relating the area of a side and median RCS and assuming a squarish area, θ can be related to the RCS of a building by

$$\log \theta \approx -1 + .75 \log \lambda - \text{RCS(db)}/17$$

At UHF, for RCS of 0, 30 and 60 dBsm, θ would be .077, .0013 and $2.3 \cdot 10^{-5}$ radians, respectively.

6.3.2 Vehicles RCS

No measurements of vehicle were found in the UHF through S-Band frequency ranges. However, a review of measurements at HF and in the mm bands indicate reasonable values for vehicles, trucks and motorcycles to be 5, 15 and 2 dBsm, respectively. The weighted average is approximately 10 dBsm. As shown in Figure 6.1, the median population density of highway vehicles is .75 the population densities given in Figure 6.2. Therefore, the median RCS densities range from 33.4 dBsm per sq. mile in the Atlantic Coast to 23.6 dBsm per sq. mile in the interior. Figure 6.7 compares the RCS density of vehicles with that of buildings. Since a high density of vehicles would be expected to be collocated with a high density of buildings, the larger RCS of buildings will dominate. Therefore, for air defense systems with large resolution cells, only the density of moving vehicles are of importance.

There are 3.9 million miles of paved roads, streets and highways in the US. With an area of about 3.0 million square miles in the CONUS, this results in an average of ~1 linear mile of paved road per square mile of surface. During 1987, 186 million cars, trucks, buses and motorcycles traveled 1.84 trillion vehicle-miles, an average traffic rate of 1,292 vehicles passing a given point per day.

However, the traffic rates are hardly uniform over the country. The rural interstate highways along the Atlantic, Gulf and Pacific coasts have traffic rates of over 15,000 vehicles/day. In 1967, the estimate traffic rate was up to 75,000 vehicles/day for rural highways within the Boston - Washington corridor, Southern California and around the Great Lakes. Since the number of motor vehicles and vehicle miles traveled has increased 90% between 1967 and 1987, it is reasonable to assume the traffic rates in these corridors

**RCS per Square Mile
from Buildings and Stationary Vehicle**

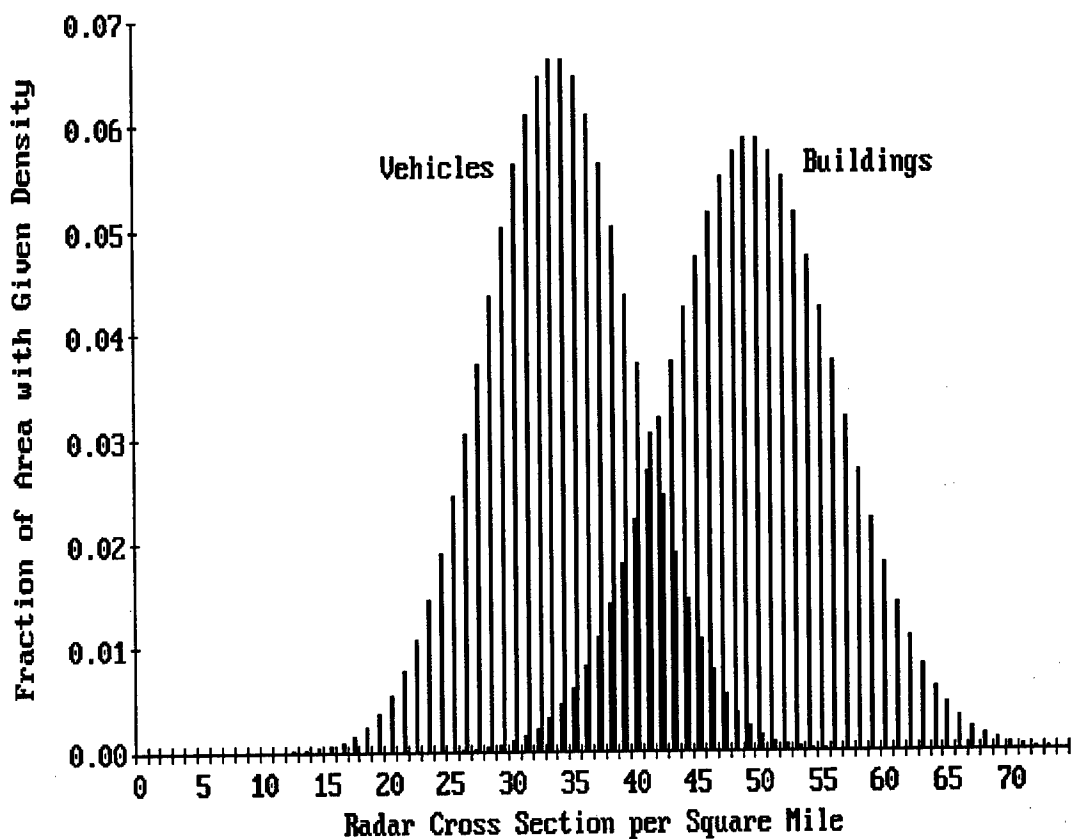


Figure 6.7 A comparison of the RCS distributions for vehicles and buildings

have increased accordingly. In order to model this variation in vehicle traffic, two types of roadways will be represented, a dual lane interstate highway and a single lane rural road.

The interstate highway system has approximately 39,000 miles, about 1 % of the total paved roads. This works out to an average of about .01 linear mile per square mile. Using the assumption that road density is proportional to population density, the Atlantic, Pacific, Great Lakes and Gulf coastal areas would have .054, .03, .027 and .019 linear miles per square mile. Using the typical traffic flow rates for urban and rural areas, the density of vehicles given in Table 6.1 can be obtained. The sample distribution of vehicle speed is Gaussian with a standard deviation of 5 mph. The speed of each vehicle is constant once assigned.

	Urban	Rural	Rural
	Interstate	Interstate	Single-lane
	Highway	Highway	Roads
Traffic Flow/Hr	2400	660	50
Average Speed (mph)	50	55	50
Average Number of Vehicles/ lin. mile	4815	12	1

Table 6.1 Summary of vehicle traffic for Interstate and Rural roads.

The average RCS of each vehicle is 10 dBsm. The fluctuation with respect to aspect is exponential and the angular change to obtain an uncorrelated sample of this distribution can be calculated using the formula for buildings.

6.3.3 Boats and Ships

In 1987, 58,307 ocean going vessels visited the ports of the US. With a total tonnage of 521 million tons, the average tonnage per ship was 9,000 tons. The average tonnage per ship in the major merchant services is about 30,000 tons with few supertankers ranging over 500,000 tons. To represent this range of tonnage, the tonnage of ocean-going ships is assumed to follow an exponential distribution with a mean of 10,000 tons.

The average RCS of large ships can be related to its tonnage using (Skolnik (1974))

$$RCS = -12.8 + .5 f_{db} + 1.5 M_{db} \text{ (dBsm)}$$

where f is the frequency in Ghz and M is the tonnage. Therefore, the RCS for these ships range from 44 dBsm at UHF for 9000 tons to 75 dBsm at S-Band for the larger supertankers.

The RCS from ships can fluctuate as a function of time for a constant aspect and as a function of aspect. For ships of this size, a log-normal distribution is recommended for the temporal scintillation about the mean RCS (Northam 1985). A standard deviation of 5 db is also suggested. The

correlation function for this scintillation follows an exponential decay where the appropriate time constant depends on the weather, and if the ship is moving or at anchor. The 1 second time constant used in the ARSR-4 model assume calm sea conditions and an anchored ship. In rough weather, or if the ship is moving and changing aspect with respect to the radar, time constants as short as 10-20 msec are possible. The angular change required to obtain an uncorrelated sample of the density function is the same given for buildings.

The most likely location for these ships is anchored on or just off the coast near dense population areas. In this model, the relative population of ships is 1 ship per 5000 of coastal population. For the Atlantic coast with an average density of 445 per square mile, this corresponds to an average of 1 ship per 11 square miles. For moving ships, an average speed of 10 knots is suggested.

Recreational craft on the coast and in the lakes and rivers are smaller and more frequent. The relative population of recreational craft is 70 per 1000. Therefore, along the Atlantic Coast, the average density of these craft is 31 per square mile. The RCS of these small boats is in the order of 0 dBsm and the scintillation distribution is exponential.

7.0 BIRDS AND INSECTS

While using low-powered, long wavelength radar systems in the 1930's, radar operators became experienced in identifying the radar clutter echoes from targets, buildings, weather and even the sea. However, as higher power, microwave systems were installed, operators became increasingly aware of randomly distributed moving dot-like or distributed returns where no aircraft and other visible targets existed. Since no explanation could readily explain their presence, the term "angels" were applied to them. Since then, numerous studies have shown that the causes of angels include birds, insects, inhomogeneities in the atmospheric refractive index and even particles in the atmosphere such as dust and smoke. The clutter from the latter two causes are considered in other sections. This section will address the most commonly observed causes of angels, birds and insects.

Bird and insect angels presented infrequent problems to early systems with human operators. First, the RCS of the aircraft threats typically exceeded 1 square meter, well above the typical RCS from bird flocks and insect swarms. This allowed use of simple processing schemes such as sensitivity time control (STC). Secondly, when angels were detected, the operators had the experience to ignore the clutter based on the shape and intensity of the PPI display and their true velocity. Finally, except for the few times when international tensions were high, most operators relied heavily on the transponder systems such as IFF which were free of angel clutter. Only in a few areas near nesting, wintering or major migration and staging areas was angel clutter an important problem.

With the advent of stealth technology, the open literature reports that the RCS of a stealth aircraft will have the RCS of a bird. Therefore, the next generation of military air defense systems is forced to reassess the angel problem. Figure 7.1 should give a qualitative idea of the environment of an ADI system. This photograph, which was taken by RADC in 1984 in support of tests performed for HQ MAC, shows the PPI presentation of a GPN-21 GCA radar located at Dover AFB, DE during the fall of 1983. The maximum displayed range is 12 nm with bright range rings every 4 nm. The sensitivity is $< .01$ sm within the 3-pulse MTI passband and $< .1$ sm at 15 knots. Most of the clutter within 2 nm of the radar is ground clutter. Beyond 2 nm, all but a very few echoes are returns from geese, gull, blackbirds and other species of birds.

Review of the time-lapse photography reveals that there were even more low-probability detections that are not well portrayed in this photo.

The environment displayed in this photo is the norm for the coastal areas between October and March where the waterfowl and other migratory birds winter. Obviously, mean RCS is no longer a useful discriminant and the lower detection threshold will require an automated system to sort through thousands of detections looking for a threat. Vaughn (1974) gives several possible discriminants including parameters measurable with sufficient time history (wingbeat rate, flap-pause, RCS amplitude statistics, doppler spectrum, true velocity). This section provides a model which summarizes some of these parameters and allow the design of a measurement radar system that can further explore these possible discriminants.

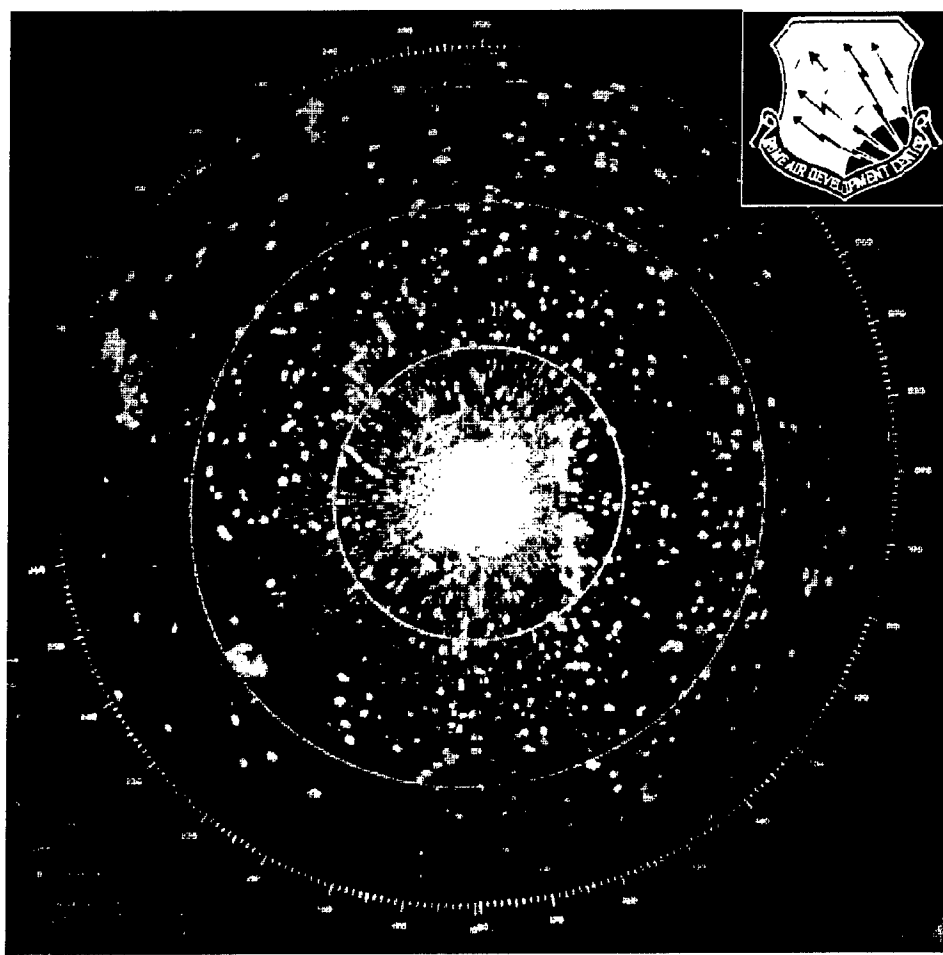


Figure 7.1 PPI presentation of bird clutter observed by an S-Band GPN-21 GCA radar. Maximum range is 12 nm with bright range rings every 4 nm. Measurements taken by RADC in 1983. For further background, refer to Simkins et al (1984)

7.1 Bird Angels

The RCS distributions of observed bird angels depend on the RCS of the individual birds, the number of birds per angel, the density of angels per nautical mile and the distribution of radar resolution sizes with range. The ATR model (1981) and the ARSR-4 model (1984) presented these models for moderate sensitivity ground-based radars. The approach used to create these models will be used in this section to derive a bird angel distribution for use in ADI.

Species	Note	Frequency Band			
		UHF	L	S	C
Grackle[1]	Average	-43		-26	-28
Pigeon [1]	Head				-40
	Broadsides				-20
	Tail				-40
	Average	-30		-21	-28
Sparrow [1]	Head				-46
	Broadsides				-32
	Tail				-47
	Average	-56		-28	-38
Duck[2]	Average	-12			
[3]Front Quadrant Avg.			-18 (HH)		
" " "			-24 (VV)		
Rear Quadrant Avg.			-21 (HH)		
" " "			-25 (VV)		
Goose [3]	Average		-13		
Western					
Sandpiper [4] Average				-22	

Table 4.1 Measured RCS in dBsm of Individual Birds

[1] Konrad, Hicks and Dobson (1968), also Nathanson (1969)

[2] Blacksmith and Mack (1965)

[3] Mack, Blacksmith and Kerr (1979)

[4] Vaughn (1974)

7.1.1 Mean RCS of Bird Angels

Table 4.1 presents measured RCS values of individual birds. These measurements are typical in that there are few measurements made in the UHF to S-Band frequency range and few species have been accurately measured. In order to present the bird clutter problem over a range of frequencies for a range of species, a model for bird backscatter is required.

The simplest model is a water sphere with a weight equal to the weight of the bird. The RCS of this model is displayed in Figure 7.2 for wavelengths of .86, 3.21 and 10 cm as well as the "optical" RCS which is given as

$$(6) \pi r^2 \quad \text{for } \lambda < \lambda_t$$

$$(7.1) \quad \sigma_{\text{opt}} = \{ \quad (6) \pi r^2 (\lambda_t/\lambda)^4 \quad \text{for } \lambda > \lambda_t$$

where r is the equivalent sphere radius in meters = $.0062 (\text{wt})^{.333}$, λ_t is the threshold wavelength between Rayleigh and optical scattering = $7 (\text{wt})^{.333}$ cm and wt is the bird weight in grams. For comparison, the measured RCS of birds and insects and several other models are also presented. σ_e and σ_s represent the respective end-on and broadside of the optical RCS for 2:1 and 5:1 prolate spheroids while the RCS of the 1/2 wavelength dipoles = $.86 \lambda^2$. Most of the bird measurements fall between the broadside and end-on RCS of the 2:1 spheroid and with average values close to the sphere model.

Another model for bird RCS is a "cylinder" model proposed by Heidbreder et al (1971). This model which was published later in the open literature by co-author Pollon (1972) states that the mean RCS σ could be related to a bird's length and weight as follows:

$$\sigma = \{ \quad \sigma_{\text{pk}} (\lambda/\lambda_r) \quad \text{for } \lambda < \lambda_r \\ \sigma_{\text{pk}} (\lambda_r/\lambda)^4 \quad \text{for } \lambda > \lambda_r$$

where $\sigma_{\text{pk}} = .1 \lambda_r^2$, $\lambda_r = k (\text{wt})^{.333}$, $k = 5.4 \text{ cm/gram}^{.333}$, wt is the bird weight in grams and λ is the radar wavelength in centimeters. σ_{pk} describes the peak RCS when λ_r is approximately twice the bird's equivalent cylinder length.

Figure 7.3 compares this model with several measurements and the "optical" RCS of an equivalent water sphere. Both models correlate well for Rayleigh

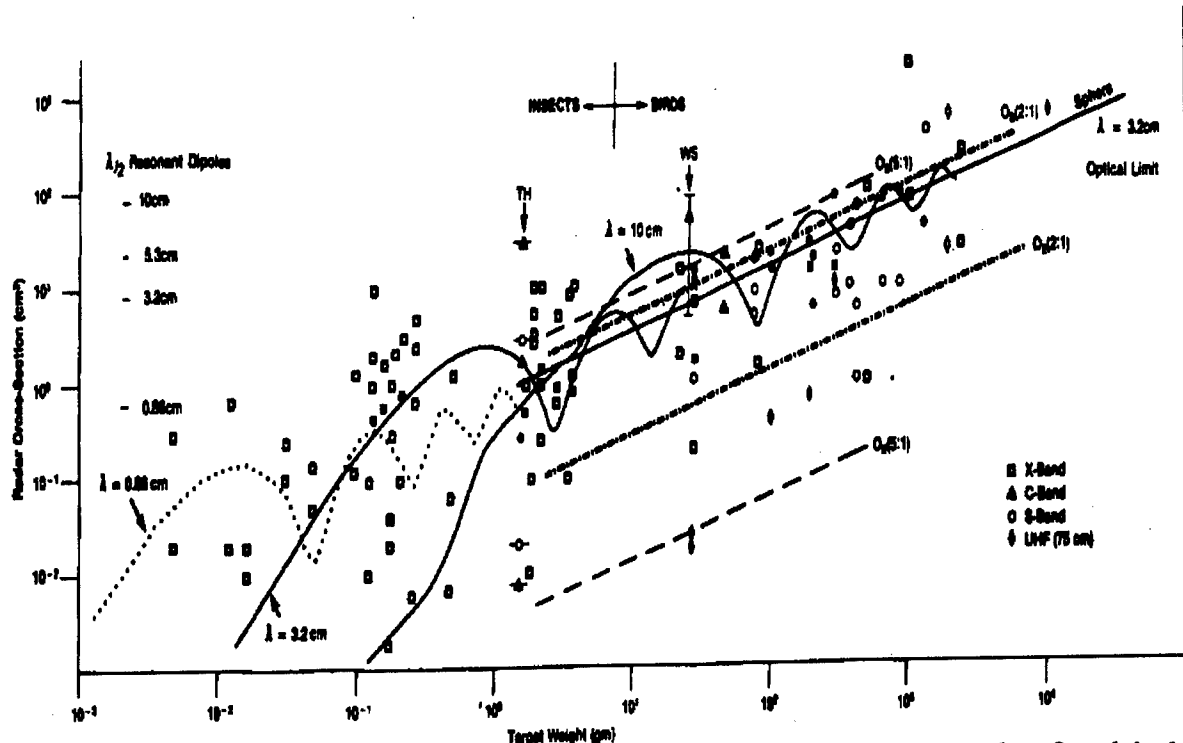


Figure 7.2 A comparison of the radar cross section versus weight for birds, insects, spherical and prolate spheroid models. (Vaughn (1985))

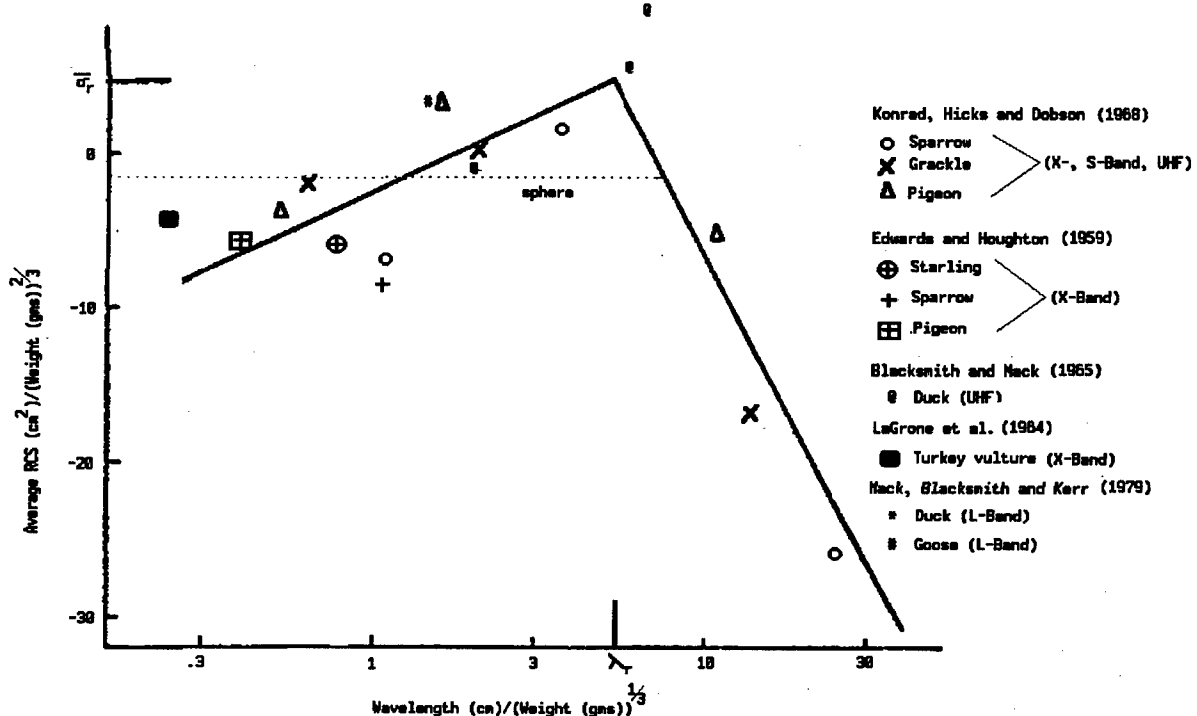


Figure 7.3 Comparison of the cylinder model (Heidbreder et al 1971; Pollon 1972) and the optical RCS of an equivalent water sphere.

scatterers. The RCS for the cylinder model exceeds the optical water sphere RCS in the resonance region to a similar degree as the water spheres given in Figure 7.2 and predicts less RCS for higher frequencies. With the limited data portrayed in Figure 7.3, the cylinder model seems to provide a better prediction of RCS. However, the larger data set given in Figure 7.2 shows a much wider spread in the data. Since the detailed RCS from real birds are not accurately described by any of these models, these resonance effects only complicate the model without providing much useful information. Therefore, the simpler "optical" model will be used for an estimate of the mean bird RCS.

Since the formulas use weight while much of the available ornithological data presents length, a version of the weight-length relationship indicated by Heidbreder et al (1971) will be used.

$$(7.2) \quad \text{wt}_{\text{dbgm}} = -5.6 + 3 l_{\text{dbin}}$$

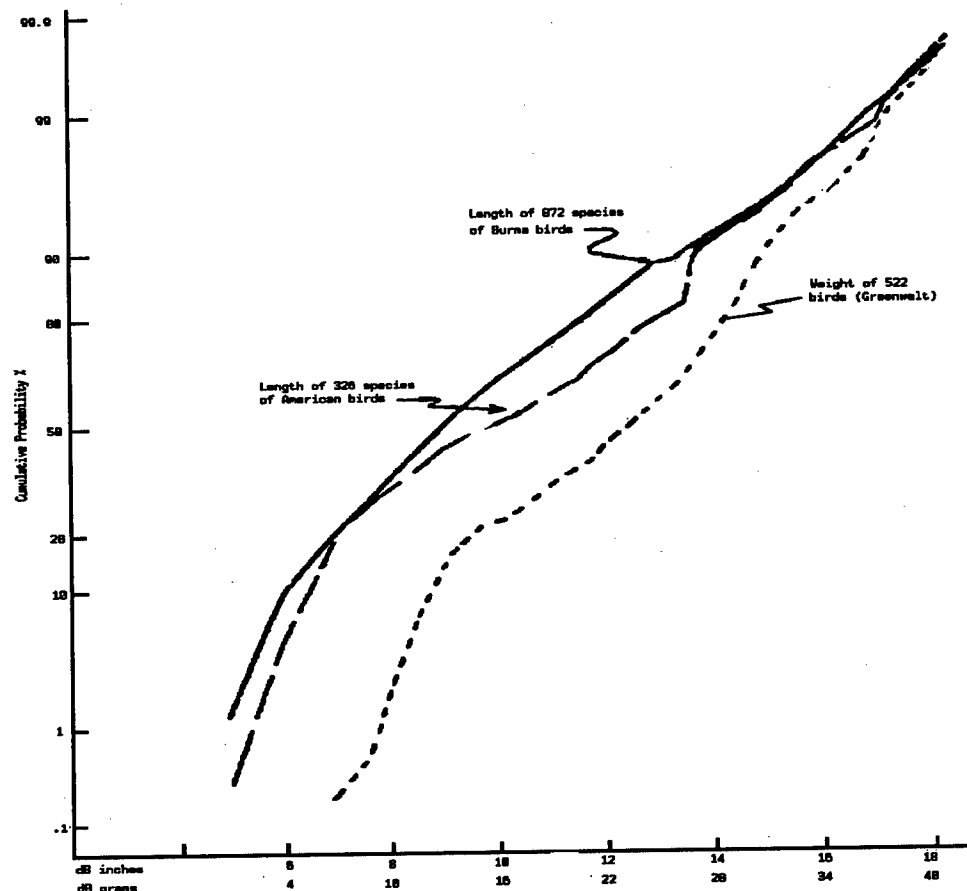
Note that this model is used only as an estimate the mean RCS and does not represent a model for polarization or other characteristics. Vaughn (1985) notes that few measurements differential reflectivity ($\sigma_{\text{hh}}/\sigma_{\text{vv}}$) have been made. In measurements using the CHILL radar in Illinois, Mueller (1983) measured an average differential reflectivity over 360 degrees of azimuth of 3 dB. Measurements by Mack et al (1979) seem to agree with this value on an average basis. Therefore, the mean values calculated using the "optical" sphere model present values for horizontal polarization. Mean values for vertical polarization are assumed to be 3 dB less.

The distribution of bird lengths and weights in the US and the rest of the world varies greatly. Figure 7.4 shows the lengths and weights of bird species for CONUS and Burma derived from the ornithological literature by Heidbreder et al (1971). The bird species lengths vary from approximately 3 to 72 inches with a median value of about 9 inches. The bird species weight varies from approximately 5 grams (.2 ounces) to about 40 kilograms (22 lbs) with a median weight of approximately 200 grams (7 ounces).

If the population of birds were equally distributed over all weights and lengths, the distribution given in Figure 7.4 could be used directly to derive the distribution of RCS for each frequency. However, the actual distribution varies with location and season. Figure 7.5 presents the results of a 1968 winter census at three locations. This census revealed that larger birds are

more predominant in the coastal areas (San Diego, New Jersey) than in the inland area (Tennessee). This is reasonable considering that the coastal areas have a larger portion of the wetlands and wildlife refuges used between October and March by waterfowl and other larger migrating birds.

Pollon (1972) derived distributions of bird RCS assuming that the population of bird species were inversely proportional to their weight. This assumption leads to distributions with lower RCS due to the emphasis on the smaller birds. While this assumption is reflected somewhat by the Tennessee data and may be appropriate for the short range helicopter-borne foilage penetrating radar that he was concerned with (see Heidbreder et al (1971)), it is not appropriate for a coastal defense system. Figure 7.5 presents the



Bird Length or Weight

Figure 7.4 Distribution of the lengths and weights of birds in the US and Burma. (Heidbreder et al 1971)

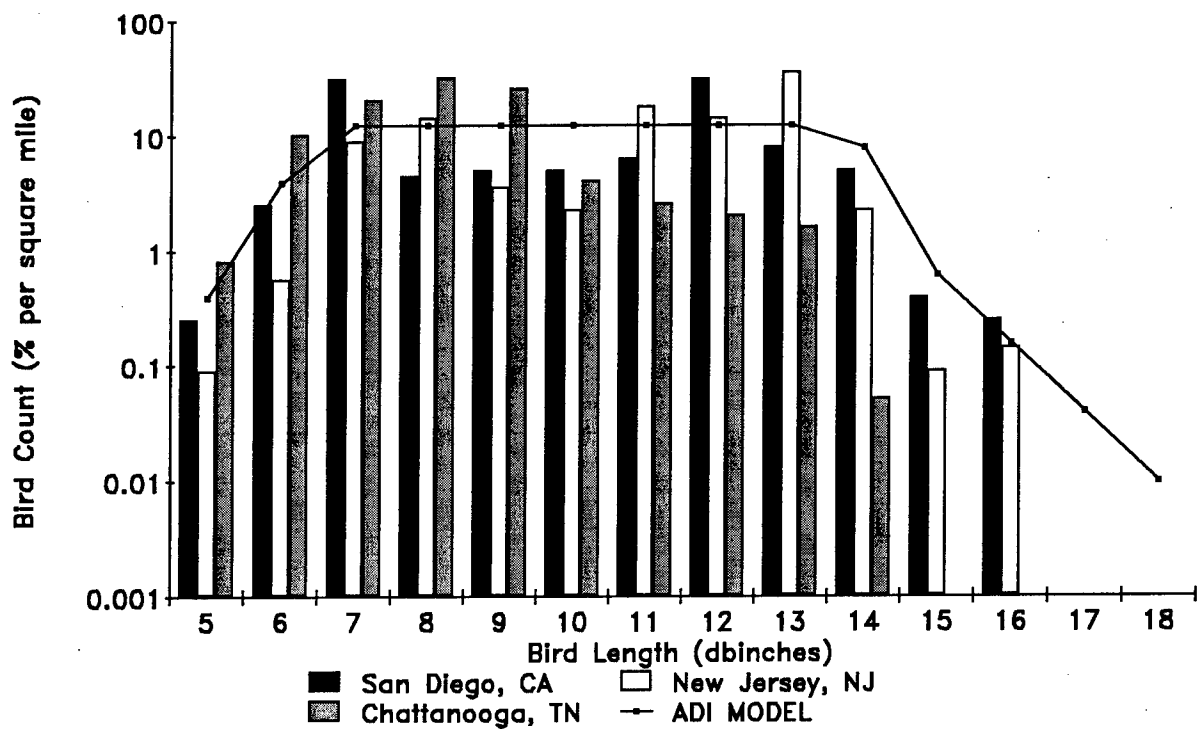


Figure 7.5 Relative Bird Population versus Length (Derived from Heidbreder et al (1971)

ADI model used in the subsequent analyses. Using the "optical" sphere model (1), the weight-length relationship (2) and the ADI bird density given in Figure 7.5, the distribution of mean RCS for single birds can be calculated. Figure 7.6 presents this probability distribution for S-Band, L-Band and UHF. The distribution for S-Band and L-Band are virtually identical because most of the bird length population have dimensions comparable to these wavelengths and the spherical model is used. For UHF, most bird lengths are in the Rayleigh region resulting in more spread in the distribution.

7.1.2 Number of Birds and Angels per Square Nautical Mile

The distribution of angel RCS observed by a high sited system is a function of the distribution of the bird RCS, the number of birds per angel, the number of angels per square mile and the number of square miles in a

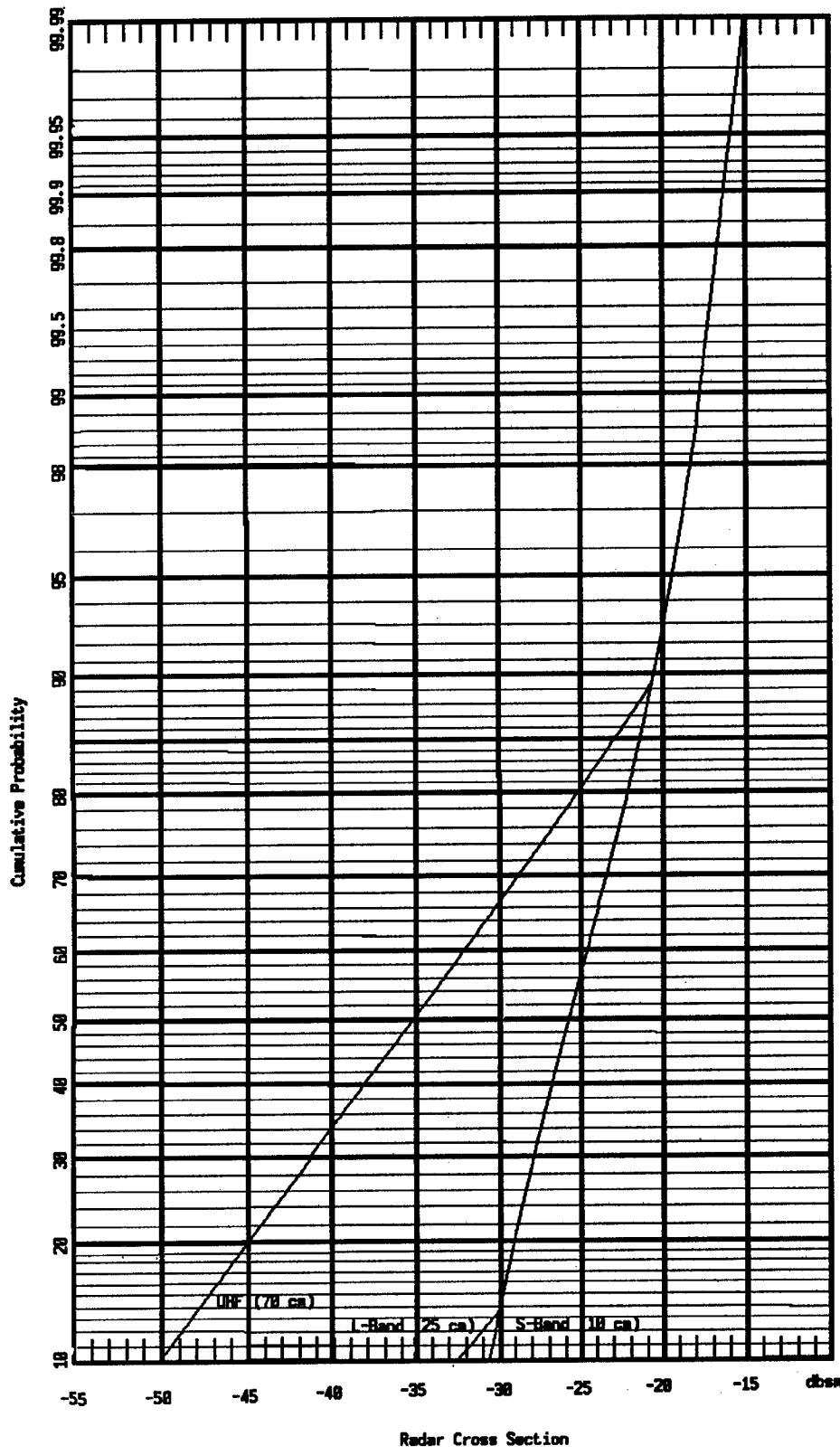


Figure 7.6 Derived RCS distribution of individual birds.

resolution cell. The derivation of the ARSR-4 angel model used the bird RCS model given above, 4 birds per flock and the distribution of range cell sizes between 5 and 200 nm. An estimate of the density of birds was based on an analysis of the data collected during the 1952 moon-matching observations (Newman and Lowery, 1964) published by Pollon (1972). One interpretation of his conclusions is that no birds were observed for 13% of the time and the density for the remaining observations was approximately log-normally distributed with a median of ~30 birds/ sq. mile and a standard deviation in the order of 6 dB. Using work performed by Harper (1958) and Nisbet (1963), he derived a density for birds averaged over all seasons and time of day which provided no birds for 36.2% of the time and a log-normal shaped density (median ~ 10 birds/sq. mile, std. deviation ~ 6 dB) when birds were present. The derivation of the ARSR-4 model assumed 4 birds (1 angel) per sq mile and a 6 dB standard deviation. After convolution with the densities of RCS and resolution cell sizes, the spread of the resulting angel RCS density was close to 10 dB.

For ADI, both the density of birds per square mile and number of birds per flock or angel were reevaluated. During the winter months, the density of birds in the US is approximately log-normally distributed with an average of 1000 birds per square mile, approximately 3000 birds at the 90 percentile and a median of approximately 600 birds. (Heidbreder et al (1971)) The standard deviation for a log-normal density fitting these values is 4.5 db, almost 1.5 less than that assumed in the derivation of the ARSR-4 model. It can be reasonably assumed that the density of flying birds would have the same shape around a smaller mean value.

Figure 7.7 compares two measurements of bird angel RCS distributions using short range radars with a derived RCS distribution using the ADI RCS model given in Figure 7.6 and a log-normal distribution for number of birds per square nautical mile. The assumed median for the bird density is 100 flying birds per nm^2 (average of ~ 1.4 birds in the $.014 \text{ nm}^2$ ASR-7 cell at 10 nm.) and the standard deviation is 4.5 dB as indicated in the previous paragraph. The resultant derived density for RCS/nm^2 has a median RCS of -25 dBsm with a std. deviation of about 6.5 dB.

The shape of the distribution function compares favorably with the two measured distributions, supporting the choice of standard deviation values. The difference between the ADI prediction and the ASR measurements made along

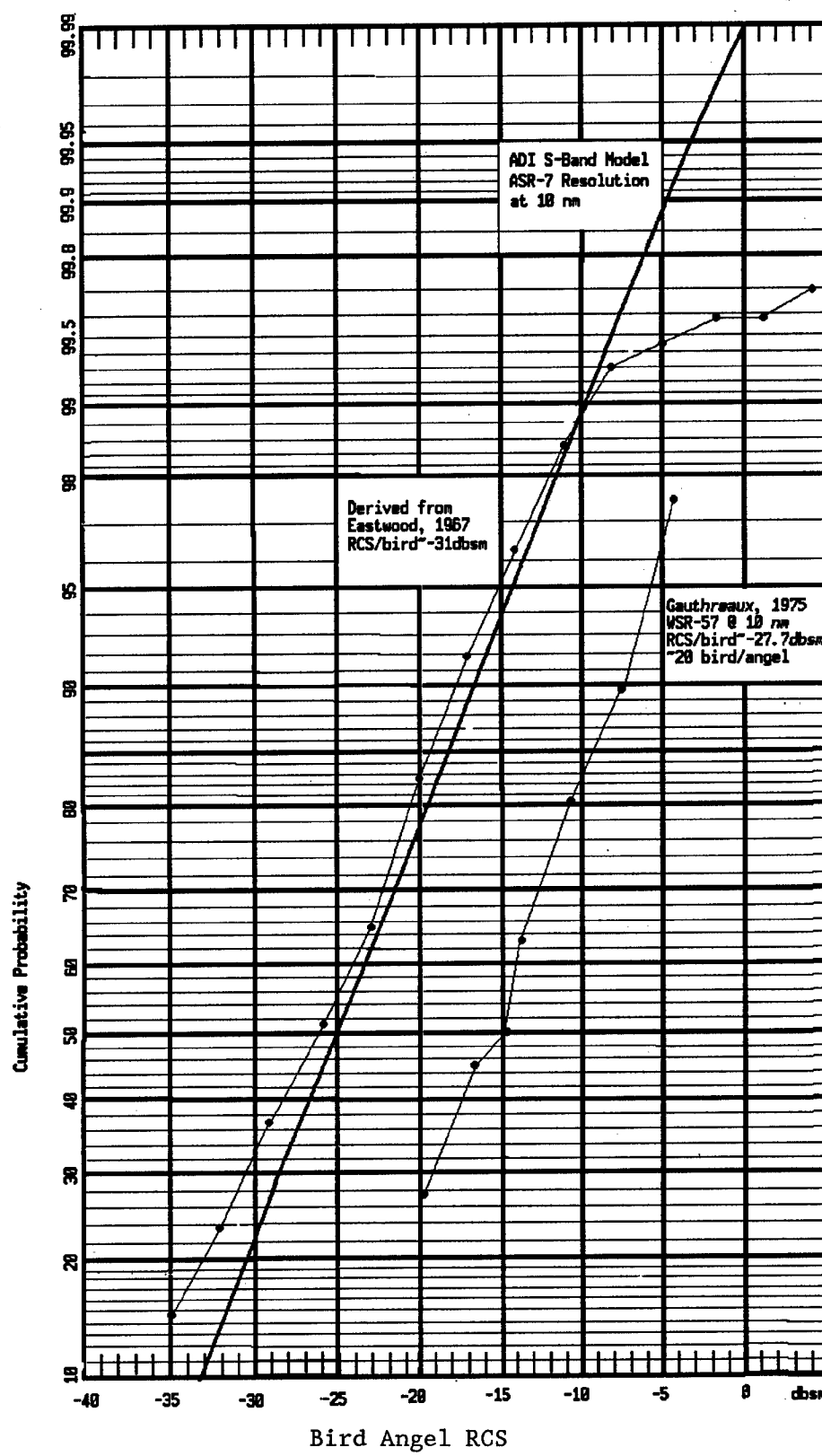


Figure 7.7 Comparison of the ADI model with measured distributions at short range

the Gulf coast (Gauthreaux 1975) is approximately equal to the number of birds assumed per resolution cell. Barry et al (1973) also measured angels within 10 nm using an ASR-7 radar and obtained RCS values of bird angels ranging from .005 to 2 m^2 with an average of $.28 \text{ m}^2$. This compares favorably with Gauthreaux if about 20 birds were assumed per angel. While the ADI curve compares favorably in both shape and median values with Eastman, the latter measured flocks containing 5 to 35 birds with much smaller RCS than the ADI median value. Therefore, while the ARSR-4 model used an average of 4 birds per angel based on the recommendations by Pollon (1972), this value seems too small.

Table 4.2 list some estimates on the number of birds per angel or flock obtained through both radar measurements and visually. Almost all of the radar measurements given in Table 4.2 were made at short ranges with radar resolution cell sizes of .03 square nautical miles or less. The measurements indicate that local densities of birds within a flock can easily exceed 1000 birds per square nautical mile and that 10 to 20 birds per angel is a more realistic estimate.

<u>Author</u>	<u>Observation</u>	<u>Technique</u>
Gauthreaux (1975)	20 birds/angel (avg) 19 birds/angel (median)	Visual and radar
Sutter (1957)	20 - 40 birds/angel	Visual and radar
Hofmann (1956)	150 birds/angel	Visual and radar
Harper (1958)	5 - 30 birds/angel	Visual and radar
Bergman and Donner (1964)	150 birds/angel	Visual and radar
Eastwood and Rider(1966)	5 - 35 birds/angel ~10 birds/angel (avg)	Radar
Nisbet (1963)	2 - 12 birds/angel	Visual and radar

Table 4.2 Number of reported birds per angel

Visual observations also support this conclusion if the number of birds per angel is essentially the same as the number of birds per flock. During migration, flock sizes for geese, ducks and swans near staging areas on the

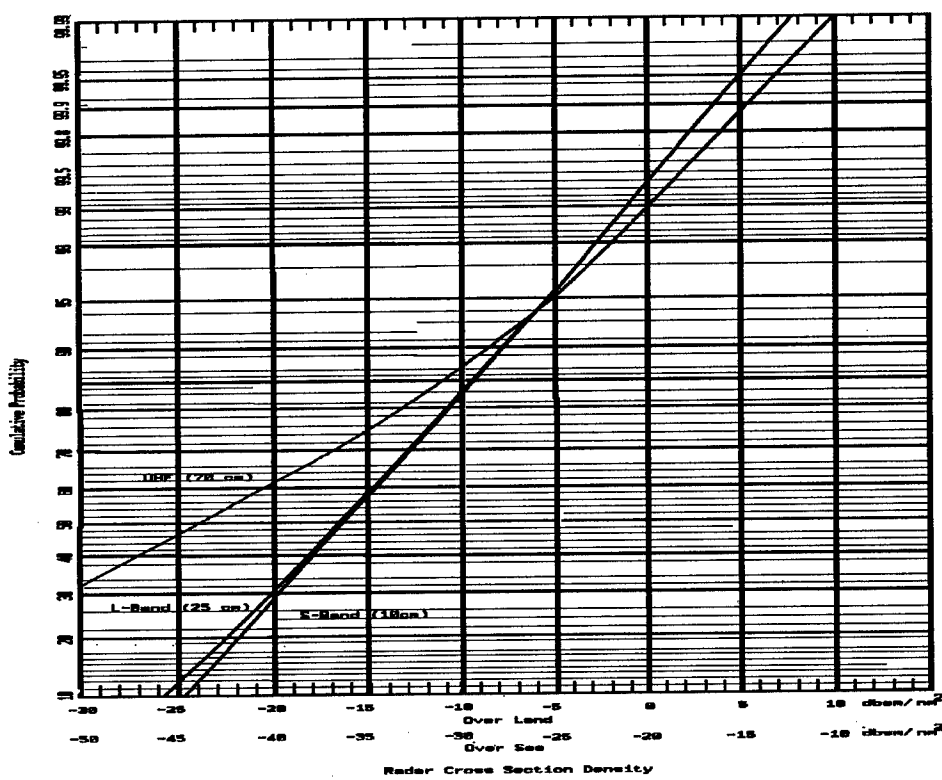


Figure 7.8a Distribution of derived angel RCS density on Gaussian probability paper

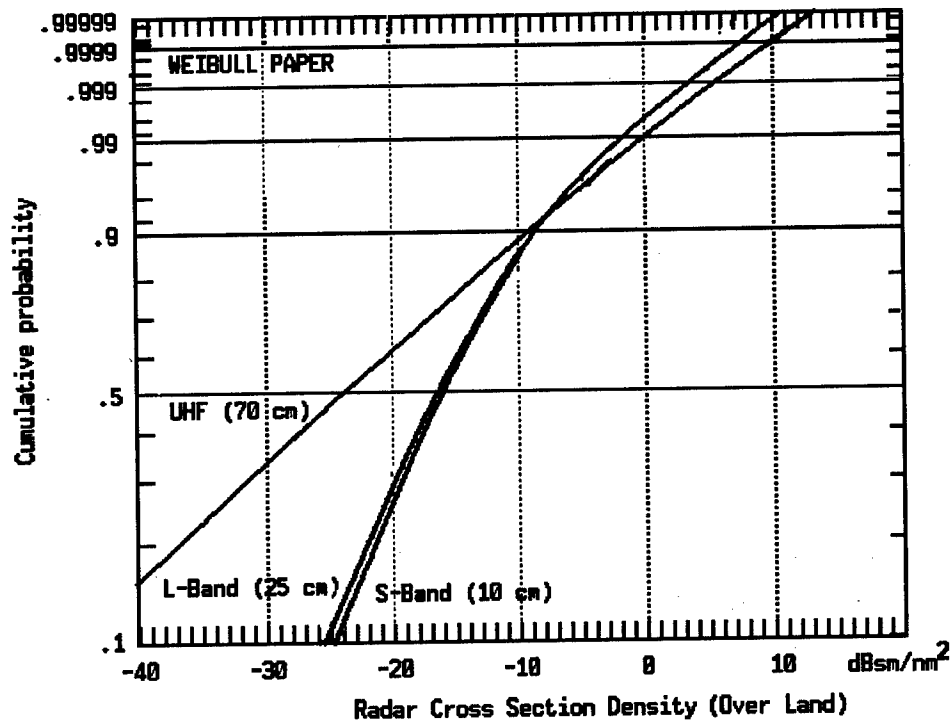


Figure 7.8b Distribution of derived angel RCS density on Weibull probability paper

northern border of the US can range from 20 to over 400 birds. Simkins et al (1984) reported typical flock sizes for geese wintering along the Atlantic Coast ranging from 5 to 30 birds and flocks of blackbirds, gulls and starlings often exceeding 100 birds. With suggested areal densities of 1 to 3 square meters per bird (Gunn and Cockshutt (1965), Blokpoel (1976) and Antonucci (1981)), such large flocks can easily be contained in one ARSR-4 or ADI resolution cell, especially at longer ranges.

Therefore, based on the above observations, the suggested number of birds per angel for ADI is 10. While there is obviously a spread on this value, it is narrow compared to the spread on the other three parameters and will be ignored. Based on the observations referenced above, the number of birds per angel is constant for all bird species. Over the sea beyond a few miles from land, the density of birds falls significantly and a reasonable value is about 1/100th the density on land or 1 one flock of 10 birds per 100 square miles. Figures 7.8 a and b present the distribution of derived bird angel RCS density over land and sea. As shown in Figure 7.8a, the derived angel RCS density for L-Band and S-Band can be approximated by a log-normal with a median of -16 dBsm and a standard deviation of 6.5 dB. Figure 7.8b presents the models on Weibull probability paper. The derived angel RCS density for UHF can be approximated by a Weibull distribution with a median of -24 dBsm and a shape factor of .34.

The density of angel RCS per resolution cell requires that the size of the resolution cell with range be taken into account. In the ARSR-4 model, a simple expression for the density of angel RCS per resolution cell was desired. Since the beamwidths and bandwidths were confined to a narrow range, the density of range cell sizes could be estimated. The resultant density given in ARSR-4 model was obtained by convolving the pdf of the angel RCS/nm² with the range cell size pdf. Thus, only an average number of angels per square mile was given with the spread of the density included in the spread of angel RCS. Since the ADI resolution cell dimensions are not well confined, this will not be attempted here.

7.2 Variation about Mean RCS

The instantaneous RCS of a bird can vary rapidly with time over a wide dynamic range. One reason is that the observed bird RCS is a function of

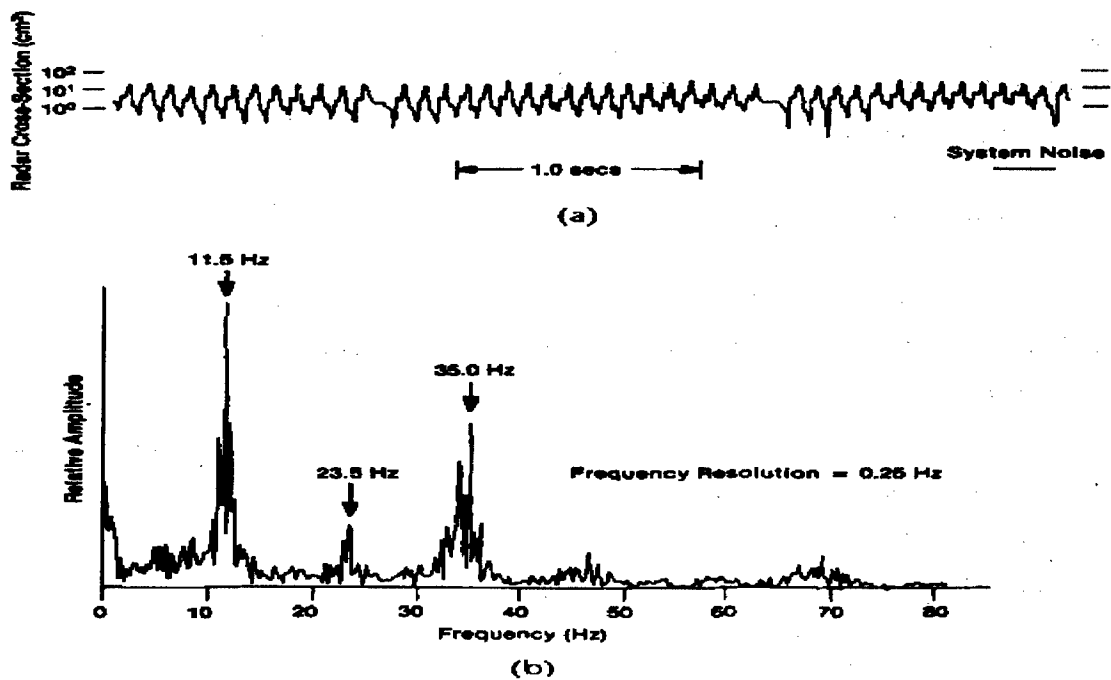


Figure 7.9 C-Band tracking data for a single migrating bird. (Vaughn 1974)

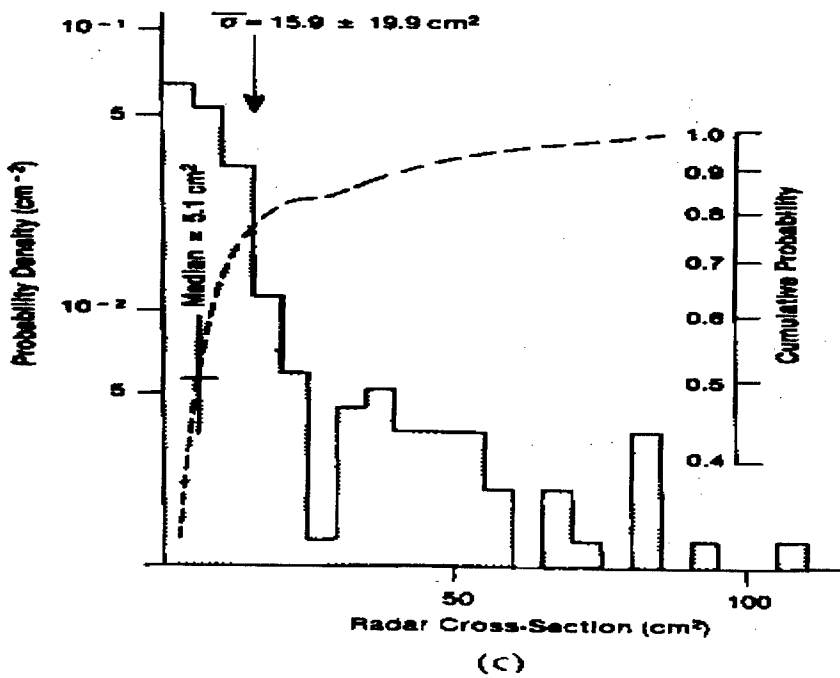


Figure 7.10 Probability density for bird measured in Figure 7.9 but for data taken several seconds earlier.

aspect angle to the radar. Another is that the body shape and wing orientation varies with wing beat creating an amplitude modulation. The instantaneous distribution can be represented by

$$p(\sigma) = \int_0^{\infty} p(\sigma/\underline{\sigma}) p(\underline{\sigma}) d\underline{\sigma}$$

where $p(\sigma/\underline{\sigma})$ is the conditional pdf of the wingbeat fluctuation given $\underline{\sigma}$ and $p(\underline{\sigma})$ is the aspect pdf with a mean value calculated using the optical sphere model.

Vaughn (1974), Flock (1974, 1976, 1977), Konrad et al (1968) and many others have measured the time histories of bird RCS. The amplitude modulation due to wingbeat are quasi-sinusoidal with 10 - 20 dB variations commonly observed. The wingbeat periods as presented in measurements presented by Vaughn (1974) range from 17 msec for a hummingbird to 178 msec. for a Willet. Rates for larger birds can be estimated using an empirical equation provided by Greenewalt (1960)

$$f = aL^{-1.15}$$

where f is the wingbeat frequency in Hz, L is the winglength in cm and $a = 572$.

Figure 7.9 show typical measurements of a single migrating bird obtained by Vaughn (1974) using a C-band tracking radar. Figure 7.9(a) presents the cross section in dB versus time while Figure 7.9(b) presents the relative power spectrum of the automatic gain control (AGC) voltage fluctuations corresponding to (a). The strong peak at 11.5 Hz is due to the wingbeating of the bird. The strong harmonics indicate the non-sinusoidal nature of the RCS. The pdf given in Figure 7.10 corresponds to a 1.024 second interval of AGC data taken several seconds before Figure 7.9(a) was taken. It portrays a skewed distribution with a mean-to-median ratio of 3.1 from which a log-normal or Weibull distribution might be inferred. However, additional measurement data on a Western sandpiper given in the same paper (also reviewed by Vaughn (1985)) notes that the mean value and shape of the distribution can change drastically in successive 1-second intervals due to aspect changes. Therefore, the data presented in Figure 7.10 represents $p(\sigma)$, not $p(\sigma/\underline{\sigma})$ or $p(\underline{\sigma})$. In the

absence of better data, the ADI model will assume that the conditional pdf of the wingbeat fluctuation is exponential.

In a recent summary article by Vaughn (1985), it is noted that RCS measurements as a function of aspect angle have been made for seven bird species. A typical example is given in Figure 7.11. Mack et al (1979) made extensive measurements of two 4 lb. ducks and one 10.8 lb goose at L-band. The birds were placed in polyfoam cages that could be positioned at the top of a polyfoam column to simulate free-space conditions. Figure 7.12 present the

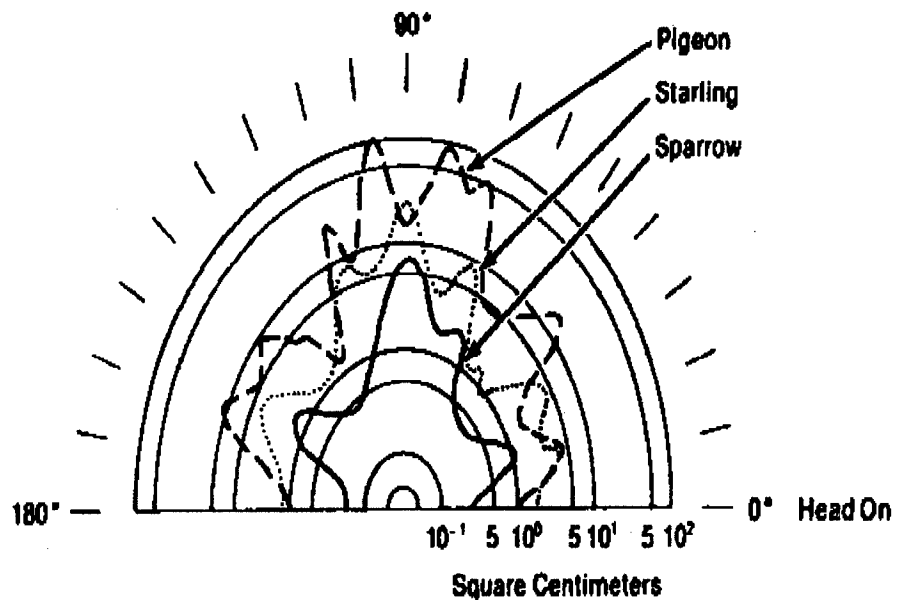


Figure 7.11 RCS polar diagram of three bird species (Edwards and Houghton as in Vaughn (1984))

results for one of the ducks. Movements by the birds caused a wild fluctuation of returns as represented by the wide range of values for many of the aspect angles. Figures 7.13 summarizes the range of these fluctuations by presenting the cumulative distribution of the maximum and minimum HH values for a duck. The fluctuations measured by Mack et al. (1979) imply an aspect distribution similar to log-normal distribution with a standard deviation of about 3 dB. Nathanson (1969) and Konrad et al (1968) also suggested a log-normal distribution with mean-to-median ratios of 2.5 for birds larger than four wavelengths and less for smaller birds. For the UHF to S-Band range, the wavelengths are generally comparable to or larger than most birds. Therefore, log-normal distribution with a standard deviation of 3 dB (mean-to-median ratio = 1.1) is suggested for the pdf versus aspect.

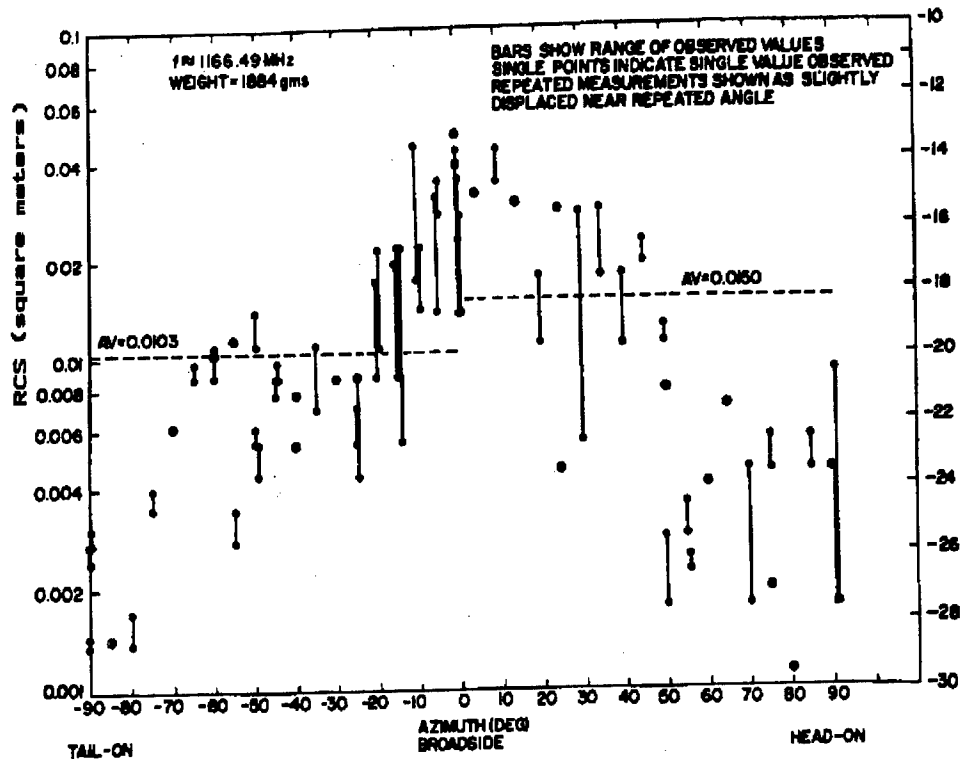


Figure 7.12 Measured Radar Cross Section of a duck versus aspect angle (Mack et al 1979)

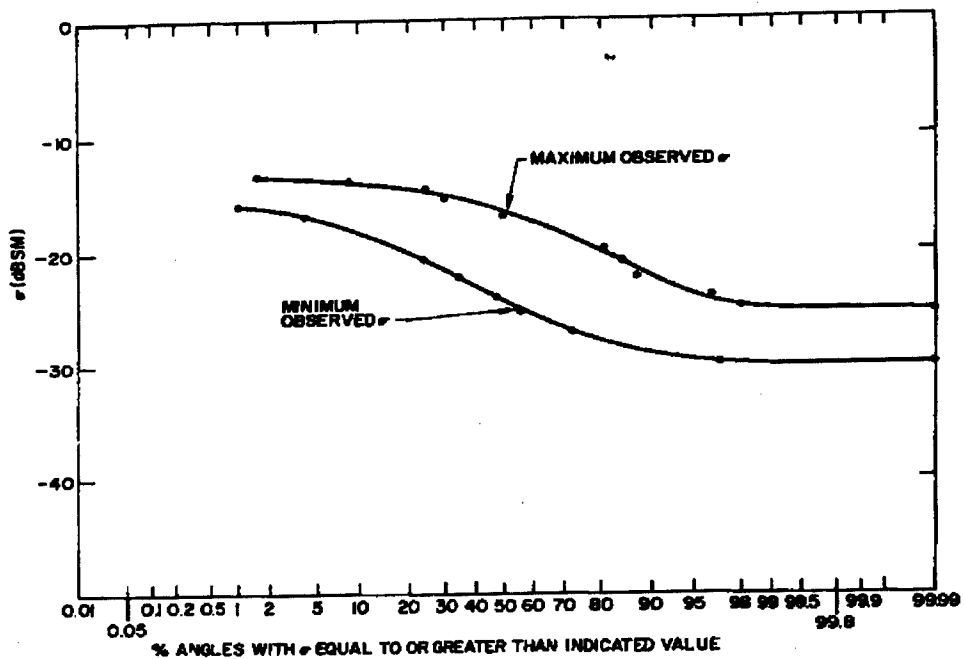


Figure 7.13 Cumulative Probability of a duck RCS versus aspect angle.

7.3 Velocity of Bird Angels

In summary, the variations about the mean for a single bird vary as a function of observation time. For intervals short relative to a wingbeat period ($t \ll$ a few milliseconds), the RCS is approximately constant. For intermediate time intervals containing several wingbeat period, but no aspect change, the RCS fluctuations will follow the wingbeat pdf, an exponential distribution. For longer time intervals, the distribution function is a compound distribution where the wingbeat pdf is the conditional distribution and the aspect pdf is the independent distribution.

Birds can fly at speeds ranging from near zero when soaring on thermals to over 100 mph when diving on prey. However, most birds fly between 5 and 50 mph. Heidbreder et al (1971) provides a reasonable model of bird velocities which is proposed for use for ADI.

$$f(V_b) = (1/2V_o)(V_b/V_o)^2 \exp[-(V_b/V_o)]$$

where V_b is the velocity of a bird and V_o is 9 knots. This distribution applies to the velocity of an angel which is assumed to have 10 birds. Once an angel has been assigned a velocity from this distribution, the velocity can be assumed to be constant for several minutes. Also, this velocity assumes a windless condition and the environmental winds must be vectorally added to obtain the true velocity of the angel.

Casual observations show that birds flying at low altitudes tend to change direction more often than those at higher altitudes. Table 4.2 presents these observations as a model versus height. The percentage of angels within each height interval assumes an exponential distribution of angel density with height given by $p(h) = -\exp(h/1500)/1500$.

Altitude Interval (kft)	% of angels	Heading changes (deg.)	Time Between Heading Changes
0-1	50	+180/-180	.1 sec to 60 seconds
1-2	25	+180/-180	1-5 minutes
2-4	20	+90 / -90	over 5 minutes
4-8	4.5	+30 / -30	over 5 minutes
8-16	0.5	+30 / -30	over 5 minutes

Table 4.2 Flight characteristics of bird angels versus height

7.4 Insect Angel Models

Referring to Figure 7.2, the RCS of individual insects is so small at the S-Band frequencies and below that a very high density is required for detection. However, many such instances occur. Goetis (1964) concluded that many sea breeze echoes were caused by birds and insects. Hardy and Ottersten (1969) concluded that the Benard-cell type of echo pattern from convective cells are really widely spaced insects tracing out the patterns of the air motion.

Vaughn (1985) provides a sampling of the densities observed in the literature. The highest is about 1 to 10 insects per cubic meter located near the surface. However, more typical values are in the vicinity of .01 to .001. A log-normal density is recommended for the distribution of angel density. The recommended median is .001 per cubic meter and the standard deviation is 6 dB. This density exists in a 100 meter layer located at 300 meters and is zero elsewhere. The corresponding median areal density is $3.4 \cdot 10^5$ per nm^2 .

Heidbreder et al (1971) gives a reasonable model for the RCS of an insect as given below:

Log-Normal density function for single insect

$$\text{Median} = -41 \text{ dBsm} - 40 \log \lambda$$

$$\text{Std. Deviation} = 6 \text{ dB}$$

where λ is the radar wavelength in cm.

At S-Band, this model would give a median RCS of -81 dBsm per insect. For a resolution cell area of $.1 \text{ nm}^2$, the RCS for the median population density given above is -35 dBsm. At the 1 % point, the RCS would be ~ -21 dBsm. L-band and UHF systems will observe substantially lower RCS values.

Airborne insect fly at the wind speed. Therefore, the velocity distribution is that given by the environmental winds provided in Section 3.0.

8.0 AURORA CLUTTER

The solar wind, a stream of charged particles from the sun, impinges on the earth's magnetic field. The interaction creates several regions of plasma, including a narrow sheet of plasma which is directly connected to the high-latitude ionosphere. This plasma is in constant convective motion as shown in Figure 8.1. The intersection of this electron stream with the earth creates an "auroral oval" which describes, at least statistically, the location of the electron stream in the E-layer as function of time (longitude) and latitude. Figure 8.2. presents the shape and location of the auroral oval is given for 1200 univeral time.

Auroral clutter is caused by backscatter from irregularities in the electron-density found in the ionospheric plasma. These irregularities may be visualized as thin plasma cylinders or rods, whose axes are aligned with the local geomagnetic field, and present in a continuum of scale sizes. Due to the high degree of anisotropy in the shape of the irregularities, their radio backscatter cross section is highly directional, that is, it is a strong function of the angle of incidence of the radio propagation vector on the geomagnetic field direction.

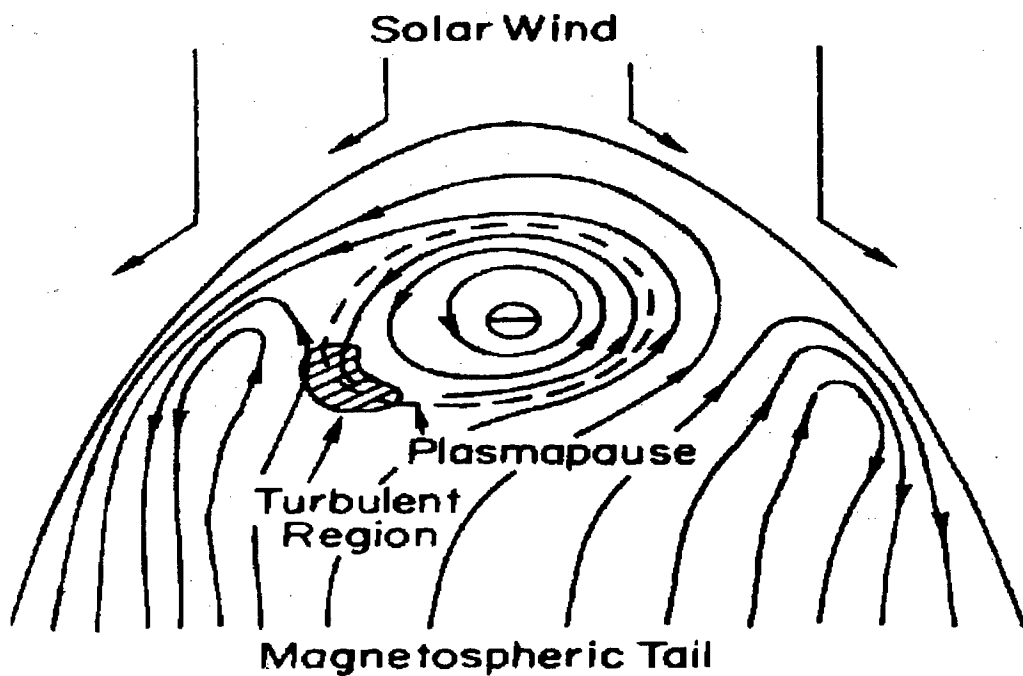


Figure 8.1 Equatorial Cross Section of Magnetosphere Showing Plasma Convection Pattern (Elkins 1980)

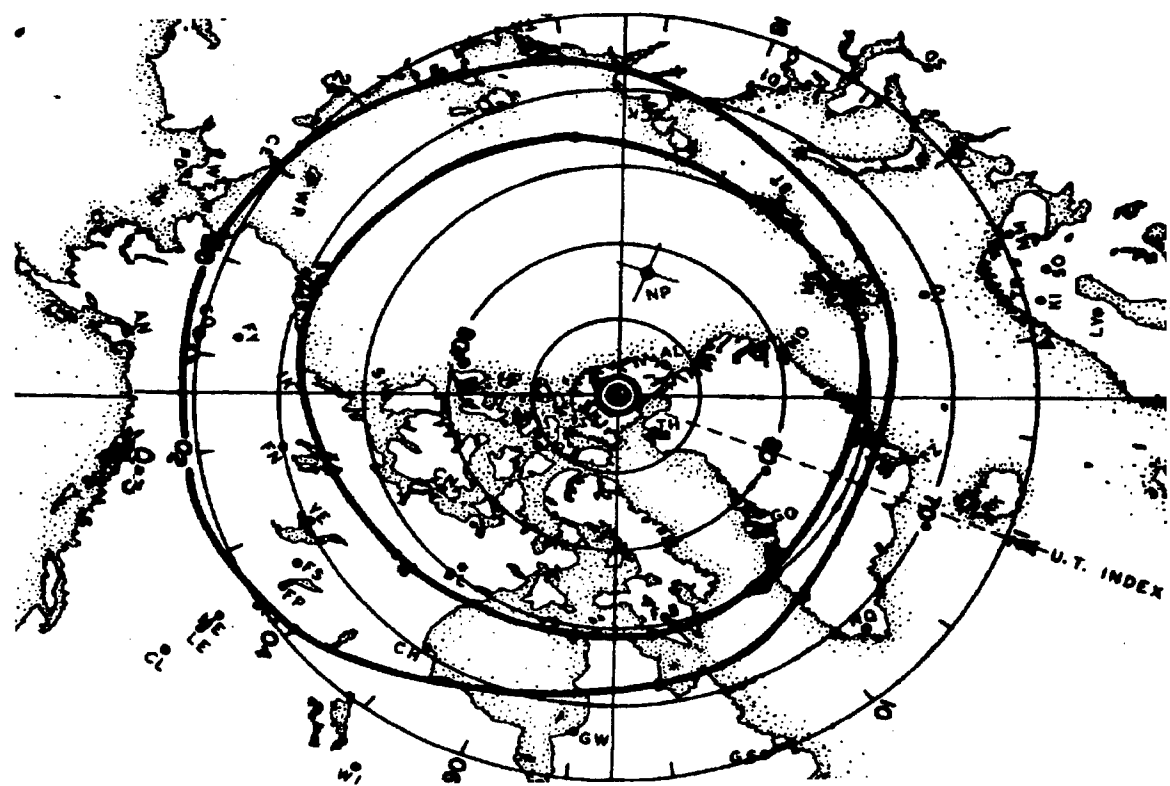


Figure 8.2 Map of northern polar regions showing location of the auroral oval at 12 UT for average geomagnetic activity. (Elkins 1980)

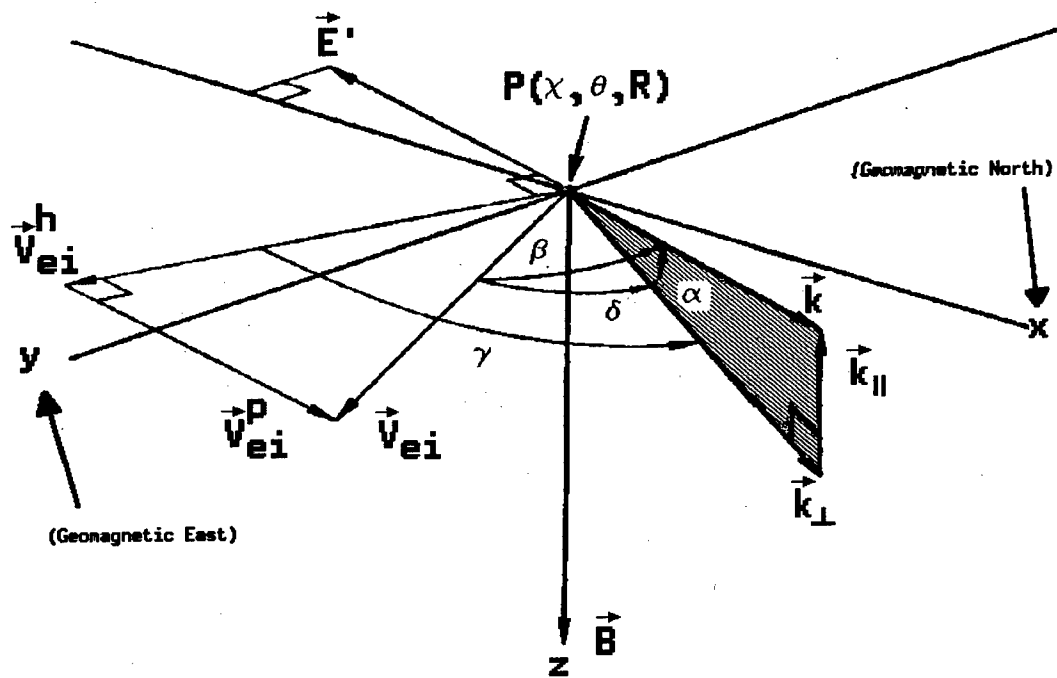


Figure 8.3 Radar scattering geometry (Derived from Tsunoda et al 1989)

Figure 3 presents the radar scattering geometry for aurora. $P(\chi, \theta, R)$ represents a point within the aurora at elevation angle χ , azimuth angle θ , and range R . The irregularity wave vector \underline{k} is the component parallel to the radar line of sight. \underline{E}' is the local electric field vector in the direction of the radar line of sight. \underline{V}_{ei} represents the streaming velocity vector of the electrons which can be represented by components parallel to (V_{ei}^P) and orthogonal to (V_{ei}^h) the radar line of sight.

In this model, the aurora clutter comes from a 30 km thick layer located between 92 km and 122 km. The boundary is abrupt at bottom and top of layer. Most of the literature on aurora reviewed in this study deal only with the mean volume reflectivity of aurora scatter. No studies on the spatial inhomogeneity or temporal nonstationarity were found although a few studies allude to such variability. (Elkins 1980, Mitchell and Brown 1976) In the absence of quantitative data on the spatial variability, this model will assume that auroral clutter within this layer is homogeneous.

The mean volume reflectivity from aurora can be given by

$$\eta_v(f_r, \alpha, \beta) = \eta_v(f_r)g(\alpha)\rho(\beta)$$

where $\eta_v(f_r)$ is the maximum reflectivity when $\alpha = \beta = 0$, $g(\alpha)$ presents the magnetic aspect angle dependence, $\rho(\beta)$ presents the flow angle dependence and the coordinate system for these angles is displayed in Figure 8.3. (Tsunoda et al 1989) The value of this maximum reflectivity is given as

$$\eta_v(f_r) = 32 \pi^4 r_e^2 N^2 |\Delta N/N|_{\max}^2 = S_o \exp(-(f_r - f_o)/f_s)$$

where N represents the plasma density, $|\Delta N/N|$ is the fractional fluctuation in the plasma density and r_e is the electron density. Tsunoda (1989) defines these parameters as follows:

$$\begin{aligned} |\Delta N/N|_{\max}^2 &= |\Delta N/N|_{f_o}^2 \exp(-(f_r - f_o)/f_s) \\ r_e &= 2.82 \times 10^{-15} \text{ meter} = \text{electron radius} \\ S_o &= 32 \pi^4 r_e^2 N^2 |\Delta N/N|_{f_o}^2 = 2 \times 10^{-8} \\ f_o &= 400 \text{ Mhz} \\ f_s &= 132 \text{ Mhz} \end{aligned}$$

Figure 8.4 shows that $\eta_v(f_r)$ compares well with measured values and provides a reasonable prediction of auroral clutter versus radar frequency.

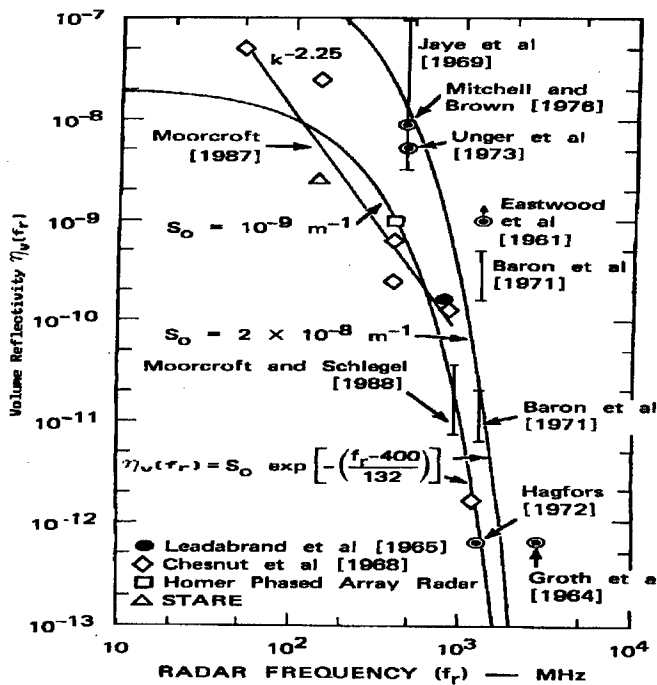


Figure 8.4 Comparison of $\eta_v(f_r)$ with VHF, UHF, L-band and S-band measurements (Derived from Tsunoda et al 1989)

The variation of mean reflectivity due to magnetic aspect angle is given as

$$g(\alpha) = \exp[-\{\pi \cdot 5 AB \ln(10)/20\} \operatorname{erf}(\alpha/B)]$$

$$A = 10.2$$

$$B = 8.4$$

The variation of mean reflectivity with respect to flow angle is given by

$$\rho(\beta) = 0.1 \exp(2.3 \cos^2 \beta)$$

β = flow angle as given in Figure 8.3.

Since the aurora is modeled as scatter from a large number of randomly positioned rods within the radar resolution volume, the pdf defining the fluctuation about the mean reflectivity is exponential. The temporal correlation properties of this fluctuation depends on the spread of auroral velocities illuminated by the antenna pattern. The radial or doppler velocity from a section located at angle β is

$$V_d = -\underline{V}_e \cdot \underline{k} / |\underline{k}|$$

where \underline{V}_e and \underline{k} are vectors defined in Figure 8.3 and $|\underline{V}_e| = 400$ m/s.

9.0 REFERENCES

Andrianov, V. A., Armand, N. A., and Kibardina, I. N., 1976, "Scattering of Radio Waves by an Underlying Surface Covered with Vegetation," Radio Engng. and Electron. Physics, Vol 21, No. 8

Andrianov, V. A., Bondarenko, I. S., Kibardina, I. N., Proshin, V. K. and Shtern, D. Y., 1976, "Characteristics of Measurement of Spectra of Radio Signals Scattered by an Underlying Surface," Radio Engng and Electron. Phys., Vol 21, No. 2

Armand, N. A., Dyakin, V. A., Kibardina, I. N., Pavel'ev, A. C., and Shuba, V. D., 1975, "The Change in the Spectrum of a Monochromatic Wave when Reflected from Moving Scatterers," Radio Engng and Electron. Physics, Vol 20, No. 7

Austin P. M., and Bemis, A. C., 1950, J. Meteor., V. 7, pp 145-151

Barlow, E. J., 1949, "Doppler Radar," Proc. IRE, vol. 37, pp.340-355

Barry, J. R., Carter, B. K. and Erdahl, R. J., 1973, Angel Clutter and the ASR Air Traffic Control Radar, Johns Hopkins Univ., APL-MSO-F-195 [AD775258]

Barton, D. K. (editor), 1975, Radar Clutter (Vol. 5 of Radars), Artech House, Dedham Ma

Bascom, W., 1964, Waves and Beaches, Anchor Books, Doubleday and Co., Inc. NY NY

Battan, L.J., 1959, Radar Meteorology, University of Chicago Press, Chicago

Battan, L.J., 1973, Radar Observation of the Atmosphere, University of Chicago Press, Chicago

Beals, G. A., 1970, Estimated Probabilities of Path-Cumulative Rain Intensity for Path of 10 and 22 Nautical Miles in High Rain Rate Areas, FAA-RD-70-55, FAA, Washington, DC

Beals, C. A., O'Reilly, P. J. and Davis, A. R., 1971, Precipitation Data for Radar Evaluation Studies, USAFETAC 6457

Billingsley, J. B., 1981, Analogous Terrain for Radar Ground Clutter Measurements, MITLL CMT-113

Blacksmith, P. and Mack, R. B., 1965, "On Measuring the Radar Cross Sections of Ducks and Chickens," Proc. IEEE 53:p1125 (1965)

Burroughs, H. H., 1967, Rain Intensity-Time Distributions, NOLC Report 720, Naval Ordnance Laboratory, Corona CA

Bussey, H. E., 1950, "Microwave Attenuation Estimated from Rainfall and Water Vapor Statistics," Proc. IRE, v. 38, pp781-785

Carlson, R. and Greenstein, L., 1969, A Distributed and Discrete Clutter Model for AWACS, TITRI Special Technical Report No. 2 (not published)

Caton, P. C. F., 1964, "A Study of Raindrop Size Distributions in the Free Atmosphere," Proc. Eleventh Wea. Radar Conf. pp. 136-141, Boston: Amer. Meteor. Soc.

Crane, A. K., 1980, "Prediction of Attenuation by Rain," IEEE Trans Comm., COM-28, pp 1717-1733

Daley, J., 1973, An Empirical Sea Clutter Model, NRL Memo 2668

Daley, J. C. and Burkett, J. A., 1970, Radar Backscatter Measurements at Low Angles on P and L Band, NRL Prob R02-37

Daley, J. C., Davis, W. T. and Mills, N.R., 1970, Radar Sea Return in High Sea States, NRL Report 7142

Daley, J. C., Davis, W. T., Duncan, J. R., and Laing, M. B., 1968, NRL Terrain Clutter Study, Phase II, NRL Report 6749

Daley, J. C., Davis, W. T., Duncan, J. R., and Laing, M. B., 1968, NRL Terrain Cluter Study, Phase II, NRL Report 6749

Daley, J. C., Ransome, J. T. and Burkett, J. A., 1971, Radar Sea Return - Joss I, NRL Report 7268

Daley, J. C., Ransome, J. T. and Davis, T., 1973, Radar Sea Return - Joss II, NRL Report 7534

Daley, J. C., Ransome, J. T., Burkett, J. A. and Duncan, J. R., 1968, Sea-Clutter Measurements on Four Frequencies, NRL Report 6806

Dawson, C. A., 1972, "Radar as a Diagnostic Tool for Lightning," J GeoPhys. Res. 77:4518-28

deRidder, C. M. , 1986, Airborne Radar Clutter Measurements: Description and Statistical Parameters for Processed Sample Patches, CMT-48, Vol. III

Doviak, R. J. and Zrnic, D. S., 1983, Doppler Radar and Weather Observations, Academic Press, NY

Drufuca, C. and Zawadzki, I. I., 1983, "Some Observation of the Fluctuating Radar signal," 21st Conf on Radar Meteor., Amer. Meteor. Soc.

Edwards, J. and Houghton, E. W., "Radar Echoing Area Polar Diagrams of Birds," Nature, vol. 184, p. 1059

Elkins, T. J., 1980, A Model for High Frequency Radar Auroral Clutter, RADC-TR-80-122

Feldman, N.E., 1979, Rain Attenuation Over Earth-Satellite Paths, Final Report, NELC Contract N00039-79-C-0136, ADA075390

Flock, W. L., 1974, "The Detection and Identification of Birds in Flight, Using Coherent and Noncoherent Radars", Proc. IEEE, Vol. 62, No. 6, June 1974, pp745-753

Flock, W. L., 1976, "Radar Echoes from Birds and their Effects on Radar Performance", Atmospheric Effects on Radar Target Identification and Imaging, p. 425-435

Flock, W. L., 1977, "Monitoring Overwater Bird Migration by Radar", XXIV Rassegna Internazionale Elettronica Nucleare Ed Aeroaziale, 23 Marzo - 3 Aprile, 1977, pp205-213

Cauthreaux, S. A., 1975, Radar Ornithology: Bird Echoes on Weather and Airport Surveillance Radars, AFOSR-TR-75-0317, AD-A006425

Gerlach. J. C. and Mazur, V., 1983, "UHF and S-Band Radar Observations of Electrically Active Storm Cells," 21st Conf. on Radar Meteor., American Meteorological Society

Coetis, S.C., 1964, "On Sea Breeze 'Angels'", Proc. Eleventh Wea. Radar Conf., pp 6-9. Boston: Amer. Meteor. Soc.

Coldstein, H., 1946, "Frequency Dependence of the Properties of Sea Echoes," Phys. Rev., vol 70, pp938-946; December 1 and 15, 1946

Crantham, D. D. and Kantor, A. J., 1967, Distribution of Radar Echoes over the United States, AFCRL-67-0232

Crantham, D.D. and 14 coauthors, 1983, Water Vapor, Precipitation, Clouds, and Fog: Chapter 16, Handbook of GeoPhysics and Space Environments. 1983 Revision, AFCL-TR-83-0181

Green, J. L. and Balsey, B. B., Development of Doppler Radar Techniques for the Detection of Bird Hazards, ADA030410

Greenstein, L., Brindley, A. and Carison R., 1969, A Comprehensive Ground Clutter Model for Airborne Radars, IIT Research Institute, September 1969

Greenwalt, C. H., 1962, Dimensional Relationships for Flying Animals, Smithsonian Miscellaneous Collections, Vol. 144, No. 2, Smithsonian Institute, Washington DC.

Guinard, N. W., Ransone, J. T. and Daley, J. C., 1971, "Variation of the NRCS of the Sea with Increasing Roughness," Journ. GeoDhys. Res., Vol 76, No. 6, Feb. 20, 1971

Guinard, N. W., Ransone, J. T., Jr., Laing, M. B. and Hearton, L. E., 1967, NRL Terrain Clutter Study Phase I, NRL Report 6487

Harper, W. G., 1958, "Detection of Bird Migration by Centimetre Radar - a Cause of Radar Angels," Proc Roy Soc London, vol 8, no. 149, pp.484-502

Heidbreder, G., Masuda, L., Pollon, G., Walker, J., 1971, A Study of Radar Angel Phenomena, ECOM-0278-F, AD883003

Jakeman, E., 1980, "On the Statistics of K-Distributed Noise", J. Phys. A: Math. Gen., 13(1980) pp.31-48

Jakeman, E. and Pusey, P. N., 1976, "A Model for Non-Rayleigh Sea Echo," IEEE AP-24, No.6, November 1976

James, W. J., 1961, The Effect of the Weather in Eastern England on the Performance of X-Band Radars, Royal Radar Establishment Tech. Note. TN # 655

Janza, F. J., Moore, R. K. and Warner, B. D., 1959, Radar Cross Sections of Terrain Near Vertical Incidence at 415 Mc, 3800 Mc. and Extension of Analysis to X-Band, Technical Report EE-21, Engineering Experimental Station, University of Mexico

Jao, J.K., 1983, First-Order Statistics of Radar Clutter Returns from Composite Terrain. CMT-39. Volume 1 and Volume 2, August 1983

Jones, M. A. and Sims, A. L., 1978, "Climatology of Instantaneous Rainfall Rates", J. Appl. Meteorology, V. 17 No. 8, pp1135-1140

Kapitanov, V. A., Mel'nichuk, V., and Chernikov, A. A., 1973, "Spectra of Radar Signals Reflected from Forests at Centimeter Waves," Radio Engng and Electron Phys., Vol 18, No. 9

Katzen, Martin, 1957, "On the Mechanisms of Radar Sea Clutter", Proc. IRE, Vol. 45, No. 1, pp 44-54, January 1957

Kazel, S., Patton, T. N., Dabkowski, J., Pipkin, R., and Brindley, A. E., 1971, Extensions to the ORT Clutter Model. JITRI Report for the Overland Radar Technology Program (unpublished)

Kerr, D. E. , 1951, Propagation of Short Radio Waves, McCraw-Hill Book Co., Inc.

Kerr, O. E. , 1979, Measured L-Band Radar Cross Sections of Ducks and Geese, RADC-TR-79-66, March 1979

Kinsman, Blair, 1965, Wind Waves, Dover Publications, Inc., 31 East 2nd St., Mineola, NY

Konrad, Hicks and Dobson, 1968, "Radar Characteristics of Known Single Birds in Flight", Science, vol. 159, no. 3812, pp. 274-280, Jan. 19, 1968

Lenhard, R. W., 1974, "Precipitation Intensity and Extent", J. Recherches Atmospheriques, Vol 8, pp375-384

Lenhard, R.W., Cole, A. E. and Sissenwine, N., 1971, Preliminary Models for Determining Instantaneous Precipitation Intensities from Available Climatology, AFCRL-71-0168

Lewinski, D. J., 1979, Characterization of Nonstationary Clutter, RADC-TR-79-267

Lewinski, D. J., 1983, "Nonstationary Probabilistic Target and Clutter Scattering Models," IEEE Trans. AP-31, No.3, May 1983

Lhermitte, R. M. and Atlas, D., 1963, "Doppler Fall Speed and Particle Growth in Stratiform Precipitation", Proc. Ninth Wea. Radar Conf., pp 218-223., Boston, Amer. Meteor. Soc.

Linell, T., 1963, "An Experimental Investigation of the Amplitude Distribution of Radar Terrain Return", 6th Conf. Swedish Nstl. Comm. Sci. Radio, Research Institute of National Defense, Stockholm

Long, Maurice W., 1975, Radar Reflectivity of Land and Sea, Lexington Books, D. C. Heath and Company, Lexington MA

Maffett, A., Klimach, H., Liskov, A., Rawson, R., Heimiller, R. and Tomlinson, P., 1978, L-Band Radar Clutter Statistics for Terrain and Ice, ERIM, Contract DAAK40-77-C-0112

Marshall, J. S. and Holtz, C. D., 1969, McGill University, Scientific Report MW-48 AD860954

Mitchell, M. J. and Brown, J. L., 1976, PAR Auroral Study. Volumes 1 - 5, Contract DASC-74-C-0026, ABMD Systems Command

Moore, R. K., 1969, Radar Return from the Ground, Bulletin of Engineering No. 59, University of Kansas, 1969

Mueller, E. A., 1983, "Differential Reflectivity of Birds and Insects" Proc. 21st Conf. Rad. Meteor., pp 465-466, 1983

Nathanson, F. E., 1969, Radar Design Principles, McGraw-Hill Book Co., New York

Newman, R. J. and Lowery, C. H., 1964, Select Quantitative Data on Night Migration in Autumn, Special Publ 3, Museum of Zoology, Louisiana State University, 1964

Nisbet, I. C. T., 1963, "Quantitative Study of the Migration with 23-Centimetre Radar", Proc Roy Soc London, Vol.105 (4), pp. 435-460, 1963

Northam, D. Y., 1985, Modeling of Electromagnetic Scattering from Ships, NRL [ADA169385]

O'Reilly, P.J., 1969, Instantaneous Surface Rainfall Rates and Associated Vertical Distributions of Total Water Content at Miami. Florida, unpublished report 6255, USAFETAC, Washington DC

O'Reilly, P. J., 1971, Clock-hour/Instantaneous Rainfall Rate Relationships Applicable to the Eastern United States, USAFETAC TN 71-12, Washington DC

Oliver, C. J., 1985, "Correlated K-Distributed Clutter Models", Opt. Acta, 1985, Vol. 32, pp. 1515-1547

Oliver C. J., 1988, "Representation of Radar Sea Clutter," Proc. IEE, Part F, No. 6, Vol 135

Owens, M. E. B., 1974, Empirical Bayes Estimation of the Probability Density of the Radar Cross Section of the Sea Surface, NRL Report 7741

Pollon, C. E., 1972, "Distributions of Radar Angels," Aero. and Elect. Sys., Vol. AES-8, No. 6, November 1972

Schmidt, K. R., 1970, Statistical Time-varying and Distribution Properties of High-Resolution Radar Sea Echo, NRL Report 7150

Sekine, M., 1979, Unpublished letter to Dr. J. Clarke, IEE editor, provided courtesy of Mr. F. Fay, MITRE

Sekine, M., Musha, T., Tomita, Y., Hagisawa, T., Irabu, T. and Kiuchi, E., 1984, "Weibull Distributed Weather Clutter in the Frequency Domain", IEE Proc., Vol. 131, Pt. F, No. 5, pp 549-553

Sekine, M., Ohtani, S., Musha, T., Irabu, T., Kiuchi, E., Hagisawa, T. and Tomita, Y., 1981, "Suppression of Ground and Weather Clutter", IEE Proc. F, Commun., Radar & Signal Process., Vol 128, (3), pp.175-178

Simkins, W. L., 1981, ATR Clutter Model (unpublished), distributed as Addendum C, Specifications for Advanced Tactical Radar, PR A-2-1000,

Simkins W. L., 1984, ARSR-4 Clutter Model (unpublished), distributed as Appendix A, Specifications for the ARSR-4, FAA-E-2763

Simkins, W. L., 1985, SOWRBALL Radar Procurement, US Customs Service, system model used parts of the ARSR-4 model provided by W. L. Simkins in 1985.

Simkins, W. L., Vannicola, V. C. and Ryan, J. P., 1977, Seek Igloo Radar Clutter Study, RADC-TR-77-338

Skolnik, M., 1962, Introduction to Radar Systems, McGraw-Hill Book Company, NY

Skolnik, M., 1970, Radar Handbook, McGraw-Hill Book Co., Inc. NY

Skolnik, M. I., 1974, "An Empirical Formula for the Radar Cross Section of Ships at Grazing Incidence," IEEE Trans. of Aero. and Elec. Systems, p. 292

Tatarski, V.I., 1961, Wave Propagation in a Turbulent Medium, New York: McGraw-Hill.

Thurman, L. A., 1981, Analysis of Selected Naval Research Laboratory Four-Frequency Radar Data: New Jersey Measurements, MITLL CMT-12, ESD-TR-81-3

Torlaschi, E. and Humphries, R. C., 1983, "Statistics of Reflectivity Gradients, "21st conf. On Radar Meteor., Amer. Meteor. Soc.

Trunk, C. V., 1972, "Radar Properties of Non-Rayleigh Sea Clutter," IEEE Trans. AES-9, No. 2

Tsunoda, R. T., Williams, M. F., Leger, C. A., Price, C. H., Trent, R. A., Zembre, Y., 1989, A Comprehensive E-Region Auroral Clutter (CERAC) Model; Preliminary Results, Interim Technical Report

Valenzuela, C. R. and Laing, M. B., 1971, On the Statistics of Sea Clutter, NRL Report 7349

Valenzuela, C. R., Laing, M. B. and Daley, J. C., 1971, "Ocean Spectra for the High-frequency Waves as Determined from Airborne Radar Measurements" Sears Foundation, J. Marine Res., Vol 29, No. 2

Vaughn, C. R., 1974, "Intraspecific Wingbeat Rate Variability and Species Identification using Tracking Radar", A Conference on the Biological Aspects of the Bird/Aircraft Collision Problem, Feb. 5-7, 1974

Vaughn, C. R., 1985, "Birds and Insects as Radar Targets: A Review," Proc. IEEE, Vol. 73, No. 2, February 1985, pp. 205-227

Ward, K. D., 1982, "A Radar Sea Clutter Model and its Application to Performance Assessment", IEE Conf. Publ. 216 (Radar '82), 1982, pp. 203-207

Ward, K. D., 1987, "Spatial Correlation in K-Distributed Sea Clutter", Proc. IEE Part F, Vol. 134, No. 6

Ward, K. D. and Watts, S., 1985, "Radar sea clutter", Microwave Journal, June 1985, Vol 28, pp. 109-121

Webster, D. J., 1966, "An Analysis of Winter Bird-Population Studies", The Wilson Bulletin, Vol. 76 No. 4, December 1966, pp. 456-461

Winner, D. C., 1968, Climatological Estimates of Clock-hour Rainfall Rates, AWSTR 202, Air Weather Service

Wright, J. W., 1968, "A New Model for Sea Clutter," IEEE Trans. AP-16, No.2, March 1968

(No Author), 1980, Environmental Trends, Council on Environmental Quality, Executive Office of the President, Washington DC.

(No Author), 1989, National Data Book and Guide to Sources, Statistical Abstract of the US, US Department of Commerce, 1989